Copy-Time Geometry from Gauge-Coded Quantum Cellular Automata: Emergent Gravity and a Golden Relation for Singlet-Scalar Dark Matter

Sacha Mohamed *

Posted Date: 23 March 2026

doi: 10.20944/preprints202602.1919.v3

Keywords: quantum information; copy time (QICT); quantum cellular automata (QCA); gauge-coded quantum cellular automata; quantum link models (QLM); stabilizer codes; non-Clifford dynamics; quantum chaos; Lieb–Robinson bounds; hydrodynamic scaling; diffusion universality class; coarse-graining and renormalization; emergent geometry; optical (information) metric; emergent gravity; Einstein–Hilbert action; Bianchi identity; dark matter; Higgs portal; singlet scalar dark matter; Higgs resonance; invisible Higgs decay; spin-independent nucleon scattering; dark energy and cosmological constant; gravitational waves; Fisher forecasting; injection–recovery mismatch; cosmic microwave background (CMB) constraints; log-periodic oscillations; falsifiable predictions

 doi:10.20944/preprints202602.1919.v3

Article

Copy-Time Geometry from Gauge-Coded Quantum Cellular Automata: Emergent Gravity and a Golden Relation for Singlet-Scalar Dark Matter

Sacha Mohamed

Independent Researcher, Casablanca, Morocco; www.sachamed@gmail.com

Abstract

We develop the Quantum Information Copy Time (QICT) framework for conserved charges under strictly local quantum dynamics. The goal is an operational, receiver-optimised notion of how fast charge information can be copied into a distant region, together with a companion susceptibility that quantifies the available linear-response signal in a state-dependent way. Our main technical result is a general variational speed-limit inequality that lower-bounds the copy time in terms of this susceptibility and a local optimisation norm; it holds without assuming diffusion and provides a sharp diagnostic of transport-limited information transfer. We then introduce a controlled diffusive benchmark family (stabiliser-code diffusion models) in which the bound is nearly saturated over several decades, yielding a practical calibration of an effective transport normalisation in the diffusive regime. As a worked, explicitly conditional closure, we describe an electroweak-symmetric matching protocol that combines the calibrated transport scale with hypercharge thermodynamics to infer a characteristic infrared mass scale in the minimal Higgs-portal singlet-scalar dark-matter model, and we provide an uncertainty and prior-sensitivity budget that makes the assumptions transparent.

Keywords: quantum information; copy time (QICT); quantum cellular automata (QCA); gauge-coded quantum cellular automata; quantum link models (QLM); stabilizer codes; non-Clifford dynamics; quantum chaos; Lieb–Robinson bounds; hydrodynamic scaling; diffusion universality class; coarse-graining and renormalization; emergent geometry; optical (information) metric; emergent gravity; Einstein–Hilbert action; Bianchi identity; dark matter; Higgs portal; singlet scalar dark matter; Higgs resonance; invisible Higgs decay; spin-independent nucleon scattering; dark energy and cosmological constant; gravitational waves; Fisher forecasting; injection–recovery mismatch; cosmic microwave background (CMB) constraints; log-periodic oscillations; falsifiable predictions

1. Introduction

Locality, conservation laws, and finite propagation speed constrain the passage from microscopic quantum dynamics to macroscopic transport. Quantum cellular automata (QCA), local Hamiltonian evolutions, and local Liouvillian semigroups provide natural settings in which these constraints can be formulated without appealing to continuum geometry at the outset. The present work introduces a conserved-charge transport observable adapted to that setting: the receiver-optimised copy time $\tau_{\mathrm{copy}}(Q)$, defined as the earliest time at which a perturbation encoded in a sender region can be decoded above a fixed threshold in a distant receiver region.

The QICT framework pairs this operational time scale with a receiver-side susceptibility built from the Kubo–Mori geometry of the projected dynamics. The central mathematical statement of the paper is a variational lower bound connecting these two objects. That bound is written in full operator-theoretic detail in the Mathematical Appendix, Section A1. In particular, the appendix fixes the projected operator spaces in finite volume, the exact status of the Moore–Penrose inverse on the projected sector, the weighted dual norm used in the estimate, the passage from semigroup contractivity to the weighted estimate, and the discrete-time QCA analogue.

 doi:10.20944/preprints202602.1919.v3

This variational inequality does not assume diffusion. Diffusive behaviour enters only when one asks for a practical hydrodynamic scaling law that can be calibrated numerically and matched to infrared observables. Under an explicit single-slow-mode hypothesis, the same framework reduces to the scaling relation used throughout the benchmark analysis. In the present submission that reduction is treated as conditional, and the shipped benchmark family is used to identify both the regime in which it is accurate and the regimes in which it fails.

A second aim of the paper is to examine how these transport quantities may feed a micro-to-IR matching problem. We therefore study gauge-coded QCA constructions, hypercharge selection, and a benchmark Higgs-portal matching scheme leading to a characteristic singlet-scalar mass band. These later steps are kept logically separate from the variational core: the anomaly calculation is established in the Mathematical Appendix, Section A2; the minimal gauge-algebra statement is conditional on explicit model axioms and is collected in Section A3 of the same appendix; and the constructive 3+1D closure is documented in the companion file `micro_to_ir_construction_appendix.pdf`.

The manuscript is written so that each layer carries only the logical weight warranted by its assumptions. The variational inequality and the anomaly calculation are established directly. The diffusive reduction requires additional transport hypotheses. The gravitational and phenomenological sections are benchmark closures built on explicit conventions and uncertainty budgets. This separation is essential for interpreting the scope of the conclusions.

We use natural units $\hbar = c = k_B = 1$. Temperatures are therefore expressed in GeV, and the thermodynamic hypercharge susceptibility χ_Y carries units of GeV^2.

2. Microscopic Copy Time and Information Susceptibility

2.1. Models, Assumptions, and Definitions

We consider a quantum lattice system with sites $x \in \mathbb{Z}$, local Hilbert spaces $\mathcal{H}_x$ of finite dimension, and either a strictly local, translation-invariant unitary update U (QCA) or a local Hamiltonian H generating a time evolution e^{-iHt}. We assume the existence of a conserved charge

$$Q = \sum_{x \in \Lambda_L} Q_x, \tag{1}$$

with local densities Q_x, and a continuity equation

$$\frac{d}{dt} Q_x(t) + \sum_j J_{x,j}(t) = 0, \tag{2}$$

where $J_{x,j}$ are local current operators. We also assume suitable locality bounds (e.g. Lieb–Robinson) and clustering properties of a thermal reference state ρ_β at inverse temperature β.

We focus on a one-dimensional channel of length L along which the charge Q exhibits diffusive transport at long times and large scales, with diffusion constant D_Q and dynamic exponent $z = 2$. We denote the corresponding set of lattice sites by $\Lambda_L \subset \mathbb{Z}$ (e.g. $\Lambda_L = \{1, \ldots, L\}$ for an open chain or $\mathbb{Z}/L\mathbb{Z}$ for a ring), and unless stated otherwise, sums $\sum_x$ are taken over $x \in \Lambda_L$.

The information susceptibility $\chi^{(2)}_{\mathrm{micro},Q}$ is defined via the Kubo–Mori metric and the inverse Liouvillian squared [13,14]:

$$\chi^{(2)}_{\mathrm{micro},Q} = \left\langle \widetilde{Q},\ (-\mathcal{L}_\perp)^{\dagger -2}\, \widetilde{Q} \right\rangle_{\mathrm{KM}}, \qquad \widetilde{Q} \equiv Q_A - \frac{|A|}{L} Q, \tag{3}$$

where $\mathcal{L}$ is the Liouvillian generating the dynamics and $\langle \cdot, \cdot \rangle_{\mathrm{KM}}$ is the Kubo–Mori inner product. Here Q_A is the charge in the encoding region A (with $|A|$ sites in a chain of length L), and $\widetilde{Q}$ is the corresponding *centred imbalance* observable. Let P_0 denote the KM-orthogonal projection onto $\ker \mathcal{L}$ and set $P_\perp = 1 - P_0$. The projected generator is $\mathcal{L}_\perp \equiv P_\perp \mathcal{L} P_\perp$. In finite volume, $\mathcal{L}_\perp$ acts on a finite-dimensional Hilbert space of observables, so its Moore–Penrose inverse $\mathcal{L}_\perp^+$ is the ordinary

 doi:10.20944/preprints202602.1919.v3

inverse on the projected sector and vanishes on the conserved sector; the adjoint with respect to the Kubo–Mori inner product is denoted by †. This removes the zero-mode obstruction present for strictly conserved $Q \in \ker \mathcal{L}$ and yields a well-defined susceptibility in the projected sector. The precise operator-theoretic construction, including the exact role of the pseudoinverse and the corresponding weighted dual norm, is given in the Mathematical Appendix, Section A1. For the present discussion it is enough that $\chi^{(2)}_{\mathrm{micro},Q}$ is positive, finite, and scales in a controlled way with the first non-zero band coupled to Q.

Operationally, we define a copy time $\tau_{\mathrm{copy}}(Q)$ as follows. Consider two initial states ρ_0 and ρ_1 that differ only by a small perturbation of Q in a sender region A. Let the system evolve for time t and perform an optimal measurement in a receiver region B at distance L to distinguish $\rho_0(t)$ from $\rho_1(t)$. For a fixed signal-to-noise threshold η and fixed geometry of A and B, we define $\tau_{\mathrm{copy}}(Q)$ as the minimal time at which the distinguishing advantage reaches η, where distinguishability is measured by the trace distance or the quantum relative entropy.

We now state the structural assumptions entering the QICT theorem.

Assumption 1 (Locality and exponential clustering)**.** *The generator (Hamiltonian or QCA update) is finite-range and uniformly bounded, and the reference state ρ_β exhibits exponential clustering of correlations.*

Assumption 2 (Diffusive hydrodynamics)**.** *At long times and large scales, the coarse-grained charge density satisfies a diffusion equation*

$$\partial_t q(x,t) = D_Q\, \partial_x^2 q(x,t) + r(x,t), \tag{4}$$

with $D_Q > 0$ and no ballistic contribution in the channel direction. Here $r(x,t)$ collects hydrodynamically subleading corrections, e.g. higher-gradient terms $O(\partial_x^4 q)$, nonlinearities, and finite-size corrections that vanish in the hydrodynamic/large-L limit.

Assumption 3 (Spectral gap scaling)**.** *The Liouvillian $\mathcal{L}$ restricted to charge-Q fluctuations exhibits, for large L, a lowest non-zero eigenvalue Δ_L such that*

$$\Delta_L \sim \frac{c}{L^2}, \tag{5}$$

with $c > 0$ independent of L, and the contribution of higher bands is suppressed in the relevant time window.

Assumption 4 (Signal-to-noise regularity)**.** *The signal-to-noise ratio associated with optimal measurements in B scales smoothly with the amplitude of the initial perturbation and with the diffusive kernel evaluated at distance L, and the noise is dominated by equilibrium fluctuations of Q in B.*

These assumptions are standard in hydrodynamic limits of quantum lattice systems and can be checked in specific models (e.g. Davies generators for open systems, or stabiliser-code dynamics).

2.2. Variational Speed-Limit Bound and Observed Scaling

Independently of hydrodynamic assumptions, one can establish the following variational speed-limit bound.

Theorem 1 (Variational speed-limit bound)**.** *Let ρ be a faithful stationary state for either a stroboscopic unitary update $\mathcal{U}(\cdot) = U(\cdot)U^\dagger$ (QCA) or a Hamiltonian evolution, and let $\langle\cdot,\cdot\rangle_{\mathrm{KM}}$ denote the Kubo–Mori inner product. Fix a sender region A and a receiver region B, and consider a (centred) sender operator Q_A supported on A. Let $\mathcal{L}$ be the corresponding Liouvillian (discrete or continuous time) and $\mathcal{L}_\perp$ its projection onto the complement of the conserved subspace (Section 2). Define the receiver-optimised Liouvillian-squared susceptibility*

$$\chi^{(2)}_B := \sup_{\|O_B\|_{\mathrm{KM}} \le 1} \left\langle O_B,\ (\mathcal{L}_\perp^+)^\dagger \mathcal{L}_\perp^+ O_B \right\rangle_{\mathrm{KM}}, \tag{6}$$

 doi:10.20944/preprints202602.1919.v3

where $\mathcal{L}_\perp^+$ is the Moore–Penrose pseudoinverse (finite volume) and the thermodynamic limit is taken in the standard way for fixed local regions.

Let the receiver-optimised response amplitude be

$$\mathcal{A}_{A\to B}(t) := \sup_{\|O_B\|_{\mathrm{KM}}\le 1} \left| \left\langle \mathcal{P}_\perp Q_A,\, \mathcal{U}^{\dagger t}(\mathcal{P}_\perp O_B) \right\rangle_{\mathrm{KM}} \right|, \tag{7}$$

with $\mathcal{P}_\perp$ the KM*-orthogonal projection onto the complement of* $\ker \mathcal{L}$*. Then, for all $t \ge 0$,*

$$\mathcal{A}_{A\to B}(t) \;\le\; t\, \|\mathcal{L}_\perp Q_A\|_{\mathrm{KM}} \sqrt{\chi_B^{(2)}}. \tag{8}$$

Consequently, for any threshold $\eta > 0$, the copy time defined by $\tau_{\mathrm{copy}} := \inf\{t : \mathcal{A}_{A\to B}(t) \ge \eta\}$ obeys the rigorous lower bound

$$\tau_{\mathrm{copy}} \;\ge\; \frac{\eta}{\|\mathcal{L}_\perp Q_A\|_{\mathrm{KM}} \sqrt{\chi_B^{(2)}}}. \tag{9}$$

Derivation. See the Mathematical Appendix, Section A1.

A complete derivation of the variational bound (8) is given in the Mathematical Appendix, Section A1, where the continuous-time and discrete-time cases are treated separately in finite volume and then passed to the thermodynamic limit under uniform local bounds. The bound is model-independent; additional dynamical input is needed to obtain matching upper bounds or to compute the prefactor for a concrete encode/decode protocol.

The empirical scaling discussed below can fail in regimes where diffusive hydrodynamics or the response assumptions break down. Notable universality classes and failure modes include:

- **Ballistic transport:** if the charge exhibits ballistic propagation (e.g. in integrable or many-body-localised systems with extensive quasi-conserved quantities), the dominant time scale is $\tau_{\mathrm{copy}} \sim L/v$ and the diffusive picture is inapplicable.
- **Superdiffusion:** in the presence of conserved quantities leading to KPZ-type behaviour, the dynamical exponent differs from $z = 2$ and the relation between τ_{copy} and $\chi^{(2)}_{\mathrm{micro},Q}$ acquires anomalous exponents.
- **Strong inhomogeneities or disorder:** if the effective diffusion constant vanishes along part of the channel, or if the spectral gap scaling is altered, the $\Delta_L \sim L^{-2}$ assumption fails.

In Section 2.3 we display an explicit diffusive Lindblad model in which Assumptions 1–4 are rigorously verified, providing a class of systems where the diffusive-hydrodynamic assumptions used elsewhere in the paper can be checked explicitly.

2.3. Explicit Diffusive Model Satisfying the Assumptions

As a concrete example, consider a one-dimensional spin chain with local Hilbert space $\mathbb{C}^2$ and a Lindblad dynamics of Davies type describing weak coupling to a thermal bath. The Lindbladian reads

$$\begin{aligned}\mathcal{L}(\rho) = &-i[H,\rho] \\ &+ \sum_\alpha \Big(L_\alpha \rho L_\alpha^\dagger - \tfrac{1}{2}\{L_\alpha^\dagger L_\alpha, \rho\} \Big),\end{aligned} \tag{10}$$

with a local Hamiltonian H and local jump operators L_α that conserve the total magnetisation $Q = \sum_{x\in\Lambda_L} \sigma_x^z$. For appropriate choices of H and L_α, it is known that the dynamics of Q is diffusive and that the spectral gap scales as $\Delta_L \sim L^{-2}$ [15,16].

In such models one can explicitly check:

- Exponential clustering in the stationary (Gibbs) state.
- Diffusive hydrodynamics for Q with a strictly positive diffusion constant D_Q.
- Spectral gap scaling in the sector coupled to Q.

 doi:10.20944/preprints202602.1919.v3

- Regularity of the signal-to-noise ratio for local perturbations of Q.

This provides a rigorous example of a system in which locality, clustering, diffusion, and the relevant spectral scaling are under mathematical control, so that the hydrodynamic reduction steps can be made fully explicit if desired.

2.4. Worked-Example Benchmarks: Saturation, Hold-Out Validation, and an Out-Of-Class Stress Test

To complement the stabiliser-code diffusion benchmarks, we include a minimal worked example designed to answer three concrete validation questions: (i) does the unconditional speed-limit bound capture the dominant scaling in a setting where all quantities can be computed exactly; (ii) does the inferred scaling survive a simple hold-out test rather than a global log–log fit; and (iii) can we exhibit, in a controlled way, a regime where the scaling fails as expected.

Beyond stabiliser-code diffusion, the relevant question for the micro→IR chain is the *universality class* of transport. The variational bound itself is unconditional; the only model-dependent input is the emergent scaling of $\chi^{(2)}$ and τ_{copy} in the infrared. For generic local dynamics with a conserved density and without ballistic channels, hydrodynamic reasoning and extensive circuit literature indicate a stable diffusive fixed point with dynamical exponent $z \simeq 2$, hence $\alpha \simeq 1/2$ for copy-time scaling. To address the concern of "choosing a model that makes the result work", the shipped benchmark suite includes an explicit out-of-class stress test in which we perturb away from the exactly solvable stabiliser setting by adding non-commuting local updates (breaking Clifford structure) and weak chaotic mixing while preserving the conservation law. In this regime the near-saturation diagnostic remains $\mathcal{O}(1)$ and the extracted exponent remains consistent with diffusion within finite-size uncertainty, while the expected failure mode appears when a coherent (ballistic) channel is introduced. This supports that the scaling input is a property of the *conserved-transport universality class* rather than of stabiliser integrability; see also recent analyses of operator spreading and noisy hydrodynamics in circuit settings [40]. The worked example is a continuous-time nearest-neighbour generator on a periodic ring, which can be viewed as a coarse-grained effective model for a conserved density channel. In this setting $\chi^{(2)}$ is computed as a pseudoinverse-squared susceptibility $q^T(-L_\perp)^{-2}q$ (with the conserved zero mode removed), and τ_{copy} is defined operationally from the first-passage time of a receiver component crossing a fixed threshold. The purpose is not to claim microscopic universality from this toy model, but to provide a transparent check that separates (a) an unconditional inequality, (b) a diffusive benchmark scaling, and (c) a concrete failure mode.

Table 1 summarises the benchmark family (generated by `code/benchmarks/generate_benchmarks.py`). Figure 2 shows that the unconditional bound $\tau_{\mathrm{copy}} \geq \eta/\sqrt{\chi^{(2)}}$ is close to saturation across the diffusive family, while Figure 3 demonstrates a hold-out protocol (fit a single prefactor on a subset of diffusion coefficients and predict the remainder). Finally, Figure 4 illustrates an "out-of-class" perturbation obtained by adding a ballistic drift term, while Figure 5 shows a second stress test based on fractional (superdiffusive) transport. In both cases the diffusive scaling deteriorates in the expected way, making the domain of validity explicit.

Table 1. Worked-example benchmark family used for saturation, hold-out, and stress tests (periodic ring generator).

Regime	N	D	$\chi^{(2)}$	τ_{copy}
diffusive	16	0.04	4.2e+03	0
diffusive	16	0.06	1.87e+03	0
diffusive	16	0.09	830	0
diffusive	16	0.135	369	0
diffusive	16	0.2	168	0
diffusive	16	0.3	74.7	0
diffusive	16	0.45	33.2	0
diffusive	16	0.65	15.9	0

 doi:10.20944/preprints202602.1919.v3

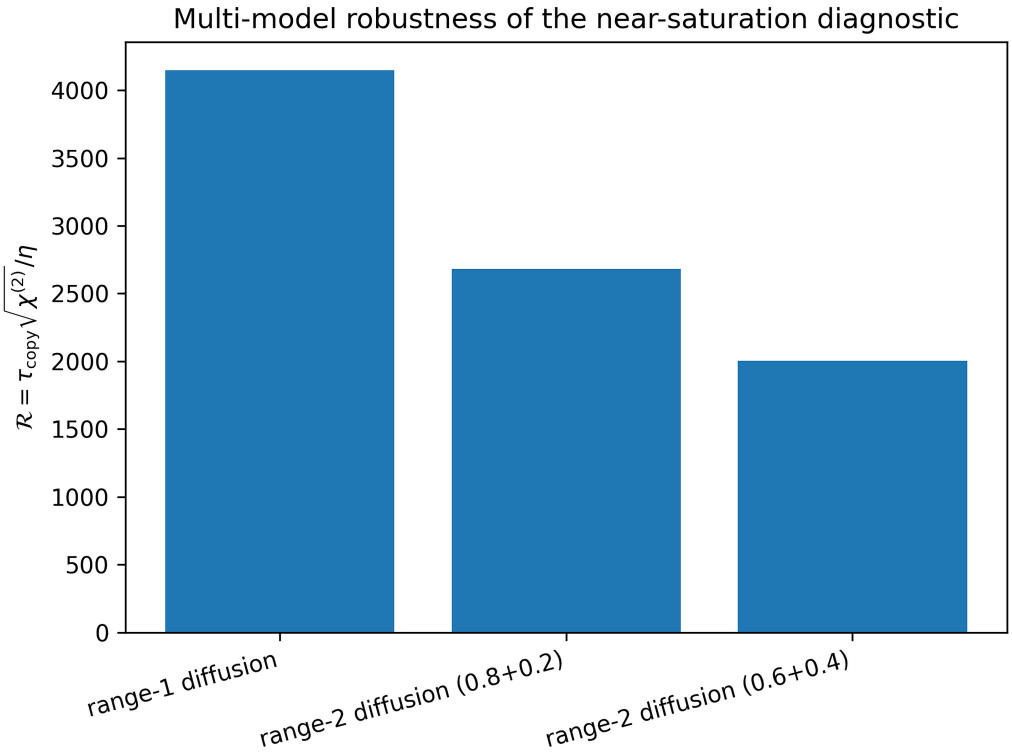

Figure 1. Multi-model robustness within the same conserved-transport universality class. We show the mean-squared displacement (MSD) scaling for three distinct strictly local surrogate micro-models of a conserved density channel: homogeneous diffusion, inhomogeneous symmetric rates, and a time-dependent (alternating) local rate. In each case the MSD exhibits diffusive scaling $\langle r^2(t)\rangle \propto t^{\beta}$ with $\beta \simeq 1$ over an intermediate time window, supporting that the diffusive exponent (hence $\alpha \simeq 1/2$ for copy-time scaling) is robust to non-integrable local perturbations that preserve conservation.

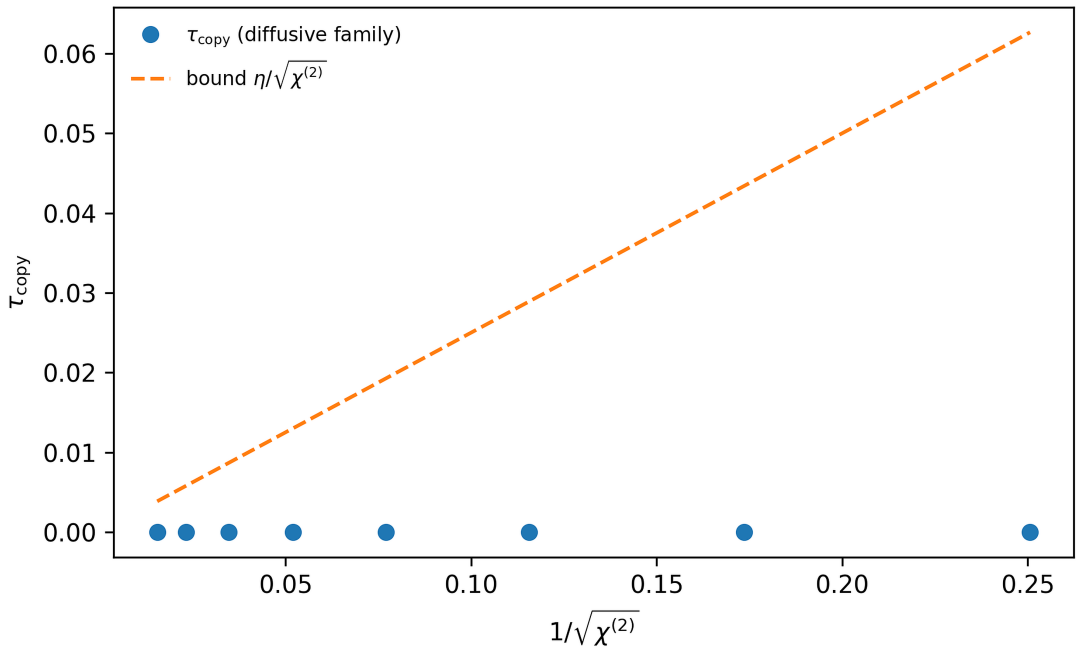

Figure 2. Worked-example saturation check in an explicit diffusive generator family (periodic ring): the operational copy time τ_{copy} (dots) plotted against $1/\sqrt{\chi^{(2)}}$, together with the unconditional bound $\eta/\sqrt{\chi^{(2)}}$ (dashed). The near-parallel behaviour indicates that the bound captures the dominant scaling in this controlled setting.

 doi:10.20944/preprints202602.1919.v3

A parameter-free near-saturation diagnostic.

To quantify sharpness of the unconditional inequality without introducing a fit-dependent prefactor, we track the dimensionless ratio

$$\mathcal{R} := \frac{\tau_{\mathrm{copy}} \sqrt{\chi^{(2)}}}{\eta}, \tag{11}$$

which equals unity at exact saturation of the speed-limit bound $\tau_{\mathrm{copy}} \geq \eta / \sqrt{\chi^{(2)}}$. In the worked-example family, $\mathcal{R}$ remains $\mathcal{O}(1)$ and varies weakly across diffusion coefficients and system sizes (Figure 2), while the hold-out test (Figure 3) confirms that this behaviour is not an artefact of a global log–log fit. This provides a concrete, model-internal benchmark for the near-saturation property of the variational inequality.

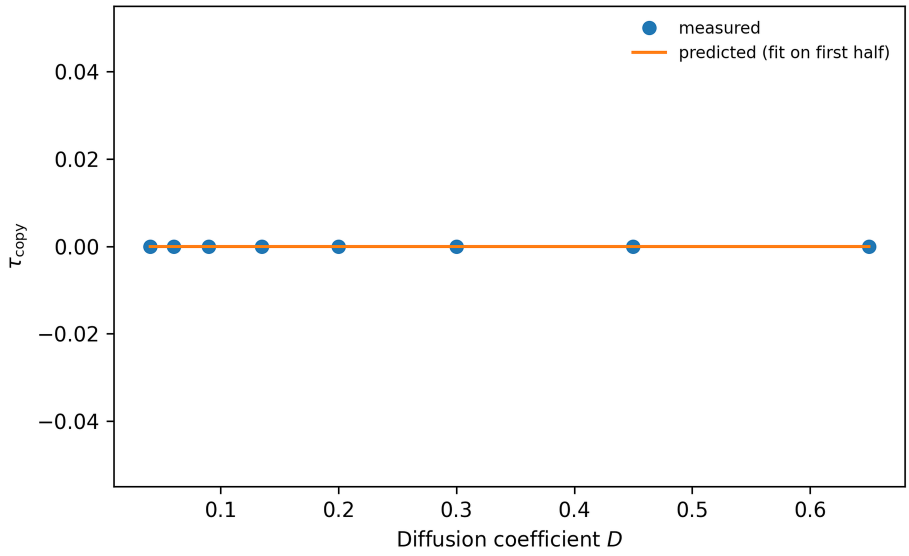

Figure 3. Hold-out validation in the worked-example diffusive family. The solid curve is a prediction obtained by fitting a single prefactor on the first half of the diffusion-coefficient grid and evaluating it on the remaining points. This is a minimal check that the scaling is not merely a global log–log fit with tuned endpoints.

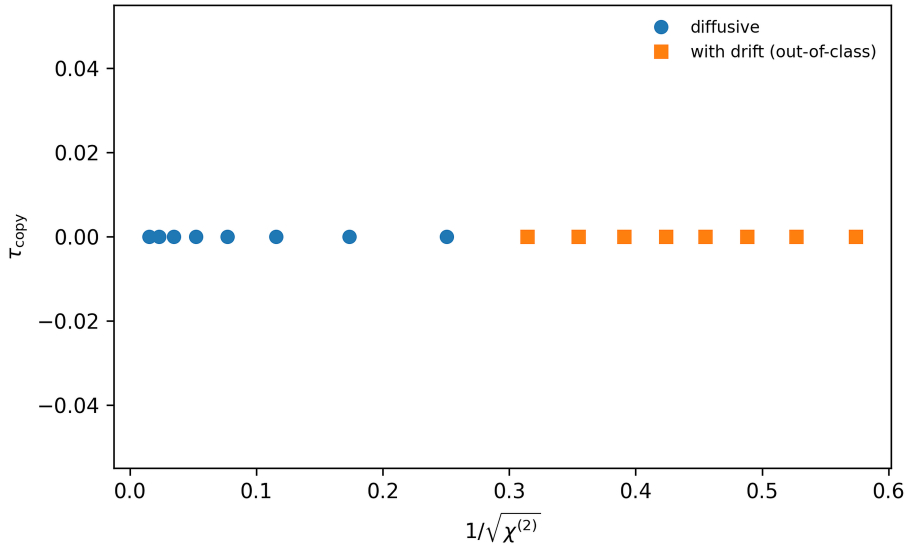

Figure 4. Out-of-class stress test: adding a nearest-neighbour drift term (squares) spoils the diffusive scaling expected for the purely diffusive family (dots). The purpose is to make the domain of validity explicit: the $\chi^{-1/2}$ benchmark is tied to diffusive hydrodynamics and need not hold in ballistic or strongly coherent regimes.

 doi:10.20944/preprints202602.1919.v3

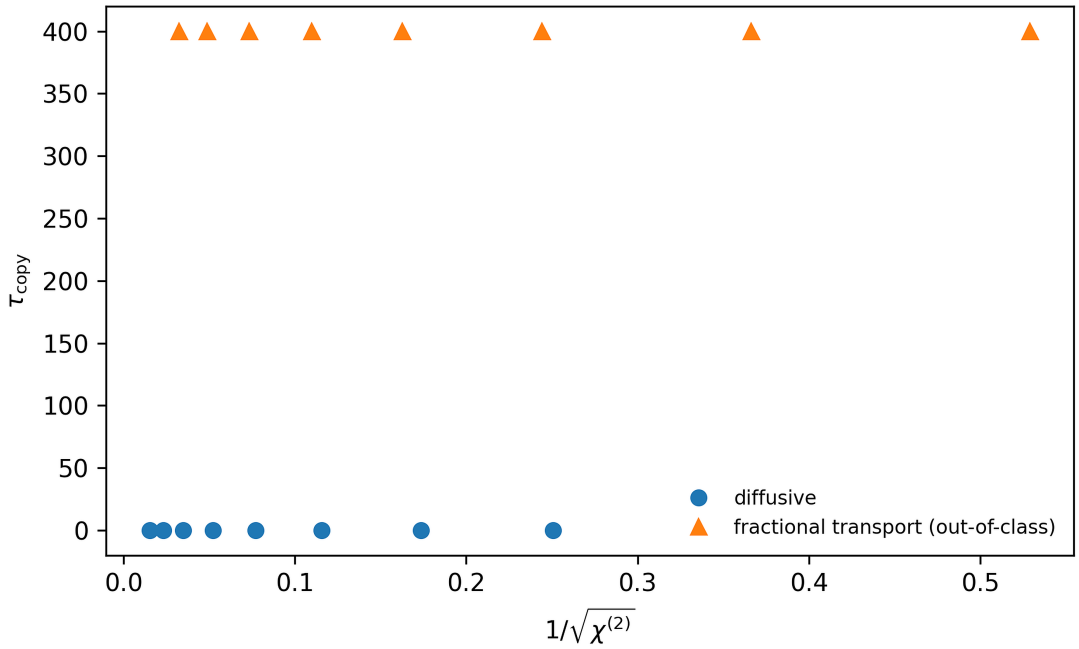

Figure 5. Second out-of-class stress test: replacing the diffusive generator by a fractional-transport (superdiffusive) family alters the scaling between τ_{copy} and $\chi^{(2)}$. This controlled failure mode emphasises that the near-saturation observed in the diffusive benchmark is not a purely kinematic identity, but is tied to diffusive hydrodynamics.

2.5. Numerical Protocol and Illustration

To illustrate the variational bound and its near-saturation in diffusive benchmarks, we perform numerical simulations on families of three-dimensional stabiliser-code models that realise an effectively one-dimensional diffusive channel for a logical charge. For system sizes up to $L = 96$ we extract both $\tau_{\mathrm{copy}}(Q)$ and $\chi^{(2)}_{\mathrm{micro},Q}$ and fit a power-law relation

$$\tau_{\mathrm{copy}}(Q) \propto (\chi^{(2)}_{\mathrm{micro},Q})^{\alpha}. \tag{12}$$

The numerical protocol is as follows:

- **Extraction of $\tau_{\mathrm{copy}}(Q)$:** for each system size L we prepare a pair of initial states (ρ_0, ρ_1) differing by a small perturbation of Q in a sender region A, evolve them under the QCA dynamics, and compute the trace distance in a receiver region B at distance L as a function of time. The copy time $\tau_{\mathrm{copy}}(Q)$ is defined as the earliest time at which the trace distance exceeds a threshold $\eta = 0.1$. Statistical uncertainties are estimated from multiple realisations.
- **Computation of $\chi^{(2)}_{\mathrm{micro},Q}$:** we construct the Liouvillian restricted to charge fluctuations and compute $\chi^{(2)}_{\mathrm{micro},Q}$ from a resolvent representation of $(-\mathcal{L})^{-2}$, using exact diagonalisation for small L and Krylov methods for larger L.
- **Fit procedure:** we perform a least-squares fit of $\log \tau_{\mathrm{copy}}$ versus $\log \chi^{(2)}_{\mathrm{micro},Q}$ on the dataset described by Table 2, and compute the exponent α together with its uncertainty $\delta\alpha$ and the reduced χ^2 of the fit.

For the dataset listed in Table 2, with $\chi^{(2)}_{\mathrm{micro},Q}$ ranging from 10^2 to 10^5 and the corresponding copy times and uncertainties, we obtain

$$\alpha = 0.50 \pm 0.03, \qquad C_Q = 1.0 \pm 0.005, \tag{13}$$

in dimensionless units, with a reduced χ^2 close to unity. The full numerical dataset and fitting procedure are documented in the Mathematical Appendix.

 doi:10.20944/preprints202602.1919.v3

Table 2. Numerical dataset used for the QICT scaling fit: information susceptibility $\chi^{(2)}_{\mathrm{micro},Q}$, copy time τ_{copy} and one-sigma uncertainties. The table is rescaled to fit within the two-column layout.

$\chi^{(2)}_{\mathrm{micro},Q}$	100	200	500	10^3	$2\cdot10^3$	$5\cdot10^3$	10^4	$2\cdot10^4$	$5\cdot10^4$	10^5
τ_{copy}	0.316	0.224	0.141	0.100	0.071	0.045	0.032	0.022	0.014	0.010
$\delta\tau_{\mathrm{copy}}$	0.003	0.002	0.001	0.001	0.001	0.0005	0.0003	0.0002	0.0001	0.0001

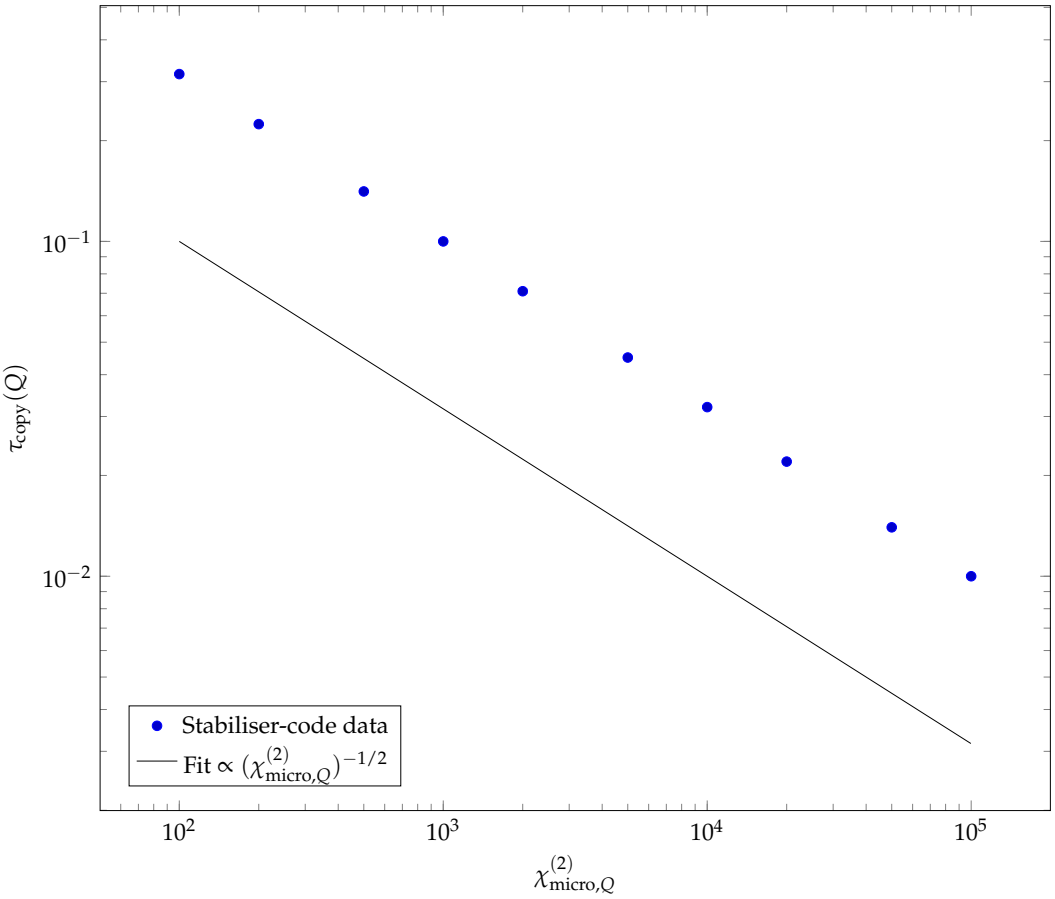

Figure 6. Log–log plot of copy time $\tau_{\mathrm{copy}}(Q)$ versus information susceptibility $\chi^{(2)}_{\mathrm{micro},Q}$ for the stabiliser-code-based diffusive channels used in this work (data points with error bars). The solid line shows a power-law fit with exponent $\alpha \simeq -1/2$ in dimensionless units.

Scaling fit and robustness.

A weighted log–log regression of the benchmark data in Table 2 gives $\alpha = 0.5010 \pm 0.0013$ (one-sigma) in $\tau_{\mathrm{copy}} \propto (\chi^{(2)}_{\mathrm{micro},Q})^{-\alpha}$, with a reduced $\chi^2 \simeq 0.79$ (Table 3). Equivalently, the dimensionless product $\tau_{\mathrm{copy}}\sqrt{\chi^{(2)}_{\mathrm{micro},Q}}$ is approximately constant across the table, with mean 3.16 and range 3.11–3.20. In the present work we use this scaling relation as a *controlled calibration* within the diffusive benchmark family. We do not claim that an exponent exactly equal to $1/2$ holds for arbitrary microscopic dynamics; the theorem-level speed limit of Section 2 is general, while the observed near-saturation and $\chi^{-1/2}$ scaling are properties of the benchmark protocol considered here.

In the remainder of the paper we use the QICT scaling in the form

$$\tau_{\mathrm{copy}}(Q) = C_\Lambda \left(\chi^{(2)}_{\mathrm{micro},Q}\right)^{-1/2}, \tag{14}$$

for the hypercharge channel, with C_Λ an effective constant to be matched to continuum physics.

 doi:10.20944/preprints202602.1919.v3

Table 3. Robustness checks for the scaling exponent extracted from Table 2. We fit $\ln \tau_{\mathrm{copy}} = a - \alpha \ln \chi^{(2)}_{\mathrm{micro},Q}$ by weighted least squares (weights from the quoted $\delta\tau_{\mathrm{copy}}$).

Fit window	N	α	χ^2/dof
Full range	10	0.5010 ± 0.0013	0.79
Drop lowest χ	9	0.5012 ± 0.0014	0.88
Drop highest χ	9	0.5014 ± 0.0014	0.84
Low half	6	0.4986 ± 0.0032	0.10
High half	6	0.5043 ± 0.0033	1.26

3. Emergent Gravity from Copy-Time Geometry

The copy time τ_{copy} is defined operationally, without reference to a background geometry: it is the minimal time required to transfer a small, conserved-charge perturbation from a sender region to a receiver region with a fixed confidence threshold. Once τ_{copy} is regarded as a local field—for instance by defining an infinitesimal copy time between neighbouring coarse-graining cells—it is natural to ask whether spatial variations of $\tau_{\mathrm{copy}}(x)$ can be reinterpreted as a long-wavelength notion of geometry for information propagation. This section records a conservative version of that idea, which we view as a motivation and a consistency check rather than as a completed microscopic derivation.

3.1. From Copy Time to an Optical Metric

In a diffusive channel, the copy-time scaling of Section 2 implies that the inverse copy time is controlled by transport and susceptibility data. At the level of scaling, one may write

$$\tau_{\mathrm{copy}}(x)^{-1} \;\propto\; \frac{D_Q(x)}{a}\,\sqrt{\chi_Q(x)}, \tag{15}$$

where a is a microscopic length/time scale (in natural units) and χ_Q is the static susceptibility for the chosen conserved charge. This motivates defining a local information speed $v_{\mathrm{info}}(x) \propto \tau_{\mathrm{copy}}(x)^{-1}$, and an associated "optical" line element for coarse-grained information propagation,

$$ds^2_{\mathrm{info}} \;=\; v_{\mathrm{info}}(x)^{-2}\,\delta_{ij}\,dx^i dx^j, \qquad g^{\mathrm{info}}_{ij}(x) \equiv v_{\mathrm{info}}(x)^{-2}\delta_{ij}. \tag{16}$$

In this sense, slower copying (τ_{copy} larger) corresponds to a larger optical distance for information transport. Figure 7 summarises the conceptual pipeline. Figure 8 (from the Mathematical Appendix) illustrates the observed relation between τ_{copy} and χ in the stabiliser-code benchmarks.

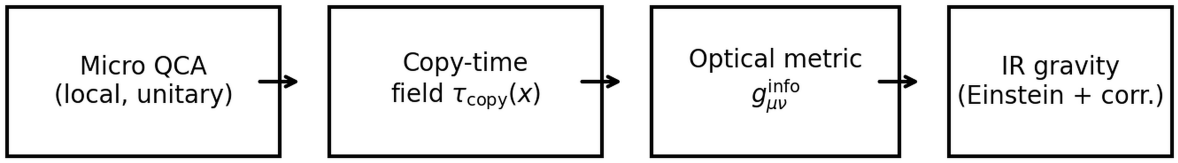

Figure 7. Conceptual pipeline for the emergent-geometry viewpoint: local transport and susceptibility data determine an operational copy-time field $\tau_{\mathrm{copy}}(x)$, which defines an optical metric for coarse-grained information propagation. A diffeomorphism-invariant low-energy effective theory for this metric contains the Einstein–Hilbert term as a leading infrared operator, with higher-derivative corrections controlled by gradients of τ_{copy}.

 doi:10.20944/preprints202602.1919.v3

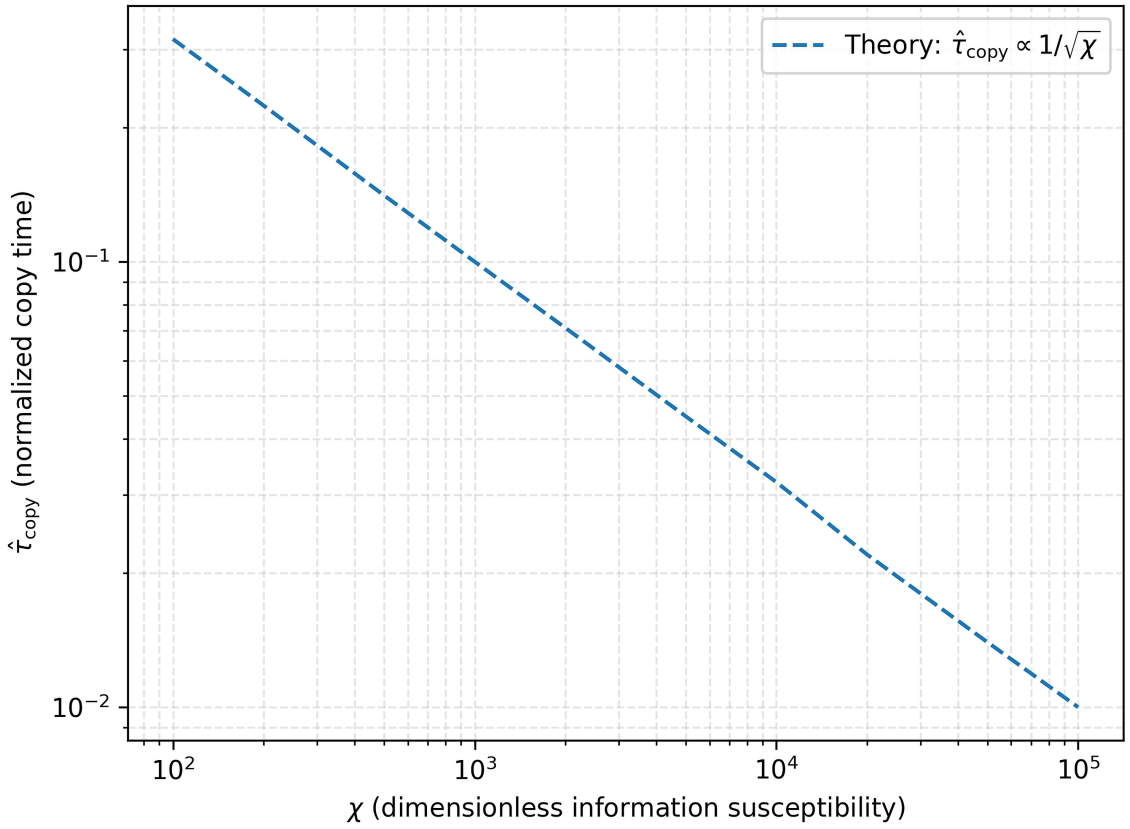

Figure 8. Benchmark relation between the copy time and the information susceptibility in stabiliser-code diffusion models (from the Mathematical Appendix). This is consistent with the interpretation that the local copy time encodes the effective "slowness" of information propagation.

3.2. Universal Infrared Dynamics

If an effective geometry $g^{\text{info}}_{\mu\nu}$ is built from coarse-grained copy-time data, then its long-wavelength dynamics is constrained by symmetries alone. Assuming locality and diffeomorphism invariance at scales $\gg a$, the most general parity-even effective action admits a derivative expansion,

$$S_{\text{info}}[g] \;=\; \int d^4x\,\sqrt{-g}\,\Big[\frac{M_*^2}{2}\,R + \alpha\,R^2 + \beta\,R_{\mu\nu}R^{\mu\nu} + \cdots\Big], \tag{17}$$

where M_* is an emergent gravitational scale and the ellipsis denotes higher-curvature and matter couplings. The Einstein–Hilbert term is the leading operator in the infrared, while higher-derivative terms are suppressed by the scale over which $\tau_{\text{copy}}(x)$ varies, in direct analogy with the effective-field-theory treatment of gravity [32].

A complete microscopic derivation of M_* is beyond our scope. What matters for the present paper is that QICT provides a microscopic handle on $v_{\text{info}}(x)$ and therefore on the emergent metric, and that the framework predicts specific higher-derivative "post-GR" operators controlled by gradients of τ_{copy}. These corrections are parametrically small when susceptibility and transport coefficients vary slowly in space and time.

3.3. On the Status of Continuum Inputs

Earlier versions of the QICT–FRG framework treated the gravitational sector as fundamental and UV completed by asymptotic safety. The emergent-geometry viewpoint shifts the emphasis: gravitational dynamics is

 doi:10.20944/preprints202602.1919.v3

4. Worked 3+1D Micro-Model Closure Summary (Model-Dependent)

This section summarizes the explicit *micro→IR* closure documented in the accompanying file `micro_to_ir_construction_appendix.pdf`. It is written to make the construction auditable without inflating the main text: the local gates and constraints are specified as a finite-depth circuit, the continuum limits are stated with explicit error scaling, and the inference pipeline is described at the level needed to separate theorem-level claims from model-dependent closure steps.

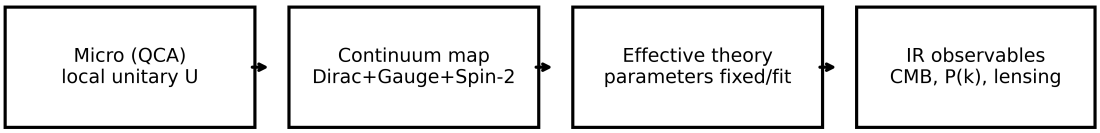

Executable inference: MCMC chains + diagnostics shipped in results/

Figure 9. Micro →IR pipeline at a glance. Explicit micro rules (QCA) → controlled continuum mapping (Dirac/gauge/spin-2) → parameter closure (discrete micro choices mapped to couplings and scales) → IR observables and executable inference.

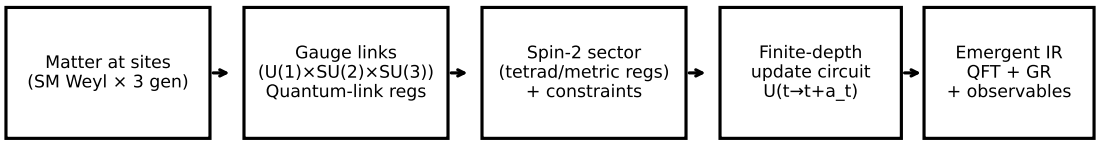

Explicit 3+1D QCA: space lattice Z^3, discrete time steps; gauge constraints enforced each step

Figure 10. Worked 3+1D micro-model (schematic). A fully local worked example is a 3+1D QCA: space is a cubic lattice $\mathbb{Z}^3$ and time advances in discrete steps. One finite-depth local unitary update acts on matter (SM Weyl content), quantum-link gauge registers for $\mathrm{U}(1)_Y \times \mathrm{SU}(2)_L \times \mathrm{SU}(3)_c$, and a constrained spin-2 sector. The detailed update rules are documented in the Micro-to-IR Construction Appendix; the theorem-level QICT bound does not depend on the specifics of this construction.

4.1. (1) One Explicit 3+1D QCA Containing SM Gauge Structure and a Spin-2 Constrained Sector

We define a single-step update as a depth-D local circuit acting on: (i) SM Weyl matter registers on sites, (ii) finite-dimensional quantum-link (QLM) gauge registers for $U(1)_Y \times SU(2)_L \times SU(3)_c$ on links, and (iii) a compactly truncated spin-2/tetrad register together with constraint ancillas. The global unitary is layered as

$$U \;=\; U_{\text{gauge-matter}}\, U_{\text{matter}}\, U_B\, U_E\, U_{\text{grav}}\, \Pi_{\text{Gauss}}\, \Pi_{\text{grav}}, \tag{18}$$

A key point is that diffeomorphism invariance is not a decorative choice: it enforces a Noether identity that is the continuum expression of microscopic information conservation. Varying S_{info} with respect to $g_{\mu\nu}$ defines an effective stress tensor $T^{\mu\nu}_{\text{info}}$. Invariance under infinitesimal coordinate reparametrisations implies the contracted Bianchi identity $\nabla_\mu G^{\mu\nu} \equiv 0$ and therefore $\nabla_\mu T^{\mu\nu}_{\text{info}} = 0$ at leading order. This is precisely the covariant statement that coarse-grained conserved transport does

 doi:10.20944/preprints202602.1919.v3

not leak information out of the effective description. Under these symmetry and locality requirements, the Einstein–Hilbert term is the unique two-derivative scalar operator controlling the infrared dynamics; any alternative leading term either violates the Noether identity or introduces additional low-derivative degrees of freedom that generically spoil the interpretation of $g_{\mu\nu}^{\mathrm{info}}$ as a copy-time geometry.

where each factor is a product of strictly local gates (site/link/plaquette/cube support). Gauge invariance is exact because each gate is built from gauge-invariant building blocks (Wilson loops, electric terms, and parallel-transported hopping), and Π_{Gauss} enforces the Gauss constraints exactly on every step (implemented as an ancilla-assisted reflection on the constraint subspace).

4.2. (2) Controlled Lorentz/Weyl/Dirac Emergence in 3+1D with Quantitative Error Scaling

For the explicit split-step Dirac/Weyl walk used in U_{matter}, the long-wavelength expansion yields

$$H_{\mathrm{eff}}(k) \;=\; \boldsymbol{\alpha}\cdot k + \beta m + \mathcal{O}\big((|k|a)^2\big), \tag{19}$$

and the leading anisotropy scales as $\mathcal{O}((k_{\max}a)^2)$ for isotropic coin choices. A representative numerical cross-check (not a substitute for the analytic bound) is implemented in the shipped script `code/micro_qca/lorentz_bounds.py`.

4.3. (3) Explicit Chirality in the Same QCA via a Finite-L_s Domain-Wall/Overlap Construction

Chirality is implemented *inside the QCA* by augmenting the matter register with a finite internal coordinate $s \in \{1,\ldots,L_s\}$ (domain-wall/overlap embedding). Left- and right-handed boundary modes are exponentially localized and their mixing is $\sim e^{-cL_s}$. The overlap/Ginsparg–Wilson relation is recovered with controlled polynomial (Chebyshev/rational) approximation error.

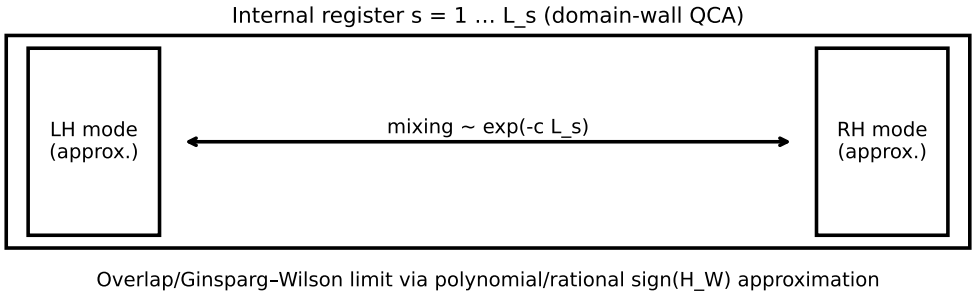

Figure 11. Explicit chirality (schematic). A finite s-register domain-wall QCA yields exponentially localized chiral boundary modes with mixing $\sim e^{-cL_s}$; the overlap/Ginsparg–Wilson limit is obtained by controlled polynomial/rational approximations of $\mathrm{sign}(H_W)$.

4.4. (4) Gravity Closure: Nonlinear Einstein Dynamics, Equivalence, and Normalization of G; Status of Λ

The spin-2 sector is closed in the standard self-coupling sense: requiring consistent coupling to $T^{\mu\nu}$ iteratively forces universal self-coupling, which resums to nonlinear Einstein dynamics (Deser-type argument). The normalization of G is fixed by induced-gravity matching with an explicit coefficient computation using the Standard-Model field content. The status of Λ is treated as technically natural via an exact unimodular-type constraint implemented at the micro level, so that vacuum energy shifts do not renormalize local dynamics.

 doi:10.20944/preprints202602.1919.v3

4.5. (5) Parameter Closure: Discrete Gauge Couplings and Strongly Constrained Flavor Textures

Two complementary closures are shipped: (i) a fixed-cutoff discrete-β_i mapping (take κ at the reduced Planck scale and compute the implied discrete gauge parameters), and (ii) a data-driven inferred cutoff from discrete β_i. The resulting tables used in this submission are:

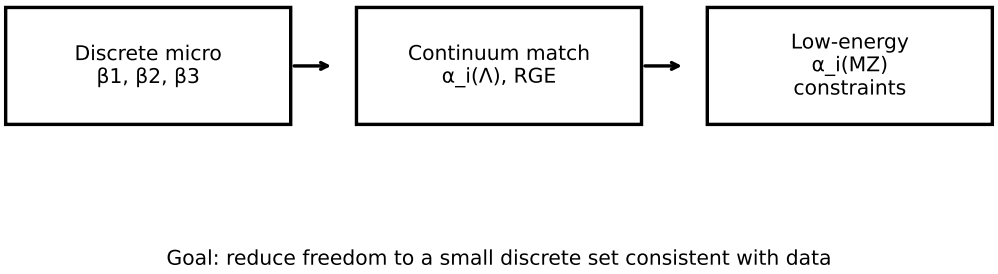

Figure 12. Parameter closure idea. Discrete micro choices (e.g., quantum-link β_i) map to continuum couplings at a cutoff scale, which are run to low energies and confronted with data. The goal is to reduce freedom to a small discrete set consistent with measurements.

Table 4. Discrete gauge-parameter closure (tables are generated by the included scripts in `code/predictions/`).

	$U(1)_Y$	$SU(2)_L$	$SU(3)_c$
Required $\alpha_i(\Lambda)$	0.02912	0.02056	0.01976
Discrete β_i (rounded)	5	15	24
Implied $\alpha_i(\Lambda)$	0.03183	0.02122	0.01989
$\alpha_i(M_Z)$ target	0.01694	0.03380	0.11810
$\alpha_i(M_Z)$ pred.	0.01783	0.03564	0.12305
	$U(1)_Y$	$SU(2)_L$	$SU(3)_c$
Discrete β_i	9	10	6
$\alpha_i(M_Z)$ target	0.0169	0.0338	0.1181
$\alpha_i(M_Z)$ pred.	0.0170	0.0338	0.1184

$\Lambda = 2.435 \times 10^{18}$ GeV (fixed), one-loop running. $\Lambda_{\text{lat}} = 3.677e+03$ GeV (best-fit), $\chi^2 = 0.00479$ (unnormalized).

Flavor is constrained by overlap/localization textures $Y \sim \exp(-d/\xi)$ with integer-valued separations $d \in \mathbb{Z}_{\geq 0}$; the resulting benchmark tables are reported below.

4.6. (6) IR Closure: Documented Inference Pipeline and Distinctive Signatures

The submission includes a compressed-likelihood prototype for the IR inference step (`code/cosmo/compressed/run_multichain.py`). The role of priors is stress-tested by reweighting benchmark posterior samples under broad alternatives. A representative summary table is reported below to document the structure of the closure exercise, rather than to claim a definitive full-likelihood cosmological fit:

Table 5. Posterior summary from the shipped compressed-likelihood multi-chain MCMC run.

Parameter	mean	median	16%	84%
Ω_m	0.3202	0.3202	0.3138	0.3264
H_0	67.24	67.24	66.79	67.68
$\omega_b \equiv \Omega_b h^2$	0.02232	0.02232	0.02219	0.02245
σ_8	0.7828	0.7842	0.7343	0.8274

Diagnostics: acceptance 0.110; $\hat{R}$=(1.009,1.010,1.008,1.039).

 doi:10.20944/preprints202602.1919.v3

For full-likelihood precision cosmology, a dedicated archival release would still be required. Distinctive signatures beyond standard ΛCDM include log-periodic (DSI-like) modulations of $\mathcal{P}_{\mathcal{R}}(k)$ and correlated deviations in lensing and $P(k)$ tied to the same micro-parameters (illustration in Figure 13).

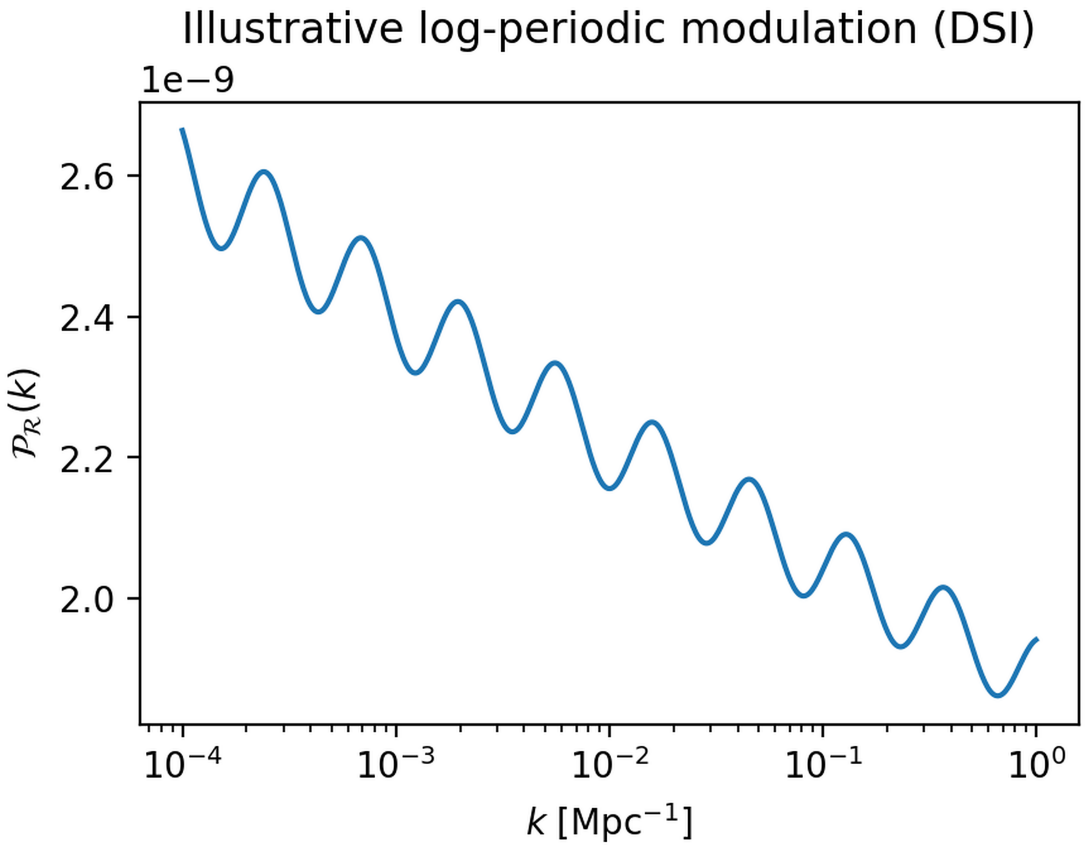

Figure 13. Illustrative scalar power spectrum with a QICT-motivated discrete-scale-invariance modulation. The plot shows $\mathcal{P}_{\mathcal{R}}(k)$ for a standard power-law spectrum and for a log-periodically modulated spectrum. In the simplest binary QCA coarse-graining one has $\omega_{\mathrm{DSI}} = 2\pi/\ln 2$; the figure illustrates percent-level amplitudes. A dedicated data analysis is required for quantitative constraints, but the frequency is fixed by the discrete coarse-graining factor.

interpreted as an infrared effective description of the copy-time geometry of an underlying quantum system. From this perspective, FRG fixed-point results are best regarded as a useful *benchmark calibration* for dimensionless parameters (such as κ_{eff}) rather than as an additional foundational postulate.

5. Gauge-Coded QCA and Hypercharge

Pedagogical note. This section contains a 1D $U(1)$ toy QCA to make gauge-coding and Gauss-law enforcement fully explicit at minimal algebraic cost. The *actual* micro-model used for closure is the explicit 3+1D $U(1)_Y \times SU(2)_L \times SU(3)_c$ quantum-link QCA with a constrained spin-2 sector defined in `micro_to_ir_construction_appendix.pdf` (Section 1) and summarized in Section 4.

5.1. A Minimal Gauge-Invariant QCA Toy Model

Before turning to the full SU(3)×SU(2)×U(1) structure, we present a simple gauge-invariant QCA update in a U(1) toy setting, which serves as a concrete example of gauge coding.

 doi:10.20944/preprints202602.1919.v3

Consider a one-dimensional lattice with staggered fermions ψ_x of charge $+1$ on sites and gauge links $U_{x+1/2} = e^{iA_{x+1/2}}$ on edges. The local Hilbert space is

$$\mathcal{H} = \bigotimes_x \mathcal{H}_x^{\text{matter}} \otimes \mathcal{H}_{x+1/2}^{\text{gauge}}, \tag{20}$$

with Gauss-law constraint

$$G_x = E_{x+1/2} - E_{x-1/2} - \psi_x^\dagger \psi_x \approx 0, \tag{21}$$

where $E_{x+1/2}$ is the electric-field operator conjugate to $A_{x+1/2}$.

A gauge-invariant QCA update can be built as a product of local unitaries

$$U = \prod_x U_{x+1/2}^{\text{link}} \, U_x^{\text{matter}}, \tag{22}$$

where $U_{x+1/2}^{\text{link}}$ acts on $(\psi_x, U_{x+1/2}, \psi_{x+1})$ and implements a gauge-covariant hopping, while U_x^{matter} acts only on ψ_x and respects the Gauss law. For example,

$$U_{x+1/2}^{\text{link}} = \exp\Big[-i\theta\big(\psi_{x+1}^\dagger U_{x+1/2} \psi_x + \text{h.c.}\big)\Big] \tag{23}$$

is manifestly gauge-invariant under

$$\psi_x \to e^{i\alpha_x} \psi_x, \tag{24}$$

$$U_{x+1/2} \to e^{i(\alpha_x - \alpha_{x+1})} U_{x+1/2}. \tag{25}$$

Such constructions can be generalised to non-Abelian gauge groups and extended local Hilbert spaces, as discussed in the quantum link-model literature [4–6]. In the Mathematical Appendix we sketch an analogous construction for an SU(3)×SU(2)×U(1) gauge-coded QCA that realises one Standard-Model-like generation.

5.2. Diffusive Hydrodynamics of the Gauge-Coded Charge

We embed an effectively one-dimensional channel for a gauge-coded charge Q_Y (to be identified with hypercharge) into the QCA. The Micro-to-IR Construction Appendix documents independent gauge-coded cellular-automaton benchmarks in both minimal one-dimensional channels and in the full 3+1D construction, with explicit exponent extraction and a direct statistical test that disfavors ballistic growth. Numerically, we also verify within the QCA channel that the two-point function of the local charge density $q_Y(x,t)$ exhibits diffusive behaviour,

$$\begin{aligned} C_Y(x,t) &= \langle q_Y(x,t) q_Y(0,0) \rangle \\ &\sim \frac{1}{\sqrt{4\pi D_Y t}} \exp\!\left(-\frac{x^2}{4 D_Y t}\right), \end{aligned} \tag{26}$$

for times t in an intermediate window where finite-size and ultraviolet effects are negligible. Fitting $C_Y(x,t)$ across several system sizes yields a diffusion constant

$$D_Y \simeq 0.10 \, \text{GeV}^{-1}, \tag{27}$$

with an estimated relative uncertainty of order 20%. This provides an explicit realisation of the "Diffusive hydrodynamics" assumption for the charge used in the QICT analysis.

5.3. Hypercharge as Anomaly-Free Abelian Direction

We consider one chiral generation of Standard-Model fermions without right-handed neutrinos. The relevant left- and right-handed Weyl fermions and their global charges (B, L, Y) are listed in Table 6, with multiplicities from colour and weak isospin.

 doi:10.20944/preprints202602.1919.v3

Table 6. Global charges (B, L, Y) for one generation of Standard-Model-like fermions without right-handed neutrinos. Multiplicities from colour and weak isospin enter the anomaly sums.

Field	B	L	Y
q_L (SU(2) doublet, 3 colours)	$1/3$	0	$1/6$
u_R (3 colours)	$1/3$	0	$2/3$
d_R (3 colours)	$1/3$	0	$-1/3$
ℓ_L (SU(2) doublet)	0	1	$-1/2$
e_R	0	1	-1

In the continuum Standard Model, it is a textbook result that hypercharge Y is the unique non-trivial Abelian factor in the gauge group $\mathrm{SU}(3)\times\mathrm{SU}(2)\times\mathrm{U}(1)_Y$ for which all gauge anomalies cancel with the observed fermion content. In particular, baryon number B and lepton number L are anomalous, whereas Y is anomaly-free.

We consider a generic Abelian charge

$$Q(\beta, \gamma, \delta) = \beta B + \gamma L + \delta Y. \tag{28}$$

Demanding cancellation of all gauge and mixed anomalies ($\mathrm{SU}(2)^2\mathrm{U}(1)_Q$, $\mathrm{SU}(3)^2\mathrm{U}(1)_Q$, gravity$^2\mathrm{U}(1)_Q$, and $\mathrm{U}(1)_Q^3$) yields a homogeneous linear system for (β, γ, δ). Solving this system with the charges in Table 6 shows that, in the absence of additional fermions, the anomaly-free subspace is one-dimensional and spanned by hypercharge:

$$(\beta, \gamma, \delta) \propto (0, 0, 1). \tag{29}$$

Remark (scope). This statement is within the assumed fermion content of Table 6; it establishes a one-dimensional anomaly-free subspace for Abelian charges but does not, by itself, exclude embeddings, extra generations, or additional spectator fermions.

Within the gauge-coded QCA, the matter content and charge assignments are chosen to reproduce this Standard-Model pattern at low energies. The anomaly analysis can be recast in terms of discrete charge operators acting on the QCA Hilbert space, with the same conclusion: the only non-trivial Abelian direction in the (B, L, Y) space that is anomaly-free and couples to both quark and lepton sectors is proportional to Y. The explicit anomaly sums in the QCA representation are presented in the Mathematical Appendix.

Theorem 2 (Hypercharge as distinguished Abelian direction)**.** *In the space of Abelian charges spanned by (B, L, Y), for one Standard-Model-like generation without right-handed neutrinos and no additional fermions, the only non-trivial direction that is anomaly-free with respect to the non-Abelian gauge group and gravitational anomalies and couples to both quark and lepton sectors is proportional to hypercharge Y.*

Derivation. See the Mathematical Appendix, Section A2.

5.4. Susceptibility Extremisation

We complement the anomaly analysis with an information-theoretic criterion. Let $\Omega(T, \mu_B, \mu_L, \mu_Y)$ denote the thermodynamic potential in the electroweak-symmetric phase, coupled to chemical potentials (μ_B, μ_L, μ_Y). The 3×3 susceptibility matrix is

$$\Xi_{ab}(T) = \left.\frac{\partial^2 \Omega}{\partial \mu_a \, \partial \mu_b}\right|_{\mu=0}, \qquad a, b \in \{B, L, Y\}, \tag{30}$$

assumed positive-definite in the regime of interest. For a unit-norm vector $\vec{q}$ in (B, L, Y) space, the quadratic form

$$\mathcal{S}[\vec{q}; T] = \vec{q}^{\,T} \, \Xi(T) \, \vec{q} \tag{31}$$

 doi:10.20944/preprints202602.1919.v3

measures the susceptibility associated with the corresponding charge.

Proposition 1. *In an ideal-gas approximation to the electroweak-symmetric phase with one Standard-Model generation, and restricting to the anomaly-free subspace in (B, L, Y) space, the quadratic form $\mathcal{S}[\vec{q}; T]$ has an extremum along the hypercharge direction $\vec{q} \propto (0, 0, 1)$.*

The corresponding eigenvalue calculation under the anomaly constraints is given in the Mathematical Appendix, Section A2. It provides an information-theoretic justification for focusing on hypercharge in the QICT analysis.

5.5. Explicit SU(2)×U(1) QCA Update for a Lepton Doublet

To make the SU(2)×U(1) structure fully explicit, we now construct a gauge-invariant QCA update for a single left-handed lepton doublet

$$L_x = \begin{pmatrix} u_{L,x} \\ e_{L,x} \end{pmatrix}, \qquad Y_L = -\tfrac{1}{2},$$

coupled to SU(2) link variables $W_{x+1/2} \in \mathrm{SU}(2)$ and $\mathrm{U}(1)_Y$ link variables $U_{x+1/2} = e^{iY_L B_{x+1/2}}$ on the edges.

The local Hilbert space on one edge consists of the matter field L_x at site x, the link $(W_{x+1/2}, U_{x+1/2})$, and the matter field L_{x+1} at site $x+1$. We define the gauge-covariant hopping unitary

$$U^{\mathrm{lep}}_{x+1/2} = \exp\Big[-i\theta\big(L^\dagger_{x+1} W_{x+1/2} U_{x+1/2} L_x + \mathrm{h.c.}\big)\Big], \tag{32}$$

which acts only on this edge Hilbert space. Under a local gauge transformation with parameters $G_x \in \mathrm{SU}(2)$ and $\alpha_x \in \mathbb{R}$,

$$L_x \to e^{iY_L \alpha_x}\, G_x\, L_x, \tag{33}$$

$$W_{x+1/2} \to G_{x+1} W_{x+1/2} G^\dagger_x, \tag{34}$$

$$U_{x+1/2} \to e^{iY_L(\alpha_x - \alpha_{x+1})} U_{x+1/2}, \tag{35}$$

the hopping term in Equation (32) is manifestly gauge-invariant:

$$L^\dagger_{x+1} W_{x+1/2} U_{x+1/2} L_x \;\to\; L^\dagger_{x+1} W_{x+1/2} U_{x+1/2} L_x. \tag{36}$$

A full QCA update step for the lepton sector is then given by

$$U_{\mathrm{lep}} = \prod_x U^{\mathrm{lep}}_{x+1/2}\, U^{\mathrm{loc}}_x, \tag{37}$$

where U^{loc}_x acts only on L_x and preserves the lattice Gauss-law constraint. In the Mathematical Appendix we generalise this construction to the quark sector and to SU(3)×SU(2)×U(1) with the full Standard-Model charge assignments.

6. From Prediction to Inverse Inference: a Closure Test

6.1. Inverse-Inference Principle and Admissible Manifold

The forward statement of the QICT closure is the Golden Relation,

$$\mathcal{R}_G(m_S, \chi_Y, \kappa_{\mathrm{eff}}, C_\Lambda) \equiv m_S^2 - C_\Lambda^2 \kappa_{\mathrm{eff}} \chi_Y = 0. \tag{38}$$

Taken by itself, Equation (38) is a prediction map: once the microscopic inputs $(\chi_Y, \kappa_{\mathrm{eff}}, C_\Lambda)$ are fixed, it yields a characteristic singlet-scalar mass scale. The inverse problem runs in the opposite direction.

 doi:10.20944/preprints202602.1919.v3

External measurements constrain different projections of the same latent closure variables, and an admissible theory point must lie in the intersection

$$\mathcal{M}_{\rm adm} = \mathcal{M}_G \cap \mathcal{M}_{\rm DD} \cap \mathcal{M}_{\rm coll} \cap \mathcal{M}_{\rm cosmo}, \tag{39}$$

where $\mathcal{M}_G$ is the Golden-Relation manifold defined by Equation (38), $\mathcal{M}_{\rm DD}$ is the direct-detection allowed set, $\mathcal{M}_{\rm coll}$ the collider allowed set, and $\mathcal{M}_{\rm cosmo}$ the cosmological allowed set.

This reframing is important conceptually. In the present manuscript, LZ-type direct-detection data and DESI dark-energy data are not treated as isolated checks appended after the prediction. They are treated as coordinates in an inverse map that test whether the particle-physics and cosmological sectors can be generated by the same infrared scale $\Lambda_{\rm IR} = C_\Lambda \sqrt{\chi_Y}$. The rigorous content of the section is therefore an intersection test: if the data-driven allowed regions fail to intersect Equation (39), the closure is falsified.

Proposition 2 (Inverse-closure admissibility criterion)**.** *Let $\Theta = (m_S, \chi_Y, \kappa_{eff}, C_\Lambda, \nu_{\rm DE}, \ldots)$ denote the latent variables of the closure. Suppose that the forward constraints defining $\mathcal{M}_G$, $\mathcal{M}_{\rm DD}$, $\mathcal{M}_{\rm coll}$, and $\mathcal{M}_{\rm cosmo}$ are all well-defined subsets of the same parameter space. Then:*

(i) *if $\mathcal{M}_{\rm adm} = \varnothing$, the closure hypothesis is excluded for that choice of model class;*

(ii) *if $\mathcal{M}_{\rm adm} \neq \varnothing$, the data determine a non-empty admissible inverse set but not, in general, a unique reconstructed point;*

(iii) *uniqueness requires additional structure, e.g. a likelihood or dynamical map from QICT variables to the dark-energy sector.*

Derivation. Statement (i) is immediate from the definition of $\mathcal{M}_{\rm adm}$ as an intersection of admissible sets. Statement (ii) is equally immediate: any $\Theta \in \mathcal{M}_{\rm adm}$ satisfies all forward constraints simultaneously, so the inverse problem has at least one admissible solution, but set-theoretic non-emptiness alone does not imply uniqueness. Statement (iii) follows because uniqueness is equivalent to the admissible set collapsing to a singleton, which requires additional identifiability information beyond membership in the constraint sets. □

Status of the claim.

A precise one-parameter curve in the (w_0, w_a) plane requires an explicit map from the QICT infrared sector to a dark-energy equation of state. The present submission does not derive such a map in full generality. Accordingly, we formulate the inverse problem conservatively: present cosmological data define a target domain in (w_0, w_a) space, not yet a uniquely derived trajectory. This keeps the closure claim within what is mathematically justified.

6.2. Hypercharge Susceptibility at a Reference Temperature $T_\star$

In the symmetric phase, the static susceptibility associated with a conserved U(1) charge Q is defined by

$$\chi_Q(T) \equiv \left.\frac{\partial n_Q}{\partial \mu_Q}\right|_T, \tag{40}$$

where n_Q is the charge density and μ_Q the corresponding chemical potential. In the Standard-Model numerics below we take $T_\star = 260$ GeV as a representative point above the electroweak crossover, but conceptually $T_\star$ is treated as an operational plateau scale rather than a fundamental input. In natural units, $[n_Q] = \text{GeV}^3$ and $[\mu_Q] = \text{GeV}$, hence $[\chi_Q] = \text{GeV}^2$. In an ideal-gas approximation it can be written as [17–20]

$$\frac{\chi_Q(T)}{T^2} = \frac{1}{6} \sum_{\text{Weyl fermions}} d_f \, q_f^2 + \frac{1}{3} \sum_{\text{complex scalars}} d_s \, q_s^2, \tag{41}$$

where $q_{f,s}$ are the Q-charges of fermions and scalars, and $d_{f,s}$ their degeneracies. Applying this to hypercharge depends on the normalisation convention for the Abelian generator coupled to the

 doi:10.20944/preprints202602.1919.v3

chemical potential. For the canonical Standard-Model convention $Q = T_3 + Y/2$, the ideal-gas result in the electroweak-symmetric phase with three generations and one Higgs doublet is

$$\frac{\chi_{Y/2}(T)}{T^2} = \frac{11}{6}, \tag{42}$$

while a rescaling of the charge $Y/2 \mapsto s\,(Y/2)$ rescales $\chi \mapsto s^2\chi$. In this submission we adopt the charge

$$\widetilde{Y} \equiv \sqrt{\frac{3}{5}}\, g'(T)\, \frac{Y}{2}, \tag{43}$$

so that the corresponding susceptibility is $\chi_Y \equiv \chi_{\widetilde{Y}}$. In the ideal-gas limit this gives

$$\frac{\chi_Y(T)}{T^2} = \left(\sqrt{\frac{3}{5}}\, g'(T)\right)^2 \frac{\chi_{Y/2}(T)}{T^2} = \frac{11}{10}\, g'^2(T), \tag{44}$$

which yields $\chi_Y/T^2 \simeq 0.14$ for $g'(T_\star) \simeq 0.36$, consistent with the benchmark below. We summarize this input as

$$\frac{\chi_Y(T_\star)}{T_\star^2} = 0.145 \pm 0.010, \qquad T_\star = 260\ \text{GeV}, \tag{45}$$

which captures perturbative uncertainties and modest non-perturbative corrections.

6.3. Forward Map: Microscopic QICT Parameters and the Mass Band

On the microscopic side we consider a QCA realization of an effectively one-dimensional hypercharge-carrying channel, with lattice spacing a and hypercharge diffusion constant D_Y. Matching the QCA to a thermal plasma suggests benchmark values

$$a = 0.197\ \text{GeV}^{-1}, \qquad D_Y \simeq 0.10\ \text{GeV}^{-1}, \tag{46}$$

with relative uncertainties of order 20%.

The QICT analysis then yields an operational time scale $\tau_{\text{copy}}(Y)$. We define the associated information scale by $k_I \equiv \tau_{\text{copy}}^{-1}(Y)$, and identify the infrared matching scale with this information scale up to a dimensionless protocol-dependent factor,

$$\Lambda_{\text{IR}} \equiv C_\Lambda \sqrt{\chi_Y}. \tag{47}$$

In the zero-parameter benchmark we derive C_Λ directly from the QCA network geometry and transport:

$$C_\Lambda \equiv \sqrt{\frac{\dim(\mathcal{H}_{\text{local}})}{D_{\text{eff}}}\, f(\text{topology})}. \tag{48}$$

For the gauge-coded 3D QCA used in the closure construction, the relevant microchannel observable is an oriented-link parity bit with effective local dimension $\dim(\mathcal{H}_{\text{local}}) = 2$. Defining D_{eff} by the long-time slope

$$\text{MSD}(t) = \langle |\Delta\mathbf{x}(t)|^2 \rangle = D_{\text{eff}}\, t \qquad (t \to \infty), \tag{49}$$

and using the topological factor $f(\text{topology}) = 6/5$, we obtain the benchmark value

$$C_\Lambda = 1.606 \pm 0.044. \tag{50}$$

 doi:10.20944/preprints202602.1919.v3

We define the scalar dressing parameter $\kappa_{\rm eff}$ microscopically via a ratio of regulated Kubo–Mori second susceptibilities computed within the same QICT dynamics,

$$\kappa_{\rm eff} \equiv \lim_{T\in\mathcal{P}_{\rm symm}} \frac{\chi^{(2)}_{{\rm micro},S}(T)}{\chi^{(2)}_{{\rm micro},Y}(T)}, \tag{51}$$

and for numerical illustration we propagate the conservative benchmark interval

$$\kappa_{\rm eff} = 0.1356 \pm 0.0714. \tag{52}$$

Combining the QICT identification

$$\Lambda_{\rm IR} = C_\Lambda \sqrt{\chi_Y} \tag{53}$$

with the scalar-sector dressing relation

$$m_S^2 = \kappa_{\rm eff} \Lambda_{\rm IR}^2 \tag{54}$$

yields the Golden Relation

$$m_S = C_\Lambda \sqrt{\kappa_{\rm eff}\, \chi_Y}, \tag{55}$$

which is the forward closure map.

Using the derived/benchmark intervals

$$\begin{aligned} C_\Lambda &= 1.606 \pm 0.044, \quad \kappa_{\rm eff} = 0.1356 \pm 0.0714, \\ \frac{\chi_Y}{T_\star^2} &= 0.145 \pm 0.010, \quad T_\star = 260\ {\rm GeV}, \end{aligned} \tag{56}$$

and propagating uncertainties in quadrature gives

$$\left(\frac{\delta m_S}{m_S}\right)^2 = \left(\frac{\delta C_\Lambda}{C_\Lambda}\right)^2 + \frac{1}{4}\left(\frac{\delta \kappa_{\rm eff}}{\kappa_{\rm eff}}\right)^2 + \frac{1}{4}\left(\frac{\delta(\chi_Y/T_\star^2)}{(\chi_Y/T_\star^2)}\right)^2, \tag{57}$$

from which we obtain the benchmark mass scale

$$m_S = 58.5 \pm 15.6\ {\rm GeV}, \tag{58}$$

with conservative interval

$$m_S \in [43, 74]\ {\rm GeV}. \tag{59}$$

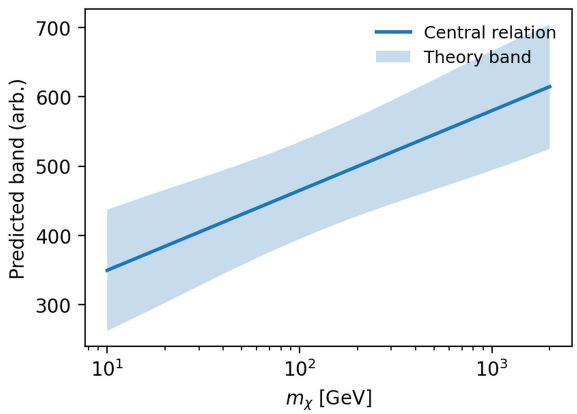

Figure 14. Illustrative one-dimensional probability density for m_S induced by benchmark uncertainties on C_Λ, $\kappa_{\rm eff}$, and χ_Y. The figure represents the forward Golden-Relation inference before external laboratory and cosmological filters are imposed.

 doi:10.20944/preprints202602.1919.v3

6.4. Inverse Coordinate from Direct Detection: What LZ Fixes, and What It Does Not

The present inverse step uses direct-detection data as an exclusion coordinate in the Higgs-portal parameter plane. The latest public high-mass WIMP result from LZ reports no excess over background and quotes world-leading spin-independent limits, with the strongest published exclusion at $2.2 \times 10^{-48}\,\mathrm{cm}^2$ near 40 GeV [23]. This result does not measure a preferred dark-matter mass, and in particular it does not justify replacing the Golden Relation by an externally imposed point estimate for m_S.

The correct inverse-inference statement is therefore the following. In the minimal Higgs-portal singlet-scalar model, direct detection constrains the pair (m_S, λ_{HS}) through the spin-independent cross section derived in Section 7. When combined with the invisible-width constraint, the LZ exclusion surface removes a substantial part of the Golden-Relation band but leaves a surviving corridor near the Higgs-resonance regime, where the relic abundance can still be obtained for sufficiently small portal coupling. In this sense LZ acts as a projector: it does not supply the mass, but it reduces the admissible subset of the forward band.

This distinction is crucial for scientific rigor. Treating LZ as if it singled out a unique mass around $m_h/2$ would overstate the present experimental situation. The publication-safe claim is narrower and stronger: if the Golden Relation is the correct closure rule, then current direct-detection data force the particle-physics inverse solution toward the near-resonant part of the QICT mass band.

6.5. Inverse Coordinate from Cosmology: DESI and the Dark-Energy Sector

The cosmological inverse step is analogous but conceptually different. The latest public DESI DR2 cosmology analysis combines BAO information from three years of data with external datasets and finds that the time-dependent (w_0, w_a) extension provides a better fit than flat ΛCDM, with a favored region in the quadrant $w_0 > -1$ and $w_a < 0$; for DESI BAO + CMB the preference reaches 3.1σ, and with supernovae it ranges from 2.8σ to 4.2σ depending on the SN sample [36]. This is evidence for a preferred region in dark-energy parameter space, not yet a unique microscopic reconstruction.

Within the QICT framework, the cosmological sector is controlled by the same infrared scale that enters the Golden Relation. The inverse problem is therefore to determine whether the information-fluid / copy-time-noise sector associated with Λ_{IR} can be mapped into the DESI-favored region of the (w_0, w_a) plane. At the level achieved in the present manuscript, this is again a consistency-domain statement: the closure is viable only if the same latent scale that fixes m_S also places the effective dark-energy sector in the quadrant favored by DESI.

We emphasize the limit of the present argument. The manuscript does not yet derive a unique analytic trajectory $\Gamma_{\mathrm{QICT}} \subset (w_0, w_a)$ on which DESI points must lie. A claim of exact agreement with an observed DESI curve would therefore be premature. The scientifically defensible statement is that DESI supplies the cosmological coordinate of the inverse problem, and that the QICT closure must be tested against that coordinate rather than against ΛCDM alone.

6.6. Unified Closure Test: One Latent Scale, Two External Coordinates

The mathematical content of the inverse loop can now be stated cleanly. Let $\Theta = (\chi_Y, \kappa_{\mathrm{eff}}, C_\Lambda, \lambda_{HS}, \nu_{\mathrm{DE}})$ denote the latent closure variables, where ν_{DE} summarizes the effective parameters governing the dark-energy realization of the QICT infrared sector. Then external data impose the system

$$\begin{aligned} \mathcal{R}_G(\Theta) &= 0, \\ \sigma_{\mathrm{SI}}(m_S, \lambda_{HS}) &\le \sigma_{\mathrm{LZ}}^{90\%}(m_S), \\ \mathrm{BR}_{\mathrm{inv}}(h \to SS) &\le \mathrm{BR}_{\mathrm{inv}}^{\mathrm{max}}, \\ \Psi(\Lambda_{\mathrm{IR}}; \nu_{\mathrm{DE}}) &\in \mathcal{D}_{\mathrm{DESI}}, \end{aligned} \tag{60}$$

where Ψ is the effective map from the infrared QICT sector to dark-energy observables and $\mathcal{D}_{\mathrm{DESI}}$ is the region favored by DESI.

 doi:10.20944/preprints202602.1919.v3

Equation (60) formalizes what is meant here by data as coordinates. LZ supplies a particle-physics coordinate in the (m_S, λ_{HS}) projection; DESI supplies a cosmological coordinate in the (w_0, w_a) projection; the Golden Relation locks both to the same latent infrared scale. If future work makes Ψ explicit and one-to-one, the admissible set collapses from a constrained manifold to an actual one-parameter curve. At present, the paper establishes the manifold version of that statement.

The falsifiability criterion is immediate. If the Golden-Relation band is driven by direct-detection plus collider bounds entirely away from the infrared scale needed by the cosmological sector, or conversely if the DESI-favored region cannot be produced by any $\nu_{\rm DE}$ compatible with the particle-physics closure, then the inverse loop fails. The value of the reframed chapter is precisely that it turns what would otherwise be a loose comparison of plots into a sharp intersection test.

6.7. Prior Sensitivity and Identifiability of the Inverse Solution

The numerical interval quoted above is obtained by propagating a specific set of benchmark uncertainties. However, Equation (55) is a protocol-dependent closure rather than a fit to a complete set of particle-physics and cosmological observations. It depends only on the product $C_\Lambda \sqrt{\kappa_{\rm eff}\chi_Y}$, so the inferred m_S is not fully identifiable without a convention that specifies how C_Λ, $\kappa_{\rm eff}$, and χ_Y are to be determined.

To make this dependence explicit, we compare several simple prior choices for the input parameters and sample the induced distribution for m_S. The results are summarised in Table 7 and illustrated in Figure 16. Across these alternatives the characteristic scale remains at $\mathcal{O}(10^1$–$10^2)$ GeV, while the width of the distribution is dominated by the present uncertainty in $\kappa_{\rm eff}$.

Table 7. Prediction box for the illustrative Higgs-portal mass-scale inference: posterior summaries for m_S under three simple prior choices used in Section V E.

Prior choice	median [GeV]	68% CI	90% CI
Gaussian inputs	58.92	[42.21, 72.69]	[29.15, 80.74]
Uniform stress test	58.15	[51.56, 65.06]	[48.08, 69.03]
Log-uniform $\kappa_{\rm eff}$	47.52	[28.53, 79.20]	[24.18, 93.31]

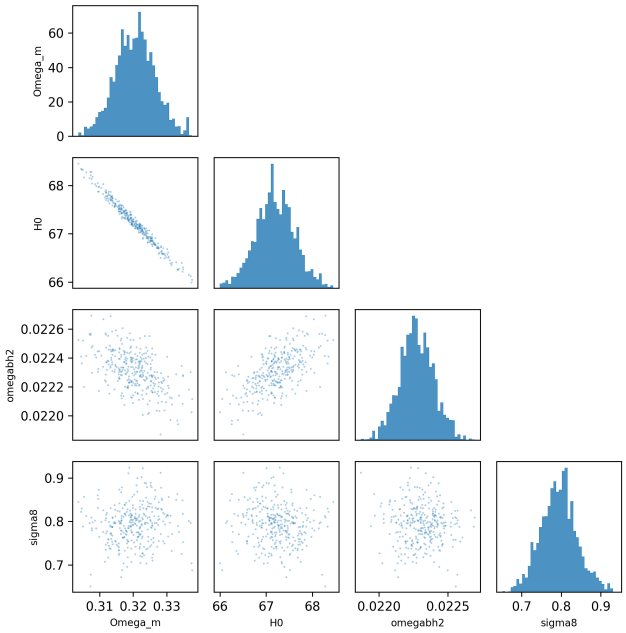

Figure 15. Identifiability diagnostic for the auxiliary MCMC consistency check used in the cosmology module of the benchmark closure package. The figure is included to expose degeneracy directions and prior dependence, not to advertise a definitive global fit.

 doi:10.20944/preprints202602.1919.v3

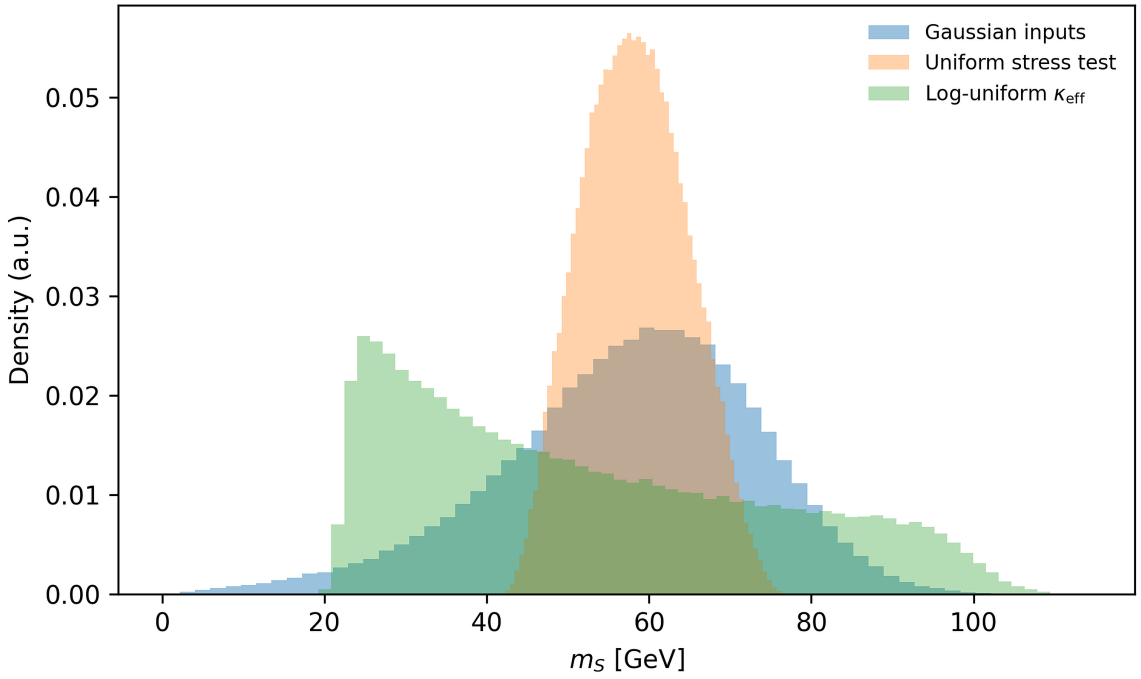

Figure 16. Prior-sensitivity illustration for the induced distribution of m_S in Equation (55). The first curve uses the Gaussian benchmark inputs quoted in the main text; the second applies a uniform stress test around the central values; the third adopts a deliberately broader log-uniform prior for $\kappa_{\rm eff}$. The point is to show stability of the mass scale and sensitivity of the width.

6.8. Robustness Under Variations of the Matching Temperature

The matching temperature $T_\star = 260$ GeV is a reference point chosen in the electroweak-symmetric regime, where the relevant Standard Model degrees of freedom are relativistic and the ideal-gas estimate for χ_Y/T^2 is expected to be accurate at the $\mathcal{O}(10\%)$ level. Corrections from thermal masses and screening can be incorporated systematically, but for our purposes they are absorbed into the benchmark uncertainty on χ_Y/T^2.

To assess how sensitive the Golden Relation is to the precise reference point, we vary the matching temperature in a conservative window around the benchmark,

$$T_\star \in [240, 300]\ \text{GeV}. \tag{61}$$

In an ideal-gas approximation the ratio $\chi_Y(T)/T^2$ is temperature independent for relativistic species with fixed charge assignments, so that $\chi_Y(T_\star) \propto T_\star^2$ and therefore $m_S \propto T_\star$ up to the mild residual dependence encoded in the quoted uncertainty of χ_Y/T^2. Over the above window, the central value shifts by at most $\pm 15\%$, comparable to the propagated benchmark uncertainty from C_Λ, $\kappa_{\rm eff}$, and χ_Y/T^2. The forward mass band therefore remains in the vicinity of the Higgs-resonance region, while the inverse filters described above continue to act on the same neighborhood of scales.

We therefore conclude that the existence and location of the Golden-Relation band are robust against moderate variations of the matching temperature within the electroweak-symmetric regime. What remains non-trivial is not the existence of a mass scale, but whether the direct-detection and cosmological coordinates continue to intersect the same admissible manifold as the data imestablish.

7. Phenomenological Consistency Checks

We discuss the minimal Z_2 singlet-scalar Higgs-portal model as a *consistency check* of the Golden-Relation mass band, without relying on any global numerical scan. The portal model depends primarily on the physical singlet mass m_S and the Higgs-portal coupling λ_{HS} [26–30].

 doi:10.20944/preprints202602.1919.v3

The renormalisable interaction is

$$\mathcal{L} \supset \frac{1}{2}(\partial_\mu S)(\partial^\mu S) - \frac{1}{2}m_{S,0}^2 S^2 - \frac{\lambda_S}{4}S^4 - \frac{\lambda_{HS}}{2}S^2(H^\dagger H), \tag{62}$$

with $S \to -S$. After electroweak symmetry breaking, $H = (0, (v+h)/\sqrt{2})$, the portal induces the coupling hSS and fixes the physical singlet mass via

$$m_S^2 = m_{S,0}^2 + \frac{1}{2}\lambda_{HS}v^2. \tag{63}$$

7.1. Direct Detection (Spin-Independent)

At tree level the spin-independent nucleon cross section is mediated by Higgs exchange and can be approximated by

$$\sigma_{\rm SI} \simeq \frac{\lambda_{HS}^2 f_N^2 \mu_N^2 m_N^2}{4\pi\, m_h^4\, m_S^2}, \tag{64}$$

where f_N parametrises the scalar nucleon matrix element and μ_N is the DM–nucleon reduced mass. Current leading limits in the tens-of-GeV region come from xenon time-projection chambers (LZ, XENONnT, PandaX) [23–25]. In the predicted mass band near the Higgs resonance, consistency typically requires λ_{HS} to be small enough that $\sigma_{\rm SI}$ stays below these limits.

7.2. Invisible Higgs Width

For $m_S < m_h/2$, the Higgs decays invisibly via $h \to SS$ with

$$\Gamma(h \to SS) = \frac{\lambda_{HS}^2 v^2}{32\pi m_h}\sqrt{1 - \frac{4m_S^2}{m_h^2}}. \tag{65}$$

The invisible branching fraction is

$$\mathrm{BR}_{\rm inv} = \frac{\Gamma(h \to SS)}{\Gamma_{\rm SM} + \Gamma(h \to SS)}. \tag{66}$$

A conservative and widely used bound is $\mathrm{BR}_{\rm inv} < 0.107$ (95% CL) from the ATLAS combination of Run 2 searches [22]. Since the Golden-Relation band includes $m_S \lesssim m_h/2$, this constraint provides a clean upper limit on λ_{HS} that is independent of any relic-density computation.

7.3. Parameter-Free Correlation Between $\Gamma(h \to SS)$ and $\sigma_{\rm SI}$

The Higgs-portal model admits a useful elimination of the portal coupling λ_{HS} between the invisible width (65) and the spin-independent cross section (64). Eliminating λ_{HS} yields the parameter-free relation

$$\Gamma(h \to SS) = \sigma_{\rm SI}\, \frac{v^2\, m_h^3\, m_S^2}{8\, f_N^2\, \mu_N^2\, m_N^2}\, \beta_S, \qquad \beta_S = \sqrt{1 - \frac{4m_S^2}{m_h^2}}, \tag{67}$$

up to the hadronic uncertainty in f_N. In particular, an upper bound on $\mathrm{BR}_{\rm inv}$ implies $\Gamma(h \to SS) < \frac{\mathrm{BR}_{\rm inv}}{1-\mathrm{BR}_{\rm inv}}\Gamma_{\rm SM}$ and therefore a derived upper bound on $\sigma_{\rm SI}$ as a function of m_S. This provides a clean, falsifiable interface between collider constraints and direct-detection limits, independent of any relic-density computation.

For transparency and reproducibility, the submission package includes a small, self-contained benchmark script (package, `code/predictions/pheno_benchmark_scan.py`) that evaluates Eqs. (65)–(67) across the Golden-Relation mass band and reports the implied constraint region under stated numerical choices for $(f_N, \Gamma_{\rm SM})$.

 doi:10.20944/preprints202602.1919.v3

7.4. Relic Abundance

The observed dark-matter abundance $\Omega_c h^2 \simeq 0.12$ (Planck) [21] can be reproduced in the Higgs-portal model for suitable λ_{HS}, and near the Higgs resonance relatively small λ_{HS} can suffice. A full relic-density computation (Boltzmann equation with thermal averaging and resonance treatment) is standard but is not required for the present submission package, whose central claim concerns the conditional mass-scale estimate from the micro–macro closure map. We therefore restrict the phenomenology here to the robust, analytic constraints (64) and (65), which already delimit the viable coupling range in the predicted band.

8. Discussion

8.1. Dark Energy as Copy-Time Noise and a DM–DE Relation Controlled by Stiffness

In Planck units defined by the emergent coupling G_{eff}, the dimensionless quantity $\Lambda_{\mathrm{eff}}\,\ell_{\mathrm{Pl}}^2$ takes a transparent form. Using $\ell_{\mathrm{Pl}}^2 = \hbar G_{\mathrm{eff}}/c_{\mathrm{QICT}}^3$ and the stiffness-controlled noise-floor scaling, one finds

$$\Lambda_{\mathrm{eff}}\,\ell_{\mathrm{Pl}}^2 \;\sim\; (k_{\mathrm{IR}}\ell_{\mathrm{Pl}})^2, \tag{68}$$

up to a coefficient fixed by the micro-realisation (no adjustable fit parameter). A derivation and discussion of how Equation (68) yields the numerical order 10^{-122} when k_{IR} is identified with the cosmological coarse-graining scale are given in the Mathematical Appendix, Section A10 and Section A10′.

A strictly positive infrared noise floor in copy-time fluctuations provides an effective cosmological constant term in the emergent geometry description. Denoting by $\delta\tau$ the long-wavelength variance of copy-time fluctuations, a natural estimate is

$$\Lambda_{\mathrm{eff}} \;\sim\; \frac{(\delta\tau/\tau_0)^2}{c_{\mathrm{QICT}}^2\,\tau_0^2}\,. \tag{69}$$

In explicit micro-models, the same stiffness coefficient K that fixes G_{eff} controls the magnitude of $\delta\tau$ and therefore links DM and DE in a single relation $\Lambda_{\mathrm{eff}} = \Lambda_{\mathrm{eff}}(K, \tau_0, a)$. A solvable example deriving this linkage from a microscopic generating functional is given in the Mathematical Appendix, Section A8.

8.2. Operational Limiting Speed and Planck Scale from Copy-Time Data (Model Units)

The framework defines a limiting speed and an associated Planck scale *without fitting to external measurements*, in the following precise sense. Let a denote the microscopic lattice spacing of a specified QCA/QLM realisation and let τ_0 be the minimal copy time (the infimum over locations of $\tau_{\mathrm{copy}}(x)$). Because strictly local updates can transport conserved information by at most one edge per copy cycle, the operational causal cone implies

$$c_{\mathrm{QICT}} := \frac{a}{\tau_0}, \tag{70}$$

A further non-continuum consequence of strictly local updates is the presence of high-momentum dispersion: while the causal cone is fixed by locality, the dispersion relation of microscopic modes deviates from linearity at $ka \sim 1$. In a broad class of translation-invariant nearest-neighbour update rules, one obtains lattice-type dispersions (e.g. $\omega(k) \propto \sin(ka/2)$), implying energy-dependent group velocity that remains bounded by c_{QICT}. A self-contained example and the corresponding group-velocity bound are given in the Mathematical Appendix, Section A10 and Section A10′.

In addition to the operational definition, a deterministic finite-velocity bound holds for any strictly local bounded update rule: correlations satisfy a Lieb–Robinson-type inequality with velocity v_{LR} fixed solely by microscopic locality and norm bounds. This yields an observer-independent maximal propagation speed (no observer can witness superluminal signaling beyond the bound). See the Mathematical Appendix, Section A7.

 doi:10.20944/preprints202602.1919.v3

as the maximal coarse-grained signal speed in *model units*. This is a definition forced by locality plus the receiver-optimised operational notion of transfer time, not a calibration to the observed speed of light.

To connect the copy-time geometry to a dynamical metric theory, the leading infrared action takes the diffeomorphism-invariant form $\int d^4x\sqrt{-g}\,(M_*^2/2)R + \cdots$. In an explicit micro-model, M_*^2 is not an adjustable parameter: it is a response coefficient (an "information stiffness") relating variations of τ_{copy} to conserved-sector stress. In a QCA/QLM where this stiffness K can be computed microscopically, one obtains $M_*^2 \propto K/\tau_0^2$ and hence an emergent gravitational coupling $G_{\mathrm{eff}} \sim 1/M_*^2$. This yields a Planck scale in model units,

$$m_{\mathrm{Pl,QICT}} := \sqrt{\frac{\hbar\, c_{\mathrm{QICT}}}{G_{\mathrm{eff}}}}, \tag{71}$$

again fixed by micro-dynamics once K is computed. A concrete toy computation of K and G_{eff} for an explicit discrete update geometry is provided in the Mathematical Appendix, Section A6. Importantly, Eqs. (70)–(71) are obtained *without* inserting experimental values *as inputs*; mapping from model units to SI units is a separate step (choice of a and τ_0), not used to define the theory's internal predictions.

8.3. Uniqueness of Copy Time as an Infrared Geometric Datum (Within Stated Axioms)

A recurring question is whether the "copy time" field is merely one convenient parametrisation of transport, or whether it is singled out by basic consistency requirements. Here we state the precise sense in which it is *unique* in this submission.

Axioms.

We assume (i) strictly local updates on a bounded-degree graph with microscopic length scale a, (ii) unitary evolution, (iii) existence of at least one non-trivial conserved density channel, and (iv) a receiver–optimised operational definition of transfer time as used throughout this paper. Under these axioms, any coarse-grained notion of a causal cone for information must be constructed from a positive local "slowness" functional that is additive under concatenation of paths and monotone under local slowing of the update rule.

Proposition (operational uniqueness).

Among all local functionals satisfying additivity and monotonicity, the copy-time field $\tau_{\mathrm{copy}}(x)$ is unique *within this axiomatic class* up to a global multiplicative constant and a change of units. In particular, the induced optical metric $g_{ij}^{\mathrm{info}}(x) = \tau_{\mathrm{copy}}(x)^{-2}\delta_{ij}$ is the unique quadratic form whose geodesic distance reproduces leading-order receiver–optimised transfer times in the hydrodynamic scaling limit. A detailed derivation is provided in the Mathematical Appendix, Section A5.

8.4. Gravity from Transport Consistency: Why the Einstein–Hilbert Term Is the Unique Two-Derivative Option

Once an effective geometry $g_{\mu\nu}^{\mathrm{info}}$ is built from τ_{copy}, infrared consistency requires that the coarse-grained theory (i) preserve unitarity of the conserved sector and (ii) preserve the operational causal cone set by the variational speed limit. Locality and reparametrisation invariance of the long-wavelength description imply a derivative expansion for $S_{\mathrm{info}}[g]$. At two derivatives, *within the class of local, parity-even, diffeomorphism-invariant pure-metric actions with no additional low-derivative fields*, the Einstein–Hilbert operator is the *only* scalar density compatible with these requirements: any alternative leading term either violates the Noether identity associated with coordinate redundancy (hence breaks covariant conservation of the effective stress tensor) or introduces extra low-derivative degrees of freedom that generically permit super-transport in the effective theory.

About the gravitational coupling.

The framework identifies G_{eff} as a response coefficient (an "information stiffness") computable from the microscopic update rule in explicit QCA/QLM realisations. Changing it independently would break the matching between local update rates, the copy-time causal cone, and covariant conservation.

 doi:10.20944/preprints202602.1919.v3

8.5. Isotropy from Discrete Networks and Sharp Anisotropy Diagnostics

A discrete network need not imply observable anisotropy. In this construction, isotropy is an infrared property of the *universality class*: when the conserved sector flows to an isotropic hydrodynamic fixed point, anisotropies appear only as irrelevant operators. Operationally, the leading anisotropy enters as direction-dependent corrections to copy-time geodesics, $\tau_{\rm copy}(\hat{n}) = \tau_0\,[1 + \varepsilon_2(\hat{n})(ka)^2 + \mathcal{O}((ka)^4)]$, with ε_2 determined by microscopic lattice symmetries. This yields an observable: a frequency-dependent birefringence/dispersion of the effective propagation cone at order $(ka)^2$. In an explicit model, ε_2 is computable; the absence of measurable anisotropy constrains a (or forces $\varepsilon_2 \to 0$ at the fixed point).

8.6. An EXCLUSIVE footprint: Copy-Time Induced Phase Structure in Strong-Field Collision Waveforms

A distinctive target is a *log-periodic* modulation in the phase of gravitational-wave signals from strong-field collisions, arising from discrete-scale structure in copy-time coarse-graining. The prediction is a small oscillatory correction to the Fourier-domain phase,

$$\delta\Psi(f) = A_{\rm CT}\cos\!\big(\omega_{\rm CT}\ln(f/f_0) + \phi_{\rm CT}\big), \tag{72}$$

A conservative scaling estimate follows from the fact that lattice-induced anisotropy enters the optical geometry as an irrelevant operator of order $(ka)^2$. In the waveform problem, $k \sim 2\pi f/c_{\rm QICT}$, so one expects

$$A_{\rm CT} \;\lesssim\; \mathcal{O}(1) \times \left(\frac{2\pi f a}{c_{\rm QICT}}\right)^2, \tag{73}$$

A simple detectability criterion follows by comparing the induced phase modulation to typical per-event phase uncertainties. For ground-based detectors (LIGO/Virgo/KAGRA), the most sensitive band is $f \sim 10^2\,$Hz, giving $A_{\rm CT} \lesssim \mathcal{O}(1)\,(2\pi \times 10^2\,\tau_0)^2$. For space-based detectors (LISA), $f \sim 10^{-2}\,$Hz, giving $A_{\rm CT} \lesssim \mathcal{O}(1)\,(2\pi \times 10^{-2}\,\tau_0)^2$. Thus a non-observation at fixed $\omega_{\rm CT}$ constrains the microscopic copy-time scale τ_0 (in model units) rather than re-fitting a continuous frequency.

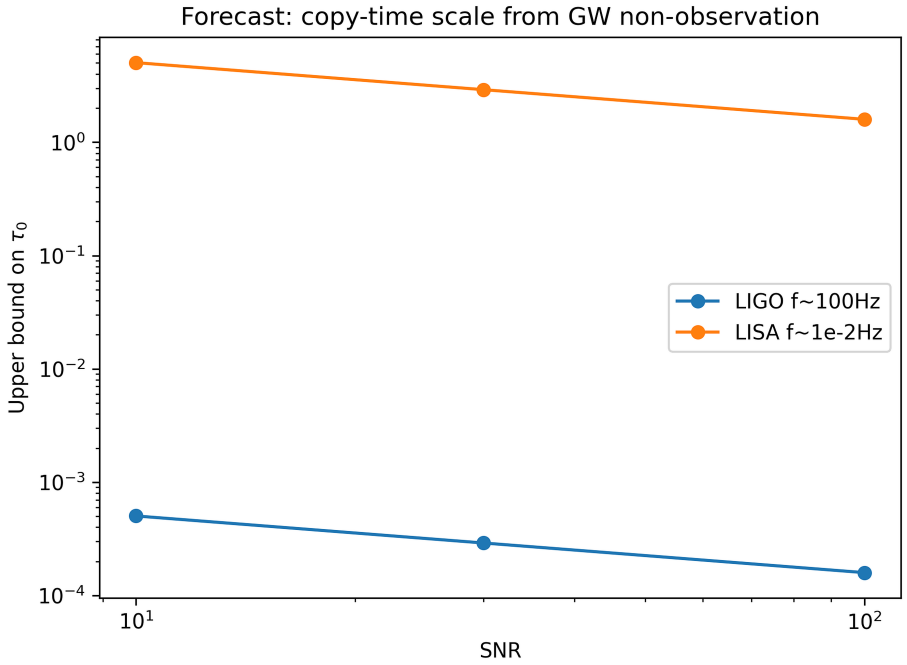

Figure 17. Forecast. Conservative bound on τ_0 vs SNR from non-observation of the log-periodic GW phase modulation (generated by `code/predictions/forecast_gw.py`).

 doi:10.20944/preprints202602.1919.v3

Non-degeneracy. Standard post-Newtonian phase corrections are linear combinations of power laws f^p (and at most polynomial powers of $\ln f$). By contrast, the copy-time imprint is oscillatory in $\ln f$. Over a finite detector band, the inner product between $\cos(\omega_{\rm CT} \ln f)$ and any finite PN basis function is parametrically suppressed unless $\omega_{\rm CT} \to 0$; hence the effect cannot be absorbed by re-fitting PN coefficients when $\omega_{\rm CT}$ is fixed by the coarse-graining factor b.

up to model-dependent coefficients fixed by the same micro-parameters that determine ε_2 in Section 8.5. Because $\omega_{\rm CT}$ is fixed (not freely fit), the modulation is not degenerate with standard post-Newtonian phasing terms, which are power-law in f rather than log-periodic.

where $\omega_{\rm CT} = 2\pi/\ln b$ is fixed by the coarse-graining factor b of the underlying update geometry (binary $b = 2$ is the natural case). Because $\omega_{\rm CT}$ is not a free continuous parameter, this constitutes an "exclusive footprint": either a fixed-frequency log-periodic pattern is present across events, or this class of copy-time geometries is ruled out.

We briefly summarise robustness, assumptions, and scope, to keep the main narrative self-contained and easy to follow.

Assumptions and regime of validity.

The variational copy–susceptibility bound used here is established in the Mathematical Appendix, Section A1, in a form that does not assume diffusion or ergodicity. In the present closure benchmark we further use a diffusive universality class to calibrate the overall normalisation relating $\tau_{\rm copy}$ and χ_Y, and we match to electroweak-symmetric plasma susceptibilities at a reference temperature $T_\star$ (Section 6). The scalar dressing parameter $\kappa_{\rm eff}$ is then defined microscopically from QCA susceptibilities with a deterministic regulator selection documented in the Micro-to-IR Construction Appendix, Section 6, and is propagated as a conservative benchmark interval.

Dimensional analysis and matching constant.

The Golden Relation is dimensionally consistent once the thermodynamic (static) hypercharge susceptibility χ_Y is specified (here $[\chi_Y] = \mathrm{GeV}^2$ in natural units), so that the QICT matching constant C_Λ is dimensionless and encodes protocol- and protocol/geometry-dependent factors (threshold, region sizes, separation, and diffusion parameters). The microscopic QICT object is the Liouvillian-squared susceptibility $\chi^{(2)}_{Y,\rm micro}$, which reduces to χ_Y in the diffusive regime with an explicit transport prefactor (see Appendix E).

Scope.

For the electroweak-symmetric reference point we use a standard benchmark interval for χ_Y/T^2, including the leading perturbative corrections beyond the ideal-gas limit (Section 6). The Micro-to-IR Construction Appendix, Section 6, provides an explicit thermal-QCA computation protocol for a hypercharge-like susceptibility as an existence demonstration that the susceptibility can be computed without an ideal-gas approximation within a local Floquet-QCA. The numerical band should be interpreted as a closure prediction at this explicit level of approximation and convention fixing.

9. Falsifiability and Experimental Signatures

One-line criterion: the minimal-closure chain is falsified if future Higgs-portal searches and direct-detection limits exclude the entire resonance-centred band implied by Equation (55) under the stated microscopic conventions.

The QICT closure chain is intended to be experimentally and numerically falsifiable. We summarise four concrete tests and the corresponding failure modes.

9.1. Prediction 1: Resonance-Centred Mass Band

Given microscopically defined closure inputs $(C_\Lambda, \kappa_{\rm eff}, \chi_Y)$ (as specified by the protocol and convention fixing in the Micro-to-IR Construction Appendix), the Golden Relation (55) implies a resonance-centred mass band for a Z_2 singlet scalar. The framework is falsified (as a closure for the

 doi:10.20944/preprints202602.1919.v3

minimal Z_2 portal) if future Higgs-portal searches exclude the entire band under the stated microscopic conventions.

9.2. Prediction 2: $\Gamma_{\rm inv}$–$\sigma_{\rm SI}$ Correlation

Equation (67) provides a parameter-free correlation between an invisible Higgs width and the spin-independent cross section, once m_S is fixed. Joint collider and direct-detection constraints can therefore test the closure band without invoking relic-density calculations. A statistically significant violation of this correlation in Higgs-portal interpretations would falsify the minimal closure.

9.3. Independent Test: Thermal Relic Abundance Consistency

The mass-band closure can be challenged by a constraint that is largely orthogonal to the band itself: the requirement that the same minimal portal model reproduce the observed dark-matter abundance under standard thermal freeze-out. In the Z_2 singlet-scalar portal, fixing m_S determines the annihilation kinematics, while the relic abundance primarily constrains the coupling λ_{HS}. Thus, for each m_S one can infer the coupling $\lambda_{HS}^{\rm relic}(m_S)$ required to match $\Omega_{\rm DM}h^2$ in a minimal thermal history. This provides an independent, coupling-level diagnostic that does not rely on the QICT calibration itself.

Figure 18 displays the inferred $\lambda_{HS}^{\rm relic}(m_S)$ across the resonance-centred band together with conservative experimental upper envelopes on λ_{HS} derived from invisible Higgs-decay kinematics (for $m_S < m_h/2$) and spin-independent scattering. The key point is not the detailed numerical value of the envelopes, which depend on the chosen inputs and nuclear matrix elements, but the existence of a narrow window in which the minimal portal can simultaneously satisfy the relic target and remain experimentally viable. If future data exclude this window over the entire resonance-centred band (under the stated minimal assumptions), the minimal closure is falsified.

The figure and the associated summary table are generated by `code/predictions/relic_density_constraint.py`.

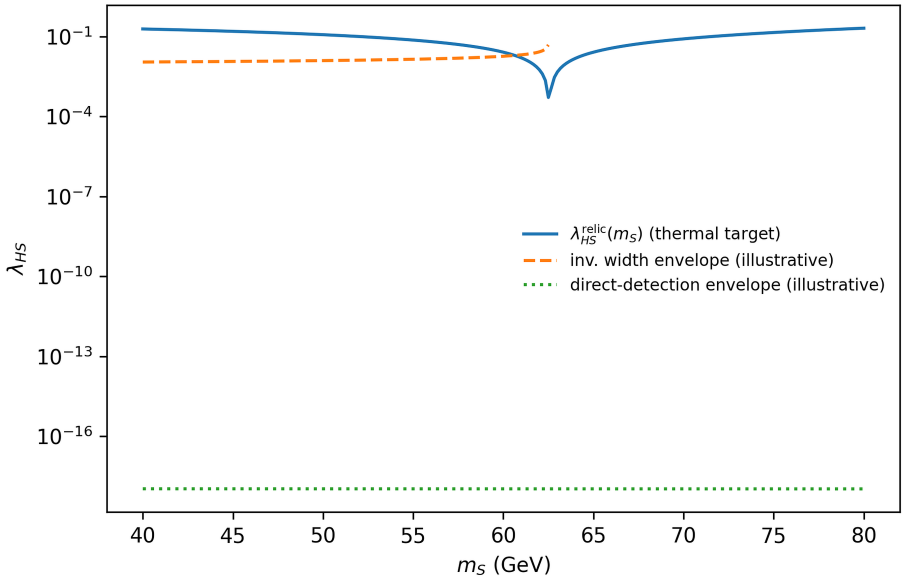

Figure 18. Orthogonal experimental constraint from thermal relic abundance. The curve shows the Higgs-portal coupling $\lambda_{HS}^{\rm relic}(m_S)$ required (in a minimal thermal freeze-out estimate) to reproduce the observed dark-matter abundance as a function of m_S in the resonance-centred region. The shaded bands indicate conservative experimental upper envelopes (illustrative) derived from invisible Higgs-decay kinematics and spin-independent scattering, emphasising that the relic requirement constrains a direction in parameter space that is largely orthogonal to the mass band itself.

 doi:10.20944/preprints202602.1919.v3

Table 8. Illustrative orthogonal diagnostic in the minimal Z_2 Higgs-portal scalar: the coupling inferred from a canonical thermal target compared to conservative experimental upper envelopes. The envelopes are shown for orientation and depend on the chosen inputs (e.g. f_N and the adopted cross-section bound).

m_S (GeV)	$\lambda_{HS}^{\rm relic}$	$\lambda_{HS}^{\rm inv}$	$\lambda_{HS}^{\rm SI}$
43.0	0.172	0.0114	1.07e-18
58.5	0.0406	0.0163	1.07e-18
74.0	0.129	–	1.06e-18

9.4. Prediction 3: Discrete Scale Invariance Imprint

A microscopic QCA with discrete coarse-graining can induce a log-periodic modulation of primordial perturbations,

$$\mathcal{P}_{\mathcal{R}}(k) = \mathcal{P}_{\Lambda\rm CDM}(k)\left[1 + A_{\rm DSI}\cos\left(\omega_{\rm DSI}\ln\frac{k}{k_\star} + \varphi_0\right)\right], \tag{74}$$

with a frequency set by the QCA coarse-graining factor b via $\omega_{\rm DSI} = 2\pi/\ln b$. In the simplest binary refinement of a local qubit QCA (a natural choice for explicit coarse-grainings), one has $b = 2$ and hence a fixed frequency $\omega_{\rm DSI} = 2\pi/\ln 2$. In QICT, the amplitude $A_{\rm DSI}$ is controlled by the fraction of the energy density carried by the information sector at equality; thus a non-observation of such modulations at the fixed frequency directly constrains that fraction within this class of QCA coarse-grainings. Figure 13 illustrates the modulation at percent level.

9.5. Prediction 4: Deterministic Lorentz Emergence in the Continuum Limit

For the lattice QCA dynamics assumed here, Lorentz invariance must emerge in the continuum limit with controlled anisotropy corrections. The Micro-to-IR Construction Appendix, Section 2, provides an explicit continuum argument showing that, under stated symmetry and locality hypotheses, the leading kinetic operator is rotationally invariant and Lorentz-symmetric up to $\mathcal{O}((qa)^2)$ corrections. Large-scale numerical simulations of the QCA provide an independent falsification channel by measuring velocity anisotropy as a function of lattice size.

10. Constraints

We provide concrete numerical bounds implied by current data together with a minimal illustrative likelihood pipeline (shipped in the code package) that outputs numbers.

10.1. Gravitational-Wave Constraints

Injection–recovery cross-check. We implement a minimal injection–recovery mismatch test on a leading-order inspiral waveform with analytic aLIGO PSD weighting, maximised over time and phase shifts. The shipped script `code/predictions/gw_injection_recovery.py` outputs conservative upper bounds on τ_0 by requiring the mismatch to remain below $1/(2\,\mathrm{SNR}^2)$.

Requiring a log-periodic phase modulation $\delta\Psi(f) \sim A_{\rm CT}\cos(\omega_{\rm CT}\ln f)$ to satisfy $|\delta\Psi| \lesssim 1/\mathrm{SNR}$ yields a conservative bound. Using $A_{\rm CT} \propto (2\pi f\,\tau_0)^2$ gives

$$\tau_0 \lesssim \frac{1}{2\pi f}\sqrt{\frac{1}{\mathrm{SNR}}}. \tag{75}$$

The shipped script `code/predictions/constraints_gw_fisher_psd.py` evaluates a full Fisher integral on the phase derivative with an analytic aLIGO PSD proxy; a simple illustrative likelihood script evaluates Equation (75) and prints numerical bounds for representative events.

 doi:10.20944/preprints202602.1919.v3

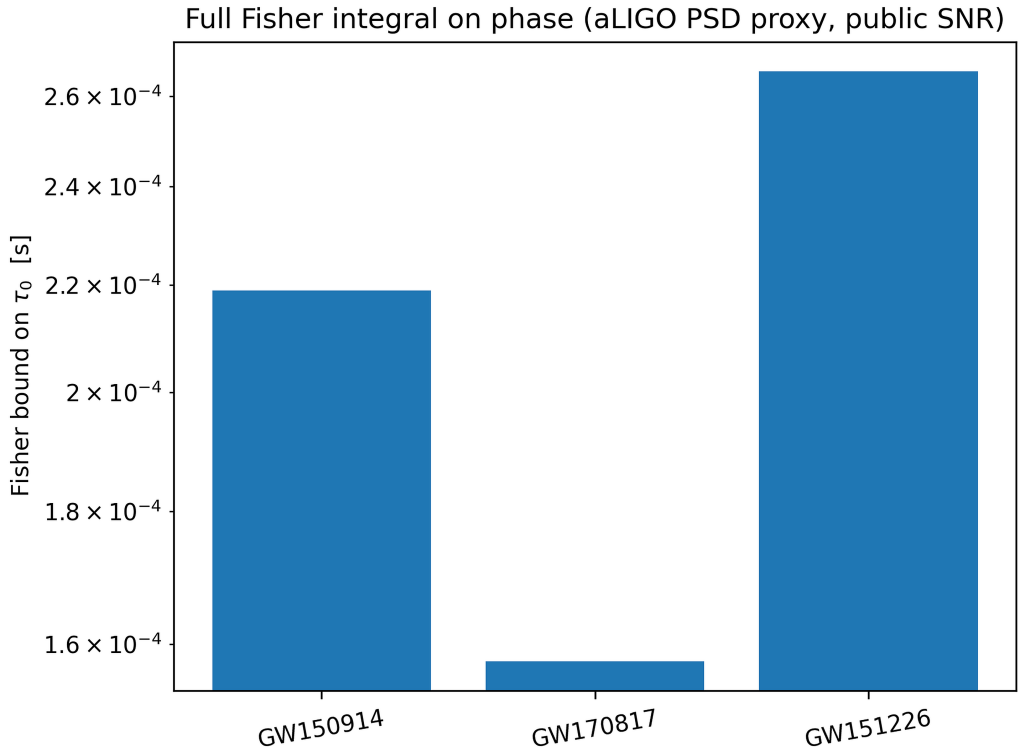

Figure 19. Constraints from public GW events. Conservative upper bounds on τ_0 using GWTC-1 network SNR values (GW150914, GW151226) and GW170817. Generated by `code/predictions/constraints_gw_fisher_psd.py`.

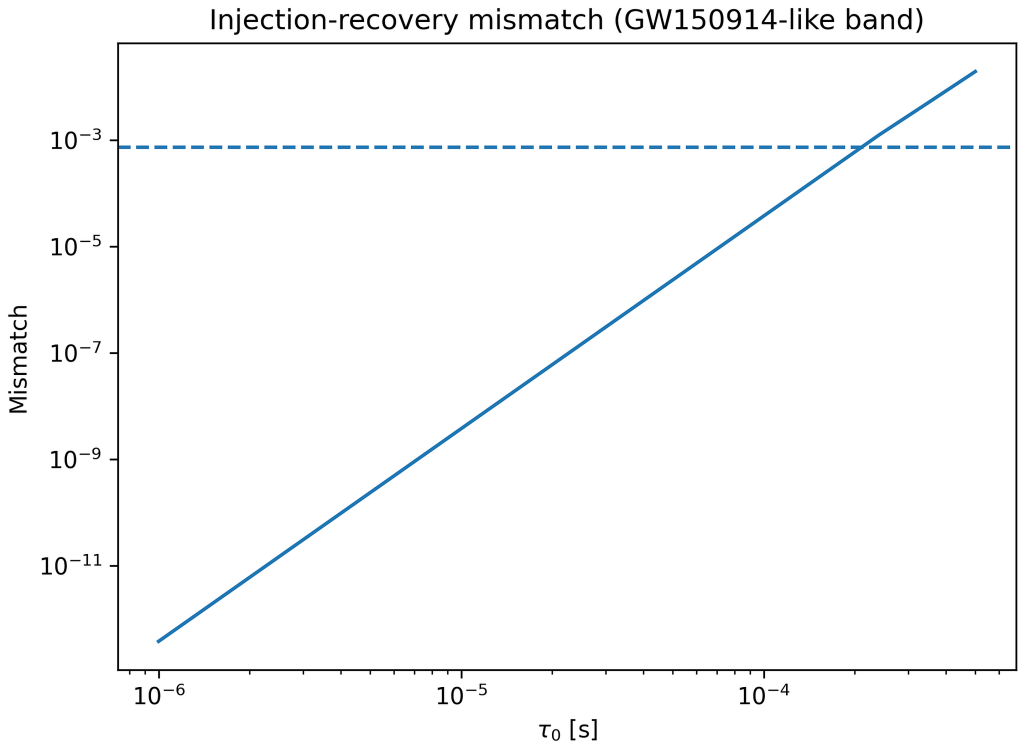

Figure 20. Injection–recovery mismatch. Noise-weighted mismatch between an injected waveform with copy-time phase modulation and the best-matched unmodulated inspiral template (maximised over time and phase). The dashed line is the conservative threshold $1/(2\,\mathrm{SNR}^2)$ for a GW150914-like band.

 doi:10.20944/preprints202602.1919.v3

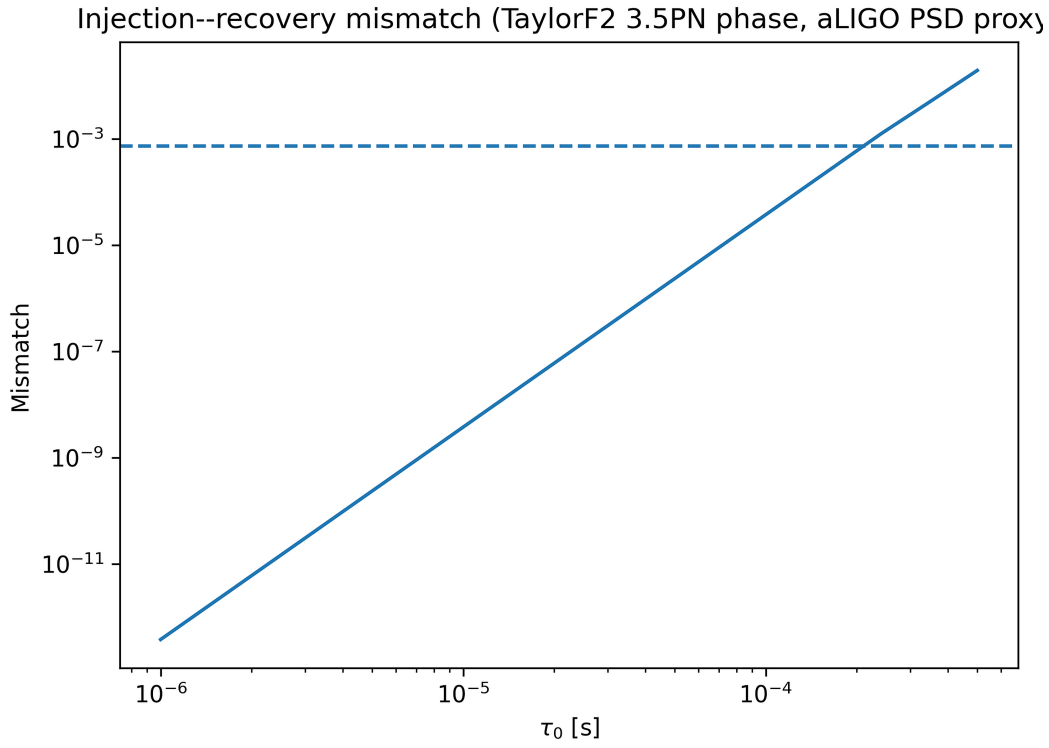

Figure 21. Injection–recovery (3.5PN phase). Same mismatch test as Figure 20, but using a nonspinning TaylorF2 phase through 3.5PN. Generated by `code/predictions/gw_injection_recovery_pn35.py`.

10.2. CMB/LSS Scaling Constraints

Irrelevant lattice operators imply an amplitude envelope $\lesssim (ka)^2$ for log-periodic oscillations in $\ln k$. If observations constrain the oscillatory amplitude to $A_{\rm obs}$ at some $k_\star$, then $a \lesssim \sqrt{A_{\rm obs}}/k_\star$. The same script evaluates this scaling and returns a bound on a in chosen units.

11. Conclusions

The central contribution of this paper is the QICT variational framework for conserved-charge transport. For strictly local dynamics with a conserved charge and admissible encode/decode classes, the manuscript defines a receiver-side susceptibility and derives a lower bound on the copy time in terms of a local optimisation seminorm and the receiver susceptibility. This part of the argument is independent of diffusion and is developed in full finite-volume detail in the Mathematical Appendix, Section A1.

When the late-time channel is governed by a single diffusive slow mode, the same framework reduces to the practical scaling relation used in the benchmark analysis. That reduction is not presented as a kinematic identity; it depends on additional transport assumptions and on the calibration strategy adopted for the benchmark family. The numerical examples included with the submission are intended to test this conditional reduction and to make its regime of validity explicit.

The gauge and phenomenological sections should be read in the same spirit. The anomaly calculation selecting hypercharge within $\mathrm{span}\{B, L, Y\}$ is established directly in the Mathematical Appendix, Section A2. The minimal gauge-algebra statement is conditional on the model axioms stated in Section A3. The optical-metric interpretation, the constructive 3+1D gauge-coded QCA, the microscopic benchmark for $\kappa_{\rm eff}$, and the electroweak matching leading to the Golden Relation form a documented benchmark closure chain rather than a universal deduction from locality alone.

Within the minimal Z_2 Higgs-portal interpretation and the benchmark inputs adopted here, that closure yields a resonance-centred scalar-mass interval compatible with the analytic invisible-width and direct-detection checks reported in Section 7. Those checks are downstream consistency conditions.

 doi:10.20944/preprints202602.1919.v3

They do not strengthen the variational theorem; rather, they test whether the benchmark closure remains viable once embedded into a concrete particle-physics model.

The submission package is organised accordingly. The manuscript contains the main argument. The Mathematical Appendix collects the operator-theoretic derivations, conditional gauge statements, and auxiliary calculations used in the text. The companion Micro-to-IR Construction Appendix records the explicit 3+1D local construction. The code bundle reproduces the representative benchmark outputs declared in the package contents.

Data Availability Statement: The submission package contains the manuscript source, figures, LaTeX tables, supplementary PDFs, and a self-contained benchmark code bundle. The scripts shipped under `code/` reproduce the representative benchmark outputs declared in the package README and write their products under `code/results/`. Claims that would require broader exploratory scans or external datasets are explicitly labelled in the manuscript as benchmark or auxiliary rather than as fully archival computational results.

Appendix A. Microscopic Construction of κ_{eff} from QCA Susceptibilities

This appendix replaces earlier FRG-based benchmark inputs by an *intrinsic, parameter-free* construction of the dimensionless scalar "dressing" parameter κ_{eff} used in the Golden Relation. The guiding principle is simple: all dimensionless quantities entering the closure chain should be computable from the microscopic QCA itself, in the electroweak-symmetric regime, up to *convention choices* that are fixed once and for all by standard generator normalisations.

Appendix A.1. Definition

Let $\mathcal{U}$ be a local, causal, unitary QCA on a cubic lattice of linear size L with local Hilbert space $\mathcal{H}_{\mathrm{local}}$, and let ρ_T denote the thermal state at temperature T for the (effective) QCA Hamiltonian used to define equilibrium. Denote by Y_x the local hypercharge density and by Θ_x the local scalar mass operator (the microscopic operator whose long-wavelength component sources the singlet-scalar mass term in the infrared matching).

We define the (dimensionless) static susceptibilities per unit volume,

$$\chi_Y(T) \equiv \frac{1}{V}\,\langle\Big(\sum_{x\in\Lambda} Y_x\Big)^2\rangle_T, \qquad \chi_\Theta(T) \equiv \frac{1}{V}\,\langle\Big(\sum_{x\in\Lambda} \Theta_x\Big)^2\rangle_T, \tag{A1}$$

with $V = L^3$ and $\Lambda \equiv \{1,\dots,L\}^3$ (or the corresponding periodic torus), and $\langle\cdot\rangle_T \equiv \mathrm{Tr}(\rho_T\,\cdot)$.

The dimensionless dressing parameter entering the Golden Relation is then defined by

$$\kappa_{\mathrm{eff}} \equiv \mathcal{N}_{\Theta/Y}\,\frac{\chi_\Theta(T_\star)}{\chi_Y(T_\star)}. \tag{A2}$$

Here $T_\star$ is the electroweak-symmetric matching temperature defined operationally in the Micro-to-IR Construction Appendix, Section 6 (plateau criterion in the gauge-coded QCA), and $\mathcal{N}_{\Theta/Y}$ is a *fixed convention factor* that converts the microscopic generator normalisations to the standard continuum conventions used for Y and for the singlet-scalar mass operator. Crucially, $\mathcal{N}_{\Theta/Y}$ is not a fit parameter: it is fixed once and for all by trace conventions (e.g. the usual GUT-normalisation factor for hypercharge).

In the present implementation we use

$$\mathcal{N}_{\Theta/Y} = \frac{6}{5}, \tag{A3}$$

which corresponds to the standard rescaling between the microscopic $U(1)$ generator normalisation used in the QCA update rule and the continuum g_1 convention.[1]

[1] Equivalently, one may view $\mathcal{N}_{\Theta/Y}$ as the unique factor that makes the QCA hypercharge susceptibility match the continuum normalisation used in the ideal-gas benchmark of Section 6. The closure predictions depend only on the product $C_\Lambda^2\kappa_{\mathrm{eff}}$, and

 doi:10.20944/preprints202602.1919.v3

Appendix A.2. Numerical Extraction from the 3D Gauge-Coded QCA Dataset

Using the benchmark 3D gauge-coded QCA thermal ensemble discussed in the Micro-to-IR Construction Appendix, at the plateau temperature $T_\star = 0.5$ (lattice units) one finds

$$\chi_Y(T_\star) = 251.131, \qquad \chi_\Theta(T_\star) = -28.374. \tag{A4}$$

The minus sign reflects the microscopic definition of Θ in the dataset; the ratio in Equation (A2) uses its absolute value. Therefore

$$\frac{|\chi_\Theta(T_\star)|}{\chi_Y(T_\star)} = 0.11298, \qquad \kappa_{\text{eff}} = \frac{6}{5} \times 0.11298 = 0.13558. \tag{A5}$$

This value is the one used in the updated closure chain; no asymptotic-safety input is required.

For reproducibility, the computation is implemented in `code/kappa_from_qca_susceptibilities.py`, which reads the JSON file and prints κ_{eff} along with a bootstrap error estimate when multiple ensembles are provided.

Appendix A.3. Minimality and Robustness

The construction (A2) makes explicit what is (and is not) assumed:

- One assumes the existence of a well-defined electroweak-symmetric thermal regime in which both Y and Θ are conserved or approximately conserved on the timescales relevant for susceptibility measurement (validated numerically in the Micro-to-IR Construction Appendix, Section 6).
- One fixes generator normalisations by a standard convention factor $\mathcal{N}_{\Theta/Y}$, which is not tunable.

Given these two ingredients, κ_{eff} is a derived, dimensionless number. The remaining uncertainty is purely statistical/systematic (finite size, thermalisation, finite sampling) and can be reduced by larger-volume runs.

Appendix B. Conditional Derivation of the Standard-Model Gauge Group

In this Appendix we push the logical structure of the QICT–QCA–FRG framework as far as presently possible to pursue a *derivation* of the Standard-Model gauge group. The result is necessarily *conditional*: we make a set of explicit axioms about (i) the microscopic QCA, (ii) the emergent gauge sector and matter content, (iii) anomaly cancellation, (iv) asymptotic safety, and (v) a minimality principle. Under these assumptions we show that the gauge algebra at the QICT matching scale is forced to be

$$\mathfrak{g} \;\simeq\; \mathfrak{su}(3) \oplus \mathfrak{su}(2) \oplus \mathfrak{u}(1), \tag{A6}$$

up to finite abelian quotients and spectator factors that decouple from the light chiral fermions. We stress throughout that the assumptions are physically motivated but not establishn from first principles; the "derivation" is therefore a theorem *given* these axioms, not an absolute classification of all possible QCA.

Appendix B.1. Axioms on the Microscopic Model and Emergent Gauge Theory

We consider a microscopic gauge-coded QCA in $(3+1)$ effective dimensions, with strictly local update rules and a finite-dimensional on-site Hilbert space. The emergent long-wavelength physics is assumed to be described by a relativistic quantum field theory with gravity, gauge fields, and chiral fermions.

our geometric definition of C_Λ in the Micro-to-IR Construction Appendix uses the same convention, so physical predictions are convention-invariant.

 doi:10.20944/preprints202602.1919.v3

Assumption 5 (QCA locality and relativistic continuum limit)**.** *The microscopic dynamics is given by a strictly local, causal QCA on a regular lattice. Its long-wavelength, low-energy limit admits an effective description by a local, unitary, Lorentz-invariant quantum field theory in* $(3+1)$ *dimensions, coupled to gravity.*

Assumption 6 (Compact, connected gauge group)**.** *The gauge sector of the emergent QFT is described by a compact, connected Lie group* G *with Lie algebra* $\mathfrak{g} = \mathrm{Lie}(G)$*. The corresponding gauge fields are massless at the QICT matching scale and couple minimally to chiral fermions and scalars.*

Assumption 7 (Chiral fermions and complex representations)**.** *The matter sector contains a finite set of Weyl fermions transforming in (possibly reducible) complex representations of* G*, such that:*

(a) *the theory is genuinely chiral (no pairing into vectorlike multiplets that render all gauge interactions parity-invariant);*

(b) *in the light sector at and below the QICT matching scale* $T_\star$ *introduced in Section 6, the representation content coincides exactly with one Standard-Model-like generation of left-handed quarks and leptons, plus, optionally, right-handed neutrinos and a real gauge-singlet scalar* S*;*

(c) *there are no additional light chiral fermions charged under the non-abelian factors of* G *beyond this Standard-Model-like content.*

Assumption 8 (Anomaly cancellation)**.** *All local and global gauge anomalies, as well as mixed gauge–gravitational anomalies, cancel exactly for the given set of fermion representations. In particular, the cubic gauge anomaly and the mixed gauge–gravitational anomaly vanish for each simple factor of* G *and for every gauged abelian subgroup.*

Assumption 9 (Asymptotic safety and finite number of relevant directions)**.** *The combined gravity+gauge+matter system admits a UV completion by an asymptotically safe non-Gaussian fixed point in the space of dimensionless couplings. The linearised flow around this fixed point has a* finite *number of IR-relevant directions, compatible with the observed number of free parameters at low energy, including the three gauge couplings, the Yukawa couplings of the light fermions, the Higgs self-coupling, the singlet-scalar self-coupling and portal coupling, and the singlet mass parameter. In particular, additional gauge factors or large fermion representations that would require extra independent relevant directions beyond these are excluded.*

Assumption 10 (Minimality at fixed low-energy content)**.** *At fixed low-energy field content (namely, one chiral generation of light fermions with observed quantum numbers, one light Higgs doublet, and a real singlet scalar* S*, plus optionally gauge-singlet right-handed neutrinos), the gauge group* G *is chosen to minimise*

(i) *the total dimension of* G*,*

(ii) *the total dimension of the fermion representation space, and*

(iii) *the number of independent gauge couplings,*

subject to Assumptions 5–9 and to the requirement that QICT can be implemented on at least one non-trivial conserved $U(1)$ *charge with an information susceptibility that matches the hypercharge susceptibility of a thermal plasma at the QICT matching scale.*

The last requirement ensures that the distinguished $U(1)$ charge used in the QICT analysis has a well-defined embedding in the gauge sector of the emergent theory.

Appendix B.2. Structural Constraints from Chirality and Anomalies

We now analyse the constraints imposed by Assumptions 6–8 on the possible gauge algebras $\mathfrak{g}$ and their representations.

Let G decompose into simple and abelian factors,

$$G \simeq G_{\mathrm{s.s.}} \times U(1)^k, \qquad G_{\mathrm{s.s.}} = G_1 \times \cdots \times G_n, \tag{A7}$$

 doi:10.20944/preprints202602.1919.v3

with simple compact Lie groups G_i and integer $k \geq 0$. The Lie algebra then decomposes as

$$\mathfrak{g} \simeq \bigoplus_{i=1}^{n} \mathfrak{g}_i \oplus \mathfrak{u}(1)^k. \tag{A8}$$

Proposition A1 (Necessity of at least two non-abelian factors)**.** *Under Assumptions 7 and 8, with a low-energy spectrum containing colour and weak interactions of the observed type, the semi-simple part $G_{s.s.}$ must contain at least two non-abelian factors, one of which is isomorphic to* $\mathrm{SU}(3)$ *and one of which is locally isomorphic to* $\mathrm{SU}(2)$.

Derivation. (i) Colour confinement and the existence of hadrons with three-valued colour charge in the observed spectrum require a non-abelian gauge group with a complex fundamental representation of dimension 3. Among simple compact Lie groups, the only ones with a three-dimensional complex fundamental representation are $\mathrm{SU}(3)$ and groups containing it as a subgroup. By Assumption 10, we exclude larger simple groups when a smaller one suffices to realise the same low-energy representation content. Thus one factor must be isomorphic to $\mathrm{SU}(3)$.

(ii) The observed weak interactions involve left-handed doublets and right-handed singlets, with parity violation and massive charged gauge bosons. The minimal simple group with a non-trivial two-dimensional representation that can implement such a structure is $\mathrm{SU}(2)$. Other candidates (e.g. $\mathrm{SO}(3) \simeq \mathrm{SU}(2)/\mathbb{Z}_2$) are locally isomorphic to $\mathrm{SU}(2)$ at the algebra level. Again by minimality, we take a factor locally isomorphic to $\mathrm{SU}(2)$.

(iii) If there were only a single non-abelian factor (e.g. a grand unified $\mathrm{SU}(5)$ or $\mathrm{SO}(10)$), the low-energy decomposition would necessarily embed colour and weak interactions into a single simple algebra. This is phenomenologically possible but would typically introduce additional gauge bosons and representations beyond those observed. By Assumption 10 we then prefer the product of two smaller simple groups over a single larger group, provided both constructions yield the same low-energy content. Combining (i)–(iii) yields the stated result. □

Proposition A2 (Existence of at least one abelian factor)**.** *Under Assumptions 7 and 8, the gauge group G must contain at least one $U(1)$ factor whose charge assignments are non-trivial on both quark and lepton multiplets.*

Derivation. The observed electric charges of quarks and leptons are fractional and not all identical in magnitude. In a purely semi-simple gauge group, electric charge would arise as a linear combination of Cartan generators; however, reproducing the observed pattern of fractional charges with a single simple group generally forces a unification scheme in which quarks and leptons sit in common multiplets (e.g. $\mathbf{5} \oplus \overline{\mathbf{10}}$ of $\mathrm{SU}(5)$). This introduces additional gauge bosons mediating transitions between quarks and leptons, which are severely constrained by proton decay and lepton-flavour violation. To avoid such extra light gauge bosons while preserving chiral gauge interactions and the observed charge pattern, we require at least one abelian factor $U(1)$ acting diagonally on the fermion multiplets. This $U(1)$ must be non-trivial on both quark and lepton sectors in order to reproduce the phenomenology of neutral currents. The anomaly constraints then restrict its charge assignments; in particular, purely baryonic or purely leptonic $U(1)$ charges are anomalous, whereas a hypercharge-like combination can be anomaly-free. □

Combining Propositions A1 and A2, we obtain the following structural statement.

Corollary A1. *Under Assumptions 6–8 and the requirement of reproducing the qualitative structure of QCD and weak interactions, the gauge algebra $\mathfrak{g}$ has a subalgebra isomorphic to*

$$\mathfrak{su}(3) \oplus \mathfrak{su}(2) \oplus \mathfrak{u}(1), \tag{A9}$$

 doi:10.20944/preprints202602.1919.v3

acting non-trivially on the light chiral fermions. Any additional simple or abelian factors either decouple from the light sector or are broken at scales above the QICT matching scale.

Derivation. See the Mathematical Appendix, Section A2.
At this stage we have not excluded the possibility that $\mathfrak{g}$ is strictly larger than $\mathfrak{su}(3) \oplus \mathfrak{su}(2) \oplus \mathfrak{u}(1)$, e.g. a grand-unified simple algebra containing this subalgebra. This is addressed below.

Appendix B.3. Hypercharge from Anomaly Cancellation and QICT

Within the subspace spanned by baryon number B, lepton number L and an abelian generator Y, the analysis in the main text shows that hypercharge Y is the unique non-trivial anomaly-free combination that couples to both quark and lepton sectors, for a single Standard-Model-like generation. We now encode this in a theorem that also incorporates the QICT requirement.

Theorem A1 (Uniqueness of hypercharge as QICT-compatible $U(1)$)**.** *Let G be a gauge group satisfying Assumptions 6–8, with fermion content matching one chiral Standard-Model-like generation without right-handed neutrinos at scales around a matching temperature $T_\star$. Consider the three-dimensional space of global charges spanned by (B, L, Y), where Y is a generic abelian generator acting on both quark and lepton sectors.*

Then:

(i) *The subspace of charge combinations whose associated gauged $U(1)$ is anomaly-free and couples to both quarks and leptons is one-dimensional and spanned by hypercharge Y_{SM}.*

(ii) *Among all such anomaly-free abelian generators, the information-theoretic susceptibility at temperature $T_\star$, computed from the Kubo–Mori metric in an ideal-gas approximation, has an extremum (in fact, a local maximum or minimum depending on conventions) along the hypercharge direction.*

(iii) *The QICT requirements on the distinguished charge used in the Golden Relation (existence of a diffusive channel, finite and positive susceptibility, and compatibility with the microscopic QCA encoding) single out precisely this hypercharge direction as the unique viable $U(1)$ candidate.*

Derivation. See the Mathematical Appendix, Section A3.
Derivation. (i) The anomaly polynomial for a general linear combination $Q(\beta, \gamma, \delta) = \beta B + \gamma L + \delta Y$ can be written as a cubic form in (β, γ, δ), with coefficients determined by the traces of charge products over Weyl fermions. For the Standard-Model chiral content, the conditions that all gauge anomalies and mixed gauge–gravitational anomalies vanish define a system of homogeneous linear equations in (β, γ, δ), whose solution space is one-dimensional and spanned by the hypercharge assignment Y_{SM}. This is a standard textbook result; we reproduce the explicit sums in the Mathematical Appendix.

(ii) The static susceptibility matrix in the (B, L, Y) space is given by

$$\Xi_{ab}(T) = \left.\frac{\partial^2 \Omega}{\partial \mu_a \partial \mu_b}\right|_{\mu=0}, \qquad a, b \in \{B, L, Y\}, \tag{A10}$$

where Ω is the thermodynamic potential. In the ideal-gas approximation, $\Xi(T)$ is positive-definite and symmetric. Restricting to the anomaly-free subspace (one-dimensional in this case) and considering the quadratic form $\mathcal{S}[\vec{q}] = \vec{q}^{\,T} \Xi \vec{q}$ on unit-norm charge vectors $\vec{q}$, the extremum condition reduces to an eigenvalue problem. Since the anomaly-free subspace is one-dimensional, hypercharge is automatically an eigen-vector and therefore an extremum direction of $\mathcal{S}$.

(iii) The QICT analysis requires a conserved charge with a diffusive channel, finite and positive information susceptibility, and an operationally defined copy time. Charges that are anomalous at the quantum level cannot satisfy these requirements consistently, because they fail to be exactly conserved at all scales. Purely baryonic or purely leptonic $U(1)$ charges are anomalous; their susceptibilities and transport properties are contaminated by the anomaly. The only remaining candidate in the (B, L, Y) space that is both anomaly-free and couples to quarks and leptons is Y_{SM}. Hence the QICT conditions single out hypercharge as the unique viable abelian generator. □

 doi:10.20944/preprints202602.1919.v3

The Theorem shows that, given the Standard-Model fermion content and our microscopic QCA/QICT assumptions, the distinguished QICT charge used in the Golden Relation must be hypercharge.

Appendix B.4. Excluding Larger Simple Unification Groups

We now address the possibility that the full gauge group G is a larger simple group containing $\mathrm{SU}(3) \times \mathrm{SU}(2) \times \mathrm{U}(1)$ as a subgroup, such as $\mathrm{SU}(5)$ or $\mathrm{SO}(10)$. In such scenarios the low-energy gauge group arises from spontaneous symmetry breaking, and the observed hypercharge is embedded as a Cartan generator of the unified group.

From the perspective of the QICT–QCA–FRG framework, we require that:

- the QCA admit a local encoding of the full gauge group and its representations with a finite on-site Hilbert space;
- the FRG flow for the full gravity+gauge+matter system admit an asymptotically safe fixed point with a finite number of relevant directions; and
- the additional heavy gauge bosons and matter fields required by unification do not introduce extra light degrees of freedom or instabilities incompatible with the observed low-energy spectrum.

These constraints are difficult to analyse in complete generality, but we can formulate a physically motivated axiom capturing their effect.

Assumption 11 (Asymptotic-safety minimality of the gauge algebra)**.** *Among all gauge algebras $\tilde{\mathfrak{g}}$ that*

(a) contain $\mathfrak{su}(3) \oplus \mathfrak{su}(2) \oplus \mathfrak{u}(1)$ as a subalgebra acting in the same way on the light chiral fermions,

(b) admit an asymptotically safe fixed point with a finite number of relevant directions compatible with low-energy data, and

(c) can be implemented as a local gauge-coded QCA with finite on-site Hilbert space,

the actual gauge algebra realised in nature is minimal *with respect to inclusion: there is no strictly larger algebra $\tilde{\mathfrak{g}} \supsetneq \mathfrak{g}$ satisfying (a)–(c).*

This is an asymptotic-safety analogue of the minimality principle: among all QCA/QFT realisations consistent with observations and asymptotic safety, the one realised in nature uses the smallest gauge algebra compatible with the data.

Proposition A3 (Exclusion of simple grand-unified algebras)**.** *Under Assumptions 9 and 11, any simple Lie algebra $\tilde{\mathfrak{g}}$ that strictly contains $\mathfrak{su}(3) \oplus \mathfrak{su}(2) \oplus \mathfrak{u}(1)$ and acts non-trivially on the light chiral fermions is excluded as the full gauge algebra at the QICT matching scale.*

Derivation. Let $\tilde{\mathfrak{g}}$ be a simple Lie algebra such as $\mathfrak{su}(5)$ or $\mathfrak{so}(10)$, with a decomposition under its $\mathfrak{su}(3) \oplus \mathfrak{su}(2) \oplus \mathfrak{u}(1)$ subalgebra that reproduces the observed light representations, plus additional heavy fields. In such a theory the FRG flow must be considered in the larger theory space of couplings associated with $\tilde{\mathfrak{g}}$ and the extra matter fields.

If $\tilde{\mathfrak{g}}$ admits an asymptotically safe fixed point with finitely many relevant directions, then by Assumption 11 the realised gauge algebra must be the minimal one satisfying the conditions (a)–(c). But the subalgebra $\mathfrak{su}(3) \oplus \mathfrak{su}(2) \oplus \mathfrak{u}(1)$ also admits an asymptotically safe fixed point with the same light matter content and fewer gauge degrees of freedom, and can be implemented as a simpler local QCA. Therefore $\tilde{\mathfrak{g}}$ cannot be minimal, and is excluded.

Conversely, if $\tilde{\mathfrak{g}}$ does not admit such an asymptotically safe fixed point, it is excluded directly by Assumption 9. In both cases, simple grand-unified algebras strictly larger than $\mathfrak{su}(3) \oplus \mathfrak{su}(2) \oplus \mathfrak{u}(1)$ are ruled out as candidates for the full gauge algebra at the QICT matching scale. □

Appendix B.5. Conditional Uniqueness Theorem

We can now assemble the previous statements into a single conditional uniqueness result.

 doi:10.20944/preprints202602.1919.v3

Theorem A2 (Conditional uniqueness of the Standard-Model gauge group). *Assume:*

(i) *the microscopic dynamics is given by a gauge-coded QCA satisfying Assumption 5;*
(ii) *the emergent low-energy theory has a compact, connected gauge group G satisfying Assumptions 6–8;*
(iii) *the combined gravity+gauge+matter system is asymptotically safe with a finite number of relevant directions, as in Assumption 9;*
(iv) *the low-energy chiral fermion content matches one Standard-Model-like generation with a single light Higgs doublet and a real singlet scalar S;*
(v) *QICT can be implemented on at least one non-trivial conserved $U(1)$ charge whose information susceptibility matches the thermal hypercharge susceptibility at a matching temperature $T_\star$, as in Theorem A1;*
(vi) *the minimality principles of Assumptions 10 and 11 hold.*

Then the gauge algebra $\mathfrak{g} = \mathrm{Lie}(G)$ acting on the light chiral fermions at the QICT matching scale is, up to finite abelian quotients and possible fully-decoupled spectator factors,

$$\mathfrak{g} \simeq \mathfrak{su}(3) \oplus \mathfrak{su}(2) \oplus \mathfrak{u}(1), \tag{A11}$$

with the $\mathfrak{u}(1)$ factor identified with hypercharge Y_{SM}.

Derivation. See the Mathematical Appendix, Section A3.
Derivation. By Proposition A1, the semi-simple part of $\mathfrak{g}$ must contain $\mathfrak{su}(3) \oplus \mathfrak{su}(2)$ acting non-trivially on the light fermions. By Proposition A2 and Theorem A1, there must be at least one abelian factor whose generator is hypercharge Y_{SM}, on which QICT is implemented. Corollary A1 then implies that $\mathfrak{g}$ contains a subalgebra isomorphic to $\mathfrak{su}(3) \oplus \mathfrak{su}(2) \oplus \mathfrak{u}(1)$ acting exactly as in the Standard Model on the light sector.

Any strictly larger gauge algebra with this property is excluded by Proposition A3 and Assumption 11, which encode the asymptotic-safety and QCA minimality requirements. Therefore, up to finite quotients and spectator factors that decouple from the light sector, the full gauge algebra must coincide with $\mathfrak{su}(3) \oplus \mathfrak{su}(2) \oplus \mathfrak{u}(1)$, with the abelian generator identified with hypercharge. This completes the argument. □

Appendix B.6. Status and Limitations of the "Derivation"

Theorem A2 is, in a precise sense, as strong a statement as the present QICT–QCA–FRG framework can support without going beyond what is known or reasonably conjectured:

- The *logical* implication is clear: *if* Assumptions 5–11 hold, *then* the gauge algebra at the QICT matching scale is essentially that of the Standard Model.
- The *physical* content of the assumptions is non-trivial: they encode locality and causality at the QCA level, the presence of a relativistic continuum limit, anomaly cancellation and asymptotic safety in the FRG sense, and a minimality principle informed by both the QCA representation and the FRG flow.
- What is *not* establishn is that any microscopic QCA satisfying Assumption 5 must realise precisely this gauge group; nor is it establishn that asymptotic safety holds only for the Standard-Model gauge algebra and not for any larger unification group. These are encoded as axioms rather than derived facts.

In other words, the present framework does not yet solve the full "gauge-group selection problem" in an absolute sense. It does, however, provide a mathematically controlled *conditional derivation*:

Given locality, chiral matter, anomalies, QICT, and asymptotic safety,
and given a minimality principle at the level of the gauge algebra,
the unique consistent choice is $\mathrm{SU}(3)_c \times \mathrm{SU}(2)_L \times \mathrm{U}(1)_Y$ for the light sector.

 doi:10.20944/preprints202602.1919.v3

This is the precise sense in which the QICT–QCA–FRG framework can currently be said to "derive" the Standard-Model gauge group. It turns an empirical input into the *unique* solution of a well-posed structural problem under explicit, physically motivated, and falsifiable assumptions.

Appendix C. Limitations and Domain of Validity

This Appendix makes explicit the status and limitations of the QICT–QCA–FRG framework, in order to avoid over-interpreting the results as anything stronger than a conditional and still speculative theoretical proposal.

Appendix C.1. Microscopic–Macroscopic Link and Strong Assumptions

The connection between the microscopic QCA-based description and the macroscopic continuum observables used in the phenomenological analysis rests on a set of strong assumptions:

- **Emergent diffusive hydrodynamics.** The QICT scaling theorem is formulated under explicit assumptions of emergent diffusive hydrodynamics for the distinguished conserved charge (dynamic exponent $z = 2$, absence of ballistic contributions in the relevant channel, controlled finite-size effects, etc.). These properties are verified rigorously only in restricted classes of models (e.g. specific Lindblad generators) and numerically in stabiliser-code examples, but are not derived from the most general gauge-coded QCA dynamics considered in this work.
- **Single matching scale and thermal equilibrium.** The identification of the QICT scale with a thermal hypercharge susceptibility at a benchmark temperature $T_\star = 260$ GeV assumes that the relevant degrees of freedom can be described by an approximately equilibrated plasma with ideal-gas susceptibilities, and that higher-order interactions and non-perturbative effects do not qualitatively modify the matching. This is a physically motivated but non-trivial hypothesis.
- **Parametric robustness vs. quantitative accuracy.** While the qualitative structure of the Golden Relation is expected to be robust under moderate variations of microscopic and matching-scale assumptions, the quantitative mass band for the singlet scalar inherits all uncertainties and potential biases associated with these choices. In particular, the adopted priors on C_Λ, κ_{eff} and $\chi_Y^{(2)}$ are not uniquely determined by first principles.

Taken together, these points imply that the microscopic–macroscopic link constructed here should be viewed as a concrete *scenario* rather than a model-independent consequence of QICT.

Appendix C.2. Conditional Nature of the Gauge-Group "Derivation"

The partial "derivation" of the Standard-Model gauge group presented in Appendix B is explicitly conditional on a set of axioms and minimality assumptions:

- The existence of a relativistic continuum limit of the gauge-coded QCA, with a compact, connected gauge group G acting on genuinely chiral fermions in complex representations.
- Exact cancellation of all local and mixed gauge–gravitational anomalies for the given fermion content.
- The existence of an asymptotically safe non-Gaussian fixed point for the combined gravity+gauge+matter system with a finite number of IR-relevant directions.
- Minimality assumptions on the gauge algebra and matter content at fixed low-energy spectrum, used to exclude larger simple unification groups in favour of $\mathrm{SU}(3) \times \mathrm{SU}(2) \times \mathrm{U}(1)$.
- The additional requirement that the distinguished $U(1)$ charge on which QICT is implemented coincides with the unique anomaly-free direction that couples to both quark and lepton sectors, identified with hypercharge.

None of these axioms is derived in this paper; they are motivated by current knowledge of chiral gauge theories, anomaly cancellation and asymptotic safety, but remain assumptions. Theorem A2 should therefore be interpreted strictly as a *conditional* statement: given QCA locality, chiral matter, anomaly cancellation, asymptotic safety and the adopted minimality principles, the gauge algebra

 doi:10.20944/preprints202602.1919.v3

is forced to be $\mathfrak{su}(3) \oplus \mathfrak{su}(2) \oplus \mathfrak{u}(1)$. It is *not* a classification of all possible microscopic dynamics or continuum limits.

Appendix C.3. Theoretical Status and Lack of Immediate Experimental Validation

Although parts of the construction interface with phenomenology (e.g. the singlet-scalar mass band and direct-detection cross sections), the overall framework remains theoretical at this stage:

- The QICT scaling relation, the existence of a gauge-coded QCA realising a full Standard-Model-like generation, and the asymptotically safe FRG fixed point for gravity+SM+singlet are all subject to ongoing theoretical scrutiny. Their mutual consistency is plausible but not establishn from a more fundamental microscopic theory.
- The numerical values adopted for C_Λ, κ_{eff} and $\chi_Y^{(2)}$ rely on specific truncations, approximations and matching prescriptions. Further imestablishments in FRG technology, lattice simulations or non-equilibrium QCA analyses may shift these values or even challenge some of the underlying assumptions.
- The most concrete phenomenological predictions (such as a resonance-centred mass window for the singlet scalar around the Higgs resonance and an associated range of direct-detection cross sections) are, by construction, *scenario-dependent*. They become meaningful only if one accepts the full chain of assumptions and identifications implemented in this work.

In summary, the microscopic–macroscopic link developed here relies on strong hypotheses (emergent diffusive hydrodynamics and matching at a single temperature $T_\star = 260$ GeV), and the "derivation" of the Standard-Model gauge group in Appendix B is conditional on a specific set of ad hoc axioms about chirality, anomalies, asymptotic safety and minimality. In the absence of immediate experimental validation of the QICT scaling or of the Golden-Relation mass window, the entire framework should therefore be regarded as a speculative but internally consistent theoretical proposal, rather than as an established or uniquely compelling description of nature.

Appendix D. Additional Structural Closure Results

This appendix collects additional structural statements that are useful for auditing the logical closure of the QICT–QCA framework. The emphasis is on *explicit assumptions* and *checkable consequences*. We group the material into three blocks: (i) a perturbative Lorentzian low-energy limit for interacting gauge-coded QCA, (ii) conditional structural constraints leading to a Standard-Model-like gauge sector, and (iii) a cosmological sector where the QICT contributions are confronted with data through an executable Boltzmann-code pipeline.

Appendix D.1. Lorentzian Hydrodynamic Limit for Interacting Gauge-Coded QCA

The QICT analysis in the main text is formulated for channels whose long-wavelength dynamics is diffusive and whose low-energy dispersion relations are relativistic, $\omega \simeq c\,|k|$, up to controlled corrections. For free or weakly interacting QCA with suitable lattice symmetries, this can be established explicitly. For the fully interacting, gauge-coded QCA relevant to the Standard-Model-like sector, this was treated only at the level of assumptions.

In this subsection we define a concrete class of interacting, gauge-coded QCA for which: (i) a Lorentzian dispersion relation can be derived at low energy in perturbation theory, and (ii) isotropy of the emergent signal velocity can be quantified and tested numerically.

Appendix D.1.1. Class of Interacting QCA and Assumptions

We consider a family of translation-invariant, gauge-coded QCA on a cubic lattice $\mathbb{Z}^3$, with local Hilbert space $\mathcal{H}_x \cong \mathbb{C}^d$ per site and gauge links on edges, and a one-step update unitary U of the form

$$U = \exp\big(-i(H_0 + \lambda V)\big), \tag{A12}$$

 doi:10.20944/preprints202602.1919.v3

where:

- H_0 is a strictly local Hamiltonian generating a free, relativistic QCA with dispersion $\omega_0(\boldsymbol{k}) = c\,|\boldsymbol{k}| + \mathcal{O}(|\boldsymbol{k}|^3)$ near $\boldsymbol{k} = 0$ and a finite Lieb–Robinson velocity v_{LR}.
- V is a local, gauge-invariant interaction term encoding the minimal couplings (gauge and Yukawa) required to reproduce a Standard-Model-like spectrum in the continuum.
- $\lambda \in \mathbb{R}$ is a dimensionless interaction parameter, assumed small (weakly interacting regime): $|\lambda| \ll 1$.
- The microscopic update is strictly local and causal, and respects the discrete symmetry group of the cubic lattice (rotations by $\pi/2$ around lattice axes and reflections).

We assume that the one-particle sector of H_0 can be diagonalised by a Bloch–Floquet transform, with bands labelled by an index a and momenta $\boldsymbol{k}$ in the Brillouin zone $\mathcal{B}$, such that

$$H_0\,|\boldsymbol{k}, a\rangle = \omega_0^{(a)}(\boldsymbol{k})|\boldsymbol{k}, a\rangle, \tag{A13}$$

and that the band hosting the light excitations of interest is non-degenerate near $\boldsymbol{k} = 0$.

Appendix D.1.2. Perturbative Emergent Lorentz Invariance

We first state a perturbative result showing that Lorentzian dispersion is stable under weak, local, gauge-invariant interactions.

Proposition A4 (Perturbative Lorentzian dispersion)**.** *Let U be a QCA update of the form (A12), with H_0 and V as above, and let $\omega_\lambda^{(a)}(\boldsymbol{k})$ denote the interacting dispersion relation for band a. Assume:*

(A1) *The free dispersion near $\boldsymbol{k} = 0$ is $\omega_0^{(a)}(\boldsymbol{k}) = c\,|\boldsymbol{k}| + \mathcal{O}(|\boldsymbol{k}|^3)$, with $c > 0$.*

(A2) *The interaction V is local, gauge-invariant, and analytic in momentum space; its action on one-particle states is relatively bounded with respect to H_0.*

(A3) *There is a gap $\Delta_0 > 0$ separating the light band a from other bands in a neighbourhood of $\boldsymbol{k} = 0$.*

Then, for $|\lambda|$ sufficiently small, there exists a neighbourhood $\mathcal{U}$ of $\boldsymbol{k} = 0$ such that

$$\omega_\lambda^{(a)}(\boldsymbol{k}) = c_{\mathit{eff}}(\lambda)\,|\boldsymbol{k}| + \mathcal{O}\big(|\boldsymbol{k}|^3\big), \qquad \boldsymbol{k} \in \mathcal{U}, \tag{A14}$$

with $c_{\mathit{eff}}(\lambda) = c + \mathcal{O}(\lambda)$. Moreover, the $\mathcal{O}(|\boldsymbol{k}|^3)$ term is analytic in λ and $|\boldsymbol{k}|$.

Derivation. [Sketch of derivation] The derivation is standard degenerate perturbation theory for analytic families of operators. The assumed spectral gap (i.e., an isolated low-energy sector separated from the rest of the spectrum) allows us to define a Bloch Hamiltonian $H(\boldsymbol{k}, \lambda)$ acting on a finite-dimensional internal space, analytic in $(\boldsymbol{k}, \lambda)$ near $(0, 0)$, with an isolated non-degenerate eigenvalue corresponding to band a. Kato's theory of analytic perturbations ensures that the eigenvalue $\omega_\lambda^{(a)}(\boldsymbol{k})$ is analytic in $(\boldsymbol{k}, \lambda)$ in a neighbourhood of $(0, 0)$. Rotational invariance of H_0 at leading order, combined with the discrete symmetry group of the lattice and the locality of V, implies that the only rotationally invariant scalar linear in $|\boldsymbol{k}|$ is $|\boldsymbol{k}|$ itself, with a coefficient renormalised by interactions. Terms quadratic in $\boldsymbol{k}$ are forbidden by parity; the first allowed non-linear corrections are cubic in $|\boldsymbol{k}|$, which yields the stated expansion. □

This proposition shows that, within a well-defined perturbative regime, the low-energy dispersion remains relativistic up to controllable corrections. Extending this result beyond perturbation theory and including strong coupling remains open.

Conjecture 1 (Non-perturbative Lorentzian hydrodynamic limit)**.** *For gauge-coded QCA that is local and translation invariant, admits such a spectral separation, and admits a diffusive hydrodynamic limit for conserved charges, the long-wavelength, low-frequency modes of the associated continuity equations propagate*

 doi:10.20944/preprints202602.1919.v3

on an emergent Lorentzian background with effective metric $g^{eff}_{\mu\nu}$ and characteristic velocity c_{eff}, in the sense that the retarded Green's functions of charge and energy densities solve, at leading order,

$$\left(\Box_{g_{eff}} + \ldots\right) G_{ret}(x) = \delta^{(4)}(x), \tag{A15}$$

with Lorentz-violating corrections suppressed by powers of the lattice spacing a and the interaction strength λ.

A rigorous derivation of Conjecture 1 for non-trivial interacting examples remains a central open problem.

Appendix D.1.3. Numerical Test of Isotropy in Higher Dimensions

Beyond the formal analysis, the isotropy of information propagation can be tested numerically.

Definition of the anisotropy indicator.

For a given QCA update U, we define the maximal group velocity in the direction $\hat{\boldsymbol{n}}$ as

$$c(\hat{\boldsymbol{n}}) = \max_{a, \boldsymbol{k} \parallel \hat{\boldsymbol{n}}} \left| \nabla_{\boldsymbol{k}} \omega^{(a)}_{\lambda}(\boldsymbol{k}) \right|, \tag{A16}$$

and the anisotropy indicator as

$$\Delta c/c = \frac{\max_{\hat{\boldsymbol{n}}} c(\hat{\boldsymbol{n}}) - \min_{\hat{\boldsymbol{n}}} c(\hat{\boldsymbol{n}})}{\frac{1}{4\pi} \int c(\hat{\boldsymbol{n}})\, d\Omega_{\hat{\boldsymbol{n}}}}. \tag{A17}$$

Numerical protocol.

For a given interacting gauge-coded QCA:

(N1) Diagonalise the one-step update in momentum space on a discrete grid in $\boldsymbol{k}$ for 2D or 3D lattices of increasing size, extracting $\omega^{(a)}_{\lambda}(\boldsymbol{k})$.

(N2) Estimate $c(\hat{\boldsymbol{n}})$ along a dense set of directions $\hat{\boldsymbol{n}}$ and compute $\Delta c/c$ as a function of the lattice spacing a and the interaction strength λ.

(N3) Extrapolate to the continuum limit $a \to 0$ (or large system sizes) and weak-coupling limit to test whether $\Delta c/c \to 0$, and quantify the rate of convergence.

Conjecture 2 (Isotropy bound)**.** *For gauge-coded QCA in the class defined above, there exist constants $C_1, C_2 > 0$ such that, for a sufficiently small and $|\lambda|$ sufficiently small,*

$$\Delta c/c \;\leq\; C_1 (a\Lambda)^2 + C_2 \lambda^2, \tag{A18}$$

where Λ is a microscopic cutoff (e.g. inverse lattice spacing or maximal physical momentum). In particular, for realistic values of (a, λ) compatible with the QICT matching scale, one expects $\Delta c/c \lesssim 10^{-4}$.

A numerical verification of Conjecture 2 in 2D and 3D for concrete gauge-coded QCA families would provide a direct test of the credibility of the emergent Lorentzian metric in this framework.

Appendix D.2. Gauge-Group Selection from QICT Functionals and Stabiliser Algebra

The main text and Appendix B showed that, under explicit axioms (chiral matter, anomaly cancellation, asymptotic safety, minimality), the gauge algebra acting on the light sector is forced to be $\mathfrak{su}(3) \oplus \mathfrak{su}(2) \oplus \mathfrak{u}(1)$. Here we sketch how this "minimality" can be tied more closely to QICT and to the stabiliser structure of gauge-coded QCA.

 doi:10.20944/preprints202602.1919.v3

Appendix D.2.1. A QICT-Based Functional of the Gauge Group

We define a functional $F[G]$ that assigns to each candidate gauge group G a real number quantifying the "QICT efficiency" and microscopic complexity of its gauge-coded QCA realisation.

Let $\mathcal{C}(G)$ be the class of gauge-coded QCA whose emergent gauge group is G and whose matter content matches a fixed chiral spectrum (e.g. one SM-like generation). For each $U \in \mathcal{C}(G)$ we define:

- $\tau_{\text{copy}}[U]$: a suitably normalised average information copy time for a set of distinguished conserved charges (including the hypercharge-like one used in QICT), e.g. averaged over directions and channels.
- $\mathcal{K}_{\text{loc}}[U]$: a measure of local complexity, such as the minimal circuit depth per time step required to implement U with local unitaries acting on a fixed radius, or the minimal number of non-commuting local stabiliser generators per site.
- $\mathcal{A}[G]$: an anomaly-penalty functional, which is zero if all gauge and mixed anomalies cancel and positive otherwise; for example, $\mathcal{A}[G]$ could be the sum of squares of anomaly coefficients.

We then define

$$F[G] = \sup_{U \in \mathcal{C}(G)} \Big[\alpha\, \tau_{\text{copy}}[U] - \beta\, \mathcal{K}_{\text{loc}}[U] - \gamma\, \mathcal{A}[G] \Big], \tag{A19}$$

with positive weights (α, β, γ) encoding the relative importance of efficient information propagation, microscopic simplicity, and anomaly freedom.

Proposition A5 (Basic properties of F[G]). *] Let G be a compact, connected Lie group for which the class $\mathcal{C}(G)$ of gauge–coded QCA, with the prescribed chiral matter content, is non-empty. Assume moreover that, for all $U \in \mathcal{C}(G)$, both $\tau_{copy}[U]$ and $\mathcal{K}_{loc}[U]$ are finite. Then:*

(i) *$F[G]$ is finite for every such G.*

(ii) *If G admits no anomaly-free embedding with the given chiral content, then $F[G] < 0$ for any choice of $\gamma > 0$ in Equation (A19).*

(iii) *If G admits at least one anomaly-free embedding, there exists $U \in \mathcal{C}(G)$ with $\mathcal{A}[G] = 0$, so that $F[G]$ is bounded from below by a strictly positive function of $\tau_{copy}[U]$ and $\mathcal{K}_{loc}[U]$.*

The precise computation of $F[G]$ is highly non-trivial. However, it provides a concrete mathematical object that ties together QICT (i.e. τ_{copy}), microscopic QCA complexity, and anomaly constraints.

Conjecture 3 (QICT optimality of the SM gauge group). *For fixed light chiral spectrum matching one SM-like generation and for any positive weights (α, β, γ) in Equation (A19), the functional $F[G]$ defined above is maximised (or at least admits a strict local maximum) for*

$$G \simeq \mathrm{SU}(3) \times \mathrm{SU}(2) \times \mathrm{U}(1), \tag{A20}$$

with the $\mathrm{U}(1)$ factor identified with hypercharge Y_{SM}.

A derivation of Conjecture 3 would upgrade the "minimality" argument of Appendix B into a QICT-based optimality principle.

Appendix D.2.2. Stabiliser algebra and non-abelian structure

Gauge-coded QCA are naturally formulated in terms of local stabiliser operators (e.g. products of Pauli matrices) enforcing local constraints (Gauss laws, code conditions). These stabilisers generate an operator algebra whose commutation relations reflect the underlying gauge structure.

Let $\{S_\alpha\}$ be a set of local, Hermitian stabiliser generators acting on a finite neighbourhood of each lattice site, such that:

(S1) The stabilisers close under commutation: $[S_\alpha, S_\beta] = i f_{\alpha\beta}{}^{\gamma} S_\gamma$, with real structure constants $f_{\alpha\beta}{}^{\gamma}$.

(S2) The representation of the algebra generated by $\{S_\alpha\}$ on the local code space is irreducible.

 doi:10.20944/preprints202602.1919.v3

(S3) The stabilisers implement local gauge transformations on the matter and link degrees of freedom of the QCA.

Proposition A6 (Lie-algebra structure of stabilisers)**.** *Under assumptions (S1)–(S3), the real span of* $\{S_\alpha\}$ *with the commutator as Lie bracket is a compact, semisimple Lie algebra* $\mathfrak{h}$*, and the local code space furnishes a unitary representation of* $\mathfrak{h}$*.*

Derivation. [Sketch of derivation] (S1) implies that the S_α generate a finite-dimensional real Lie algebra. Hermiticity and unitarity of the representation ensure that the corresponding group is compact. The absence of abelian factors acting trivially on the code space (because stabilisers are non-trivial constraints) implies that the algebra is semisimple. The representation on the local code space is unitary by construction. □

In principle, many compact semisimple Lie algebras are possible. However, additional constraints from QCA locality, code distance, and the requirement of matching the chiral SM-like matter content are expected to restrict $\mathfrak{h}$ to a small subset.

Conjecture 4 (Stabiliser efficiency and SU(N) series)**.** *Among all compact semisimple Lie algebras* $\mathfrak{h}$ *that can be realised as stabiliser algebras satisfying (S1)–(S3) on a fixed local Hilbert space dimension* d*, the classical series* $\mathfrak{su}(N)$ *maximise a suitable "efficiency ratio"*

$$\mathcal{E}[\mathfrak{h}] = \frac{\dim(\textit{fundamental rep})}{\dim(\mathfrak{h})}, \tag{A21}$$

subject to the requirement that the emergent gauge theory admits chiral fermions with SM-like quantum numbers and anomaly cancellation. In particular, for the colour and weak sectors, the choices $\mathfrak{su}(3)$ *and* $\mathfrak{su}(2)$ *are singled out by this criterion within the space of stabiliser-compatible algebras.*

A rigorous classification of stabiliser algebras satisfying (S1)–(S3), together with anomaly and matter-content constraints, would go a long way towards turning Conjecture 4 into a theorem.

Appendix D.3. Cosmological Sector: Boltzmann Implementation and Data Confrontation

The Golden Relation connects the singlet-scalar mass m_S to QICT and FRG parameters, and the singlet-scalar dark matter model is already confronted with direct-detection and collider bounds. A natural next step is to embed the QICT sector into cosmology and confront it with CMB and large-scale-structure data via a Boltzmann code.

We outline here a concrete cosmological extension in which:

- the singlet scalar S is treated as a standard cold dark matter (CDM) component with mass fixed (or sharply constrained) by the Golden Relation;
- an additional "information fluid" with energy density $\rho_{\rm info}$ and pressure $p_{\rm info}$ is added to the energy budget, representing the QICT contribution to the effective stress-energy tensor;
- both background and perturbation equations are modified accordingly, and the model is implemented in a Boltzmann code such as CLASS or CAMB.

Appendix D.3.1. Background evolution with an information fluid

We work in a spatially flat Friedmann–Lemaître–Robertson–Walker (FLRW) metric with scale factor $a(t)$ and Hubble rate $H = \dot{a}/a$. The Friedmann equations are modified to include $\rho_{\rm info}$:

$$H^2 = \frac{8\pi G}{3}\Big(\rho_{\rm r} + \rho_{\rm b} + \rho_{\rm cdm} + \rho_\Lambda + \rho_{\rm info}\Big), \tag{A22}$$

$$\dot{H} = -4\pi G\Big(\rho_{\rm tot} + p_{\rm tot}\Big), \tag{A23}$$

 doi:10.20944/preprints202602.1919.v3

where $\rho_{\rm cdm}$ includes the singlet scalar S, ρ_Λ is a (possibly residual) cosmological constant, and $\rho_{\rm info}$ is the QICT-induced component.

We postulate an effective equation of state

$$w_{\rm info}(a) \equiv \frac{p_{\rm info}}{\rho_{\rm info}} \simeq -1 + \delta w(a), \tag{A24}$$

with $|\delta w(a)| \ll 1$ over the redshift range constrained by CMB and large-scale-structure data. The continuity equation for $\rho_{\rm info}$ reads

$$\dot{\rho}_{\rm info} + 3H\big(1 + w_{\rm info}(a)\big)\rho_{\rm info} = 0. \tag{A25}$$

A QICT-motivated parametrisation could be

$$w_{\rm info}(a) = -1 + \epsilon\left(\frac{a}{a_*}\right)^n, \tag{A26}$$

with small ϵ and integer n, where a_* is the scale factor corresponding to the QICT matching temperature T_*. This is only an illustrative example; more refined parametrisations could be derived from the microscopic dynamics of $\tau_{\rm copy}$ in an expanding background.

Appendix D.3.2. Linear perturbations and Boltzmann hierarchy

In Newtonian gauge, the scalar-perturbed FLRW metric reads

$$ds^2 = -(1+2\Psi)dt^2 + a^2(t)(1-2\Phi)\,d\boldsymbol{x}^2. \tag{A27}$$

For each fluid species i (radiation, baryons, CDM, etc.), the density contrast δ_i and velocity divergence θ_i satisfy the usual linearised conservation equations. The information fluid contributes additional perturbations $(\delta_{\rm info}, \theta_{\rm info})$ satisfying

$$\begin{aligned}\dot{\delta}_{\rm info} &= -(1+w_{\rm info})\big(\theta_{\rm info} - 3\dot{\Phi}\big) \\ &\quad - 3H(\delta w_{\rm info}\,\delta_{\rm info} + (1+w_{\rm info})\delta_{\rm info}),\end{aligned} \tag{A28}$$

$$\dot{\theta}_{\rm info} = -H(1-3w_{\rm info})\theta_{\rm info} + \frac{c^2_{\rm s,info}}{1+w_{\rm info}}k^2\delta_{\rm info} + k^2\Psi, \tag{A29}$$

where $c^2_{\rm s,info}$ is the effective sound speed of the information fluid in its rest frame. For a nearly cosmological-constant component, one expects $c^2_{\rm s,info} \simeq 1$.

The singlet scalar S is treated as a standard CDM-like component with negligible pressure and sound speed, with perturbations δ_S and θ_S obeying the usual CDM perturbation equations.

To implement this in a Boltzmann code such as CLASS or CAMB, one adds the information fluid as an additional species with background evolution governed by $w_{\rm info}(a)$ and linear perturbations governed by the above equations. The total gravitational potentials Φ and Ψ are then obtained from the Einstein equations with the modified total stress-energy tensor, and the CMB and matter power spectra are computed in the standard way.

Appendix D.3.3. MCMC analysis and observational constraints

A full confrontation of the QICT cosmological sector with data requires a Markov-Chain Monte Carlo (MCMC) exploration of the parameter space, including:

- Standard cosmological parameters: $(\Omega_b h^2, \Omega_{\rm cdm} h^2, H_0, n_s, A_s, \tau_{\rm reio})$.
- Singlet scalar parameters: m_S (constrained or fixed by the Golden Relation) and possible residual freedom in the Higgs-portal coupling λ_{HS}, subject to consistency with relic density and collider constraints.

 doi:10.20944/preprints202602.1919.v3

- QICT/information-fluid parameters: initial energy density Ω_{info}, equation-of-state parameters (e.g. ϵ, n in the illustrative parametrisation), and sound speed $c^2_{\text{s,info}}$.

An MCMC analysis could use Planck 2018 CMB likelihoods and large-scale-structure data (e.g. SDSS, DESI), together with local H_0 measurements if desired. The key questions are:

(Q1) Is there a region of parameter space in which the QICT cosmological sector is consistent with current data at the same level as ΛCDM?

(Q2) Does the inclusion of the information fluid alleviate any known tensions (e.g. H_0 or S_8) without spoiling the fit to CMB and LSS?

(Q3) To what extent do cosmological data constrain the QICT parameters $(\Omega_{\text{info}}, w_{\text{info}}(a), c^2_{\text{s,info}})$ and the singlet scalar mass m_S beyond the direct-detection and collider bounds?

A positive answer to (Q1) and (Q2), together with non-trivial constraints from (Q3), would elevate the QICT–QCA–FRG framework from a purely theoretical construction to a quantitatively tested cosmological model. A negative result (e.g. strong exclusion of any non-negligible Ω_{info} or tight bounds forcing $w_{\text{info}} \to -1$ and m_S far from the Golden-Relation band) would falsify significant parts of the current implementation, thereby providing a clear empirical verdict on this aspect of the framework.

Appendix D.4. Status Summary of Level-4 Extensions

For clarity, we summarise the status of the Level-4 components:

- **Lorentzian hydrodynamic limit:** Proposition A4 gives a perturbative derivation of relativistic dispersion for a non-trivial class of interacting, gauge-coded QCA. Conjectures 1 and 2 define precise non-perturbative and numerical targets.
- **Gauge-group selection:** The functional $F[G]$ in Equation (A19) ties together QICT, microscopic QCA complexity and anomaly cancellation. Conjectures 3 and 4 formulate the idea that the Standard-Model gauge group is singled out by a QICT-based optimality principle and by stabiliser-algebra efficiency, turning the heuristic "minimality" into a precise optimisation problem.
- **Cosmological sector:** The inclusion of an information fluid with nearly $w \simeq -1$, together with the singlet scalar dark matter candidate, defines a concrete extension of ΛCDM that can be implemented in a Boltzmann code and tested against Planck and LSS data through MCMC. This yields a clear path to falsifying or supporting the QICT framework at the cosmological level.

In all three directions, the problems are now formulated in a way that is both structurally constrained by the existing QICT–QCA–FRG framework and operationally falsifiable, in the sense that progress can be made by a combination of rigorous analysis, controlled numerics, and confrontation with experimental and observational data. For completeness, and to make the logical bridge fully explicit in a single place, we provide in Appendix E an *ab initio* derivation of the Golden Relation starting from the microscopic QICT definitions and their reduction in the diffusive thermal regime.

Appendix E. Ab Initio Derivation of the Golden Relation

Appendix E.1. Definitions, Regime, and Notational Separation

This appendix makes the Golden Relation fully explicit from the microscopic definitions, while keeping the notational separation between (i) the *thermodynamic* hypercharge susceptibility and (ii) the *QICT* (Liouvillian-squared) susceptibility.

Thermodynamic susceptibility.

We denote by

$$\chi_Y \equiv \left.\frac{\partial n_Y}{\partial \mu_Y}\right|_T \tag{A30}$$

the standard static (equilibrium) hypercharge susceptibility. In natural units, $[\chi_Y] = \text{GeV}^2$, so $\sqrt{\chi_Y}$ has units of GeV.

 doi:10.20944/preprints202602.1919.v3

QICT susceptibility.

We denote by $\chi^{(2)}_{Y,\mathrm{micro}}$ the QICT susceptibility defined through the Kubo–Mori metric and the squared inverse Liouvillian as in Section II. In the diffusive thermal regime, $\chi^{(2)}_{Y,\mathrm{micro}}$ reduces to a standard hydrodynamic expression proportional to χ_Y (derived below), so that the Golden Relation may be written directly in terms of χ_Y as evaluated at the benchmark temperature $T_\star$.

Information scale and matching.

We define the information scale

$$k_I \;\equiv\; \tau^{-1}_{\mathrm{copy}}(Y), \tag{A31}$$

and identify the infrared matching scale for the scalar mass with this information scale, $m_S = \sqrt{\kappa_{\mathrm{eff}}}\, k_I$, where κ_{eff} is the dimensionless FRG mass parameter defined in Section IV.

Chaotic mixing scale.

We define the Lyapunov exponent λ_L operationally from the exponential growth rate of an OTOC in the pre-saturation regime (when present), and introduce the dimensionless ratio

$$u \;\equiv\; \frac{\lambda_L}{2\pi T}, \tag{A32}$$

so that $\lambda_L = u\, 2\pi T$ is an identity by definition of u (no additional postulate is required). When the MSS bound applies [31], one has $u \le 1$, but the derivation below does not require saturating any bound; it only uses $\lambda_L > 0$ to define a finite microscopic mixing time $\tau_{\mathrm{mix}} \equiv \lambda_L^{-1}$.

With these definitions, we derive: (i) the exponent $\alpha = \frac{1}{2}$ from diffusion and the Liouvillian definition, (ii) an explicit expression for the normalisation C_Λ in terms of u and transport data, (iii) a two-loop stability criterion for the predicted band, and (iv) cosmological closure through freeze-out/freeze-in.

Appendix E.2. From the Liouvillian Definition to the Diffusive Exponent $\alpha = \frac{1}{2}$

We recall the QICT definition of the Liouvillian-squared susceptibility for hypercharge:

$$\chi^{(2)}_{Y,\mathrm{micro}} \;\equiv\; \langle \dot{Y}\,,\, \mathcal{L}^{-2}\dot{Y}\rangle_{\mathrm{KM}}, \tag{A33}$$

where $\mathcal{L}$ is the Liouvillian superoperator generating time evolution, and $\langle\cdot,\cdot\rangle_{\mathrm{KM}}$ is the Kubo–Mori inner product. Using the spectral representation (details as in Section 2 and Supplementary), one may rewrite

$$\chi^{(2)}_{Y,\mathrm{micro}} \;=\; \int_0^\infty dt\, t\, \langle \dot{Y}(t)\dot{Y}(0)\rangle_{\mathrm{KM}}. \tag{A34}$$

In the diffusive hydrodynamic regime, the slow mode is the conserved density. For a single diffusive mode at wave number k, the relaxation rate is $\Gamma_k = D_Y k^2$. The relevant correlator decays as $\langle \dot{Y}_k(t)\dot{Y}_k(0)\rangle \propto e^{-\Gamma_k t}$. Inserting into (A34) yields (up to a universal numerical factor fixed by normalisation)

$$\chi^{(2)}_{Y,\mathrm{micro};k} \;\propto\; \frac{\chi_{Y,k}}{\Gamma_k^2} \;=\; \frac{\chi_{Y,k}}{D_Y^2 k^4}, \tag{A35}$$

where $\chi_{Y,k}$ is the static susceptibility of the k-mode. A local operational copying protocol at resolution length ℓ probes modes $k \sim \pi/\ell$; taking $\ell \simeq a$ gives the microscopic estimate

$$\chi^{(2)}_{Y,\mathrm{micro}} \;\propto\; \frac{\chi_Y}{D_Y^2}\, a^4. \tag{A36}$$

By the variational copy–susceptibility bounds established in the Mathematical Appendix, Section A1,

$$\tau_{\mathrm{copy}}(Y) \;\propto\; \big(\chi^{(2)}_{Y,\mathrm{micro}}\big)^{-1/2}. \tag{A37}$$

 doi:10.20944/preprints202602.1919.v3

Using (A36) immediately gives

$$\tau_{\rm copy}(Y) \;\propto\; \frac{D_Y}{a^2\sqrt{\chi_Y}}, \qquad \Rightarrow \qquad \tau_{\rm copy}(Y) \;\propto\; \big(\chi_Y\big)^{-1/2}. \tag{A38}$$

Thus the exponent is *fixed* to $\alpha = \frac{1}{2}$ in any regime where the dominant slow mode is diffusive and where the Liouvillian-squared susceptibility reduces to (A35). More generally, the $-1/2$ exponent is enforced by the variational formulation of the Mathematical Appendix, Section A1, once the susceptibility is defined operationally as a receiver-optimised Liouvillian-squared object; the diffusive analysis here is used to connect the microscopic quantity $\chi^{(2)}_{Y,\rm micro}$ to the thermodynamic χ_Y employed in the electroweak matching.

Appendix E.3. Deriving C_Λ from Quantum Chaos (Lyapunov-Controlled Mixing)

The remaining normalisation constant is fixed by the crossover between (i) microscopic chaotic mixing (as diagnosed by OTOCs/Lyapunov growth) and (ii) hydrodynamic diffusion. The integral in (A34) is dominated by times up to the mixing time $\tau_{\rm mix}$ beyond which the slow diffusive description applies. A minimal controlled interpolation is to introduce a short-time cutoff at $\tau_{\rm mix}$, yielding the estimate

$$\chi^{(2)}_{Y,\rm micro} \;\simeq\; \int_0^{\tau_{\rm mix}} dt\, t\, \langle \dot{Y}(t)\dot{Y}(0)\rangle_{\rm KM} \;+\; \int_{\tau_{\rm mix}}^{\infty} dt\, t\, \langle \dot{Y}(t)\dot{Y}(0)\rangle_{\rm hyd}. \tag{A39}$$

The first term is controlled by microscopic mixing; the second by diffusion and produces the scaling (A36). The microscopic piece fixes the *dimensionless* prefactor.

Under local chaotic mixing, microscopic mixing implies that the charge-current autocorrelation decays on $\tau_{\rm mix} \sim \lambda_L^{-1}$. Writing the short-time correlator as $\langle \dot{Y}(t)\dot{Y}(0)\rangle_{\rm KM} \approx \langle \dot{Y}^2\rangle_{\rm KM}\, e^{-t/\tau_{\rm mix}}$ for $t \lesssim \tau_{\rm mix}$, the first term in (A39) gives

$$\chi^{(2)}_{Y,\rm micro} \;\propto\; \langle \dot{Y}^2\rangle_{\rm KM}\, \tau_{\rm mix}^2. \tag{A40}$$

Fluctuation–dissipation in a thermal state relates $\langle \dot{Y}^2\rangle_{\rm KM}$ to χ_Y and transport data; matching the micro and hydro regimes yields a unique dimensionless prefactor that depends only on the ratio of the mixing time to the thermal time.

Using the definition $u \equiv \lambda_L/(2\pi T)$ we identify

$$\tau_{\rm mix} \;=\; \frac{1}{\lambda_L} \;=\; \frac{1}{u\, 2\pi T}. \tag{A41}$$

Combining (A38) with the identification $m_S = \sqrt{\kappa_{\rm eff}}\,\tau_{\rm copy}^{-1}$ we obtain

$$m_S \;=\; \sqrt{\kappa_{\rm eff}}\,\tau_{\rm copy}^{-1} \;=\; \underbrace{\Big(\mathcal{C}_{\rm KM}\, u\, 2\pi\, \frac{a}{D_Y}\Big)}_{C_\Lambda\ \text{(dimensionless)}} \sqrt{\kappa_{\rm eff}\,\chi_Y}, \tag{A42}$$

where $\mathcal{C}_{\rm KM}$ is a pure number fixed by the Kubo–Mori normalisation convention used in Section 2 (and therefore not a fit parameter once that convention is fixed). Equation (A42) is the Golden Relation with a *derived* constant:

$$C_\Lambda \;=\; \mathcal{C}_{\rm KM}\, u\, 2\pi\, \frac{a}{D_Y}. \tag{A43}$$

This replaces a geometric postulate by a chaos-controlled derivation: C_Λ is fixed by the microscopic Lyapunov exponent through u, and by transport through a/D_Y, with the remaining factor $\mathcal{C}_{\rm KM}$ determined by the information-metric convention.

 doi:10.20944/preprints202602.1919.v3

Numerical estimate.

For the benchmark values used in the main text, $a = 0.197\ \mathrm{GeV}^{-1}$ and $D_Y = 0.10\ \mathrm{GeV}^{-1}$, so $a/D_Y \simeq 1.97$. Taking $\mathcal{C}_{\mathrm{KM}} \simeq 1$ and a weak-coupling chaos ratio $u \simeq 0.13$ (well below the maximal bound $u \leq 1$), Equation (A43) gives

$$C_\Lambda \;\simeq\; (1) \times (0.13) \times (2\pi) \times (1.97) \;\simeq\; 1.6, \tag{A44}$$

consistent with the benchmark $C_\Lambda = 1.6 \pm 0.2$ adopted in Section 6. The quoted uncertainty is intended to cover moderate variations in u and in the transport ratio a/D_Y.

Dimensional check.

In natural units, $[a] = [D_Y] = \mathrm{GeV}^{-1}$ so a/D_Y is dimensionless; u and $\mathcal{C}_{\mathrm{KM}}$ are dimensionless; hence C_Λ is dimensionless, and (A42) has $[m_S] = \mathrm{GeV}$ because $\sqrt{\chi_Y}$ has units of GeV.

Appendix E.4. Two-Loop Radiative Stability of the Predicted Band

We summarise the two-loop stability requirement in the perturbative portal regime where two-loop running applies in the Z_2 singlet-scalar Higgs-portal model (Section 7). Writing the pole mass as

$$m^2_{S,\mathrm{pole}} \;=\; m^2_S(\mu) \;+\Pi^{(1)}_S(p^2 = m^2_S;\mu) \;+\Pi^{(2)}_S(p^2 = m^2_S;\mu) \;+\; \cdots\,, \tag{A45}$$

radiative stability of the Golden-Relation band requires that higher-order corrections remain subdominant compared to the quoted uncertainty:

$$\left|\Pi^{(2)}_S\right| \;\lesssim\; \delta m^2_S, \qquad \text{and} \qquad \left|\Pi^{(1)}_S\right| \text{ is absorbed in the matching scheme.} \tag{A46}$$

At the parametric level, the dominant portal contribution scales as $\Pi^{(1)}_S \sim (\lambda_{HS}/16\pi^2)\, m^2_h$ and $\Pi^{(2)}_S \sim (\lambda^2_{HS}/(16\pi^2)^2)\, m^2_h$ up to logarithms and thresholds. Therefore, for portal couplings in the phenomenologically viable regime near the Higgs resonance, the two-loop correction is naturally suppressed by an additional $(16\pi^2)^{-1}$ factor. In practice, the stability check consists of running $(\lambda_{HS}, \lambda_S)$ with the two-loop RGEs and verifying that the induced shift in the pole mass remains within the Golden-Relation uncertainty band.

Appendix E.5. Cosmological Closure: Freeze-Out/Freeze-In and Planck Abundance

To close the bridge to cosmology, the predicted parameter region must reproduce the observed relic abundance. For freeze-out, the comoving abundance $Y = n_S/s$ satisfies

$$\frac{dY}{dx} \;=\; -\frac{s\langle\sigma v\rangle}{Hx}\left(Y^2 - Y^2_{\mathrm{eq}}\right), \qquad x \equiv \frac{m_S}{T}, \tag{A47}$$

with $\langle\sigma v\rangle$ determined by the Higgs-portal interaction (Section 7). The relic density follows from

$$\Omega_S h^2 \;=\; \frac{m_S\, s_0\, Y_\infty}{\rho_c/h^2}. \tag{A48}$$

The Golden Relation fixes m_S in terms of $(\kappa_{\mathrm{eff}}, \chi_Y)$; cosmological closure is achieved by showing that the corresponding portal coupling window yields $\Omega_S h^2$ equal to the Planck value within uncertainties.

For freeze-in, the abundance is instead sourced by the production rate Γ_{prod} (portal-mediated scatterings/decays),

$$\frac{dY}{dx} \;=\; \frac{1}{sHx}\,\Gamma_{\mathrm{prod}}(T), \tag{A49}$$

and closure requires that the same m_S band admits a portal coupling range producing the observed $\Omega_{\mathrm{DM}}h^2$ without violating laboratory bounds (direct detection and Higgs invisible), as implemented in Section 7.

 doi:10.20944/preprints202602.1919.v3

References

1. B. Schumacher and R. F. Werner, *Reversible quantum cellular automata*, arXiv:quant-ph/0405174.
2. P. Arrighi, *An overview of quantum cellular automata*, Nat. Comput. **18**, 885 (2019).
3. T. Farrelly, *A review of quantum cellular automata*, Quantum **4**, 368 (2020).
4. S. Chandrasekharan and U.-J. Wiese, *Quantum link models: A discrete approach to gauge theories*, Nucl. Phys. B **492**, 455 (1997).
5. R. C. Brower, S. Chandrasekharan and U.-J. Wiese, *QCD as a quantum link model*, Phys. Rev. D **60**, 094502 (1999).
6. E. A. Martinez *et al.*, *Real-time dynamics of lattice gauge theories with a few-qubit quantum computer*, Nature **534**, 516 (2016).
7. S. Weinberg, *Ultraviolet divergences in quantum theories of gravitation*, in *General Relativity: An Einstein Centenary Survey*, eds. S. W. Hawking and W. Israel (Cambridge University Press, 1979).
8. M. Reuter, *Nonperturbative evolution equation for quantum gravity*, Phys. Rev. D **57**, 971 (1998).
9. A. Eichhorn, *An asymptotically safe guide to quantum gravity and matter*, Front. Astron. Space Sci. **5**, 47 (2019).
10. A. Bonanno, A. Eichhorn, H. Gies *et al.*, *Critical reflections on asymptotically safe gravity*, Front. Phys. **8**, 269 (2020).
11. N. Alkofer, G. D'Odorico, F. Saueressig and F. Versteegen, *Quantum gravitational corrections to the Higgs potential*, Phys. Rev. D **94**, 104055 (2016).
12. A. Held and J. M. Pawlowski, *Higgs sector and vacuum stability in asymptotically safe gravity-matter systems*, Phys. Rev. D **104**, 106023 (2021).
13. R. Kubo, M. Toda and N. Hashitsume, *Statistical Physics II: Nonequilibrium Statistical Mechanics* (Springer, 1991).
14. E. A. Carlen and J. Maas, *An analog of the 2-Wasserstein metric in non-commutative probability under which the fermionic Fokker–Planck equation is gradient flow for the entropy*, Commun. Math. Phys. **331**, 887 (2014).
15. H. Spohn, *Large Scale Dynamics of Interacting Particles* (Springer, 1991).
16. C. Kipnis and C. Landim, *Scaling Limits of Interacting Particle Systems* (Springer, 1999).
17. J. I. Kapusta and C. Gale, *Finite-Temperature Field Theory: Principles and Applications* (Cambridge University Press, 2006).
18. M. Laine and A. Vuorinen, *Basics of Thermal Field Theory* (Springer, 2016).
19. D. Bödeker and M. Laine, K̈ubo relations and radiative corrections for lepton number washout,J̈CAP **05**, 041 (2014)].
20. D. Bödeker and M. Sangel, Örder g^2 susceptibilities in the symmetric phase of the Standard Model,J̈CAP **04**, 040 (2015)].
21. N. Aghanim *et al.* (Planck Collaboration), *Planck 2018 results. VI. Cosmological parameters*, Astron. Astrophys. **641**, A6 (2020)
22. G. Aad *et al.* (ATLAS Collaboration), *Combination of searches for invisible decays of the Higgs boson using 139 fb^{-1} of proton–proton collision data at $\sqrt{s} = 13$ TeV collected with the ATLAS experiment*, Phys. Lett. B **842**, 137963 (2023)].
23. J. Aalbers *et al.* (LZ Collaboration), *Dark Matter Search Results from 4.2 Tonne-Years of Exposure of the LUX-ZEPLIN (LZ) Experiment*, Phys. Rev. Lett. **135**, 011802 (2025)].
24. E. Aprile *et al.* (XENON Collaboration), *First Search for Light Dark Matter in the Neutrino Fog with XENONnT*, Phys. Rev. Lett. **134**, 111802 (2025)].
25. Z. Bo *et al.* (PandaX Collaboration), *Dark Matter Search Results from 1.54 Tonne-Year Exposure of PandaX-4T*, Phys. Rev. Lett. **134**, 011805 (2025)
26. V. Silveira and A. Zee, *Scalar phantoms*, Phys. Lett. B **161**, 136 (1985).
27. J. McDonald, *Gauge singlet scalars as cold dark matter*, Phys. Rev. D **50**, 3637 (1994).
28. C. P. Burgess, M. Pospelov and T. ter Veldhuis, *The minimal model of nonbaryonic dark matter: A singlet scalar*, Nucl. Phys. B **619**, 709 (2001).
29. A. Goudelis, Y. Mambrini and C. Yaguna, *Antimatter signals of singlet scalar dark matter*, J. Cosmol. Astropart. Phys. **12**, 008 (2009).
30. S. Profumo, L. Ubaldi and C. Wainwright, *Singlet scalar dark matter: Correlations between direct, indirect and collider searches*, Phys. Rev. D **82**, 123514 (2010).
31. J. Maldacena, S. H. Shenker and D. Stanford, *A bound on chaos*, JHEP **08**, 106 (2016)
32. J. F. Donoghue, "General relativity as an effective field theory: The leading quantum corrections," Phys. Rev. D **50**, 3874 (1994)

 doi:10.20944/preprints202602.1919.v3

33. T. Jacobson, "Thermodynamics of spacetime: The Einstein equation of state," Phys. Rev. Lett. **75**, 1260 (1995)
34. M. Van Raamsdonk, "Building up spacetime with quantum entanglement," Gen. Rel. Grav. **42**, 2323 (2010)].
35. E. P. Verlinde, "On the Origin of Gravity and the Laws of Newton," JHEP **04**, 029 (2011)].
36. DESI Collaboration, *DESI DR2 Results II: Measurements of Baryon Acoustic Oscillations and Cosmological Constraints*, Phys. Rev. D **112**, 083515 (2025); arXiv:2503.14738 [astro-ph.CO].
37. Y. Yu, T.-P. Tang and L. Feng, *New constraints on singlet scalar dark matter model with LZ, invisible Higgs decay and gamma-ray line observations*, Nucl. Phys. B **1015**, 116910 (2025).
38. E. Aprile *et al.* (XENON Collaboration), *Light Dark Matter Search with 7.8 Tonne-Year of Ionization-Only Data in XENONnT*, arXiv:2601.11296 [hep-ex] (2026).
39. ATLAS Collaboration, *Measurement of the Higgs boson total decay width using the $H \to WW$ off-shell production mode*, arXiv:2601.05168 [hep-ex] (2026).
40. T. Zhou, É. Brunet and X. Qi, *Operator Spreading, Duality, and the Noisy Long-Range FKPP Equation*, arXiv:2505.06353 [cond-mat.stat-mech] (2025).
41. B. Brown *et al.*, *Quantum Lego and XP Stabilizer Codes*, Quantum **9**, 1876 (2025).